

Copyright

by

Tejas Shyam Karande

2007

The Dissertation Committee for Tejas Shyam Karande Certifies that this is the approved version of the following dissertation:

Effect of Scaffold Architecture on Diffusion of Oxygen in Tissue Engineering Constructs

Committee:

C. Mauli Agrawal, Supervisor

Nicholas A. Peppas

David D. Dean

Laura Suggs

Krishnendu Roy

**Effect of Scaffold Architecture on Diffusion of Oxygen in Tissue
Engineering Constructs**

by

Tejas Shyam Karande, B.E.; M.S.E.

Dissertation

Presented to the Faculty of the Graduate School of

The University of Texas at Austin

in Partial Fulfillment

of the Requirements

for the Degree of

Doctor of Philosophy

The University of Texas at Austin

August 2007

Dedication

To my family, without whose love and support I would not be here.

Acknowledgements

There are many people whose advice and guidance have helped me reach this milestone and I would like to thank each and every one of them. I would like to begin by acknowledging Dr. Jagannathan Mahadevan for his patient, sustained help with the diffusion modeling aspect of the project. In spite of his own dissertation, he found the time to help me and I will be ever grateful for his assistance. I would also like to thank Dat Dinh and Robert Hardin who taught me the basics of cell culture; Dr. Vic Sylvia and Dr. David Dean who not only gave me access to their laboratory, but would always sit down with me and try to help me overcome the obstacles that one encounters when dealing with all aspects of cell behavior; Dr. David Carnes who helped me decide what assays were appropriate for studying different cell functions and Dr. Victoria Frohlich, who helped me numerous times with advice regarding the best way to image my constructs. I would also like to acknowledge Paul Flores for helping with the design and construction of the permeability tester as well as Dr. Wei Sun, Lauren Shor and Binil Starly for fabricating the scaffolds. Dr. Stephanie Cano's invaluable assistance with statistical analysis of my data is greatly appreciated. Finally, I would like to sincerely thank my mentor Dr. C. Mauli Agrawal for his wise guidance, timely advice and sustained support in all aspects towards the completion of this project.

Effect of Scaffold Architecture on Diffusion of Oxygen in Tissue Engineering Constructs

Publication No. _____

Tejas Shyam Karande, PhD

The University of Texas at Austin, 2007

Supervisor: C. Mauli Agrawal

Viable tissue formation is often observed in peripheral regions of tissue engineering scaffolds whereas the interior fails to support viable tissue. This could be attributed to the fact that as cells within the pores of the scaffold begin to proliferate and secrete extracellular matrix, they simultaneously begin to occlude the pores and decrease supply of nutrients to the interior. Since transport within the scaffold is mainly a function of diffusion, careful design of the diffusion characteristics of the scaffold is critical. These transport issues relate to oxygen and nutrient delivery, waste removal, protein transport and cell migration, which in turn are governed by scaffold porosity and permeability. The current study addresses these issues by evaluating the effect of these architectural parameters on oxygen concentration and cell behavior in the interior of scaffolds with different architectures. Cylindrical polycaprolactone (PCL) scaffolds fabricated using precision extrusion deposition and having the same pore size but different porosities and tortuosities, and hence different permeabilities, were statically

seeded with MG63 cells. The bases of the scaffolds were sealed with an impermeable layer of PCL and the scaffolds were surrounded with a tubing of low air permeability to allow diffusion of air into the constructs mainly from the top. These constructs were evaluated at days 1 and 7 for cell viability and proliferation as well as oxygen concentration as a function of depth within the construct. A simple mathematical model was used to describe the process of diffusion of oxygen in these cell-seeded scaffolds of varying permeability. It was hypothesized that there would be better diffusion and cell function with increasing permeability. This was found to be true in case of cell viability. However, cell proliferation data revealed no significant differences as a function of depth, day or architecture. Oxygen concentration data revealed trends showing decreasing concentrations of oxygen as a function of depth across all architectures. Tortuosity had a greater influence on oxygen concentration profiles on day 1 compared to porosity, whose effect seemed to dominate on day 7. Overall, porosity seemed to play a greater role than tortuosity in supporting viability, proliferation and oxygen diffusion.

Table of Contents

List of Tables	x
List of Figures	xi
INTRODUCTION	1
BACKGROUND	4
Chapter 1: Scaffold Architecture	4
Pore size and shape	4
Porosity	7
Pore interconnectivity	10
Permeability	12
Chapter 2: Modeling of Diffusion in Tissue Engineering Scaffolds	16
Chapter 3: Scaffold Fabrication Techniques.....	26
Solvent casting and particulate leaching (SCPL).....	26
Rapid prototyping (RP)/Solid freeform fabrication (SFF).....	27
Chapter 4: Measurement of Oxygen Concentration	30
Oxygen microelectrode	30
Phosphorescence quenching	32
MATERIALS AND METHODS	34
Chapter 5: Construct Specifications.....	34
Scaffold material and method of fabrication	34
Cell type selection.....	35
Scaffold architectural parameter selection.....	35
Chapter 6: Measurement of Scaffold Porosity.....	41
Chapter 7: Measurement of Scaffold Permeability.....	42
Chapter 8: Measurement of Oxygen Concentration	46
Theory of polarographic oxygen measurement	46

Apparatus for oxygen concentration measurement.....	47
Calibration of sensor	49
Protocol for measurement of oxygen concentration	51
Chapter 9: Measurement of Cell Viability.....	57
Chapter 10: Measurement of Cell Proliferation.....	65
Chapter 11: Mathematical Model for Diffusion of Oxygen	69
RESULTS	84
Chapter 12: Oxygen Concentration Measurement Results.....	84
Chapter 13: Cell Viability Measurement Results	96
Depth comparison	97
Day comparison	97
Type comparison.....	97
Chapter 14: Cell Proliferation Measurement Results	99
Depth comparison	100
Day comparison	100
Type comparison.....	100
Chapter 15: Validation of Diffusion Model.....	101
DISCUSSION	105
Porosity, permeability and water retention time	105
Oxygen concentration	106
Cell viability.....	108
Cell proliferation.....	109
Correlation between oxygen concentration, cell viability and cell proliferation	111
Diffusion model	117
CONCLUSIONS	118
References.....	119

List of Tables

Table 1. Porosity of scaffolds	41
Table 2. Selection of control(c) and sample(s) scaffolds for oxygen concentration measurement	56
Table 3. Selection of constructs for cell viability measurement (n = 3).	60
Table 4. Selection of constructs for cell proliferation measurement (n = 3).	66

List of Figures

Figure 1. Scaffold architectural parameters selected.	37
Figure 2. Type 1 (a) side view, (b) isotropic view. Type 2 (c) side view, (d) isotropic view. Images were generated using Rhinoceros® (McNeel North America, Seattle, WA). The blue arrows indicate the probable path that fluid would take to go from top to bottom if it follows the path of least resistance and is used to estimate tortuosity.	38
Figure 3. Type 3 (a) side view, (b) isotropic view. Type 4 (c) side view, (d) isotropic view. Images were generated using Rhinoceros® (McNeel North America, Seattle, WA). The blue arrows indicate the probable path that fluid would take to go from top to bottom if it follows the path of least resistance and is used to estimate tortuosity.	39
Figure 4. Estimating porosity from side view of scaffold schematics for architectures of (a) Type 1 and 2, (b) Type 3 and 4.	40
Figure 5. Permeability tester.	44
Figure 6. Permeabilities of different scaffold architectures.	44
Figure 7. Water retention times for different scaffold architectures.	45
Figure 8. Measurement of oxygen concentration.	48
Figure 9. Chemical microsensor.	48
Figure 10. Calibration cell.	50
Figure 11. Apparatus for oxygen concentration measurement.	50
Figure 12. Constructs just removed from the incubator (a) placed in the water bath; (b) being equilibrated.	55
Figure 13. Hypodermic needle surrounding the sensor being descended into the construct.	55
Figure 14. Schematic depicting sectioning of scaffold resulting in the generation of six surfaces for viewing under the fluorescence microscope.	59
Figure 15. Schematic depicting fluorescence imaging of a scaffold surface after sectioning.	60
Figure 16. Images on day 1 of (a) MG63 cells seeded in a well, not treated with calcein AM (brightfield image), (b) MG63 cells treated with calcein AM (fluorescent image), (c) scaffold without cells treated with calcein AM (control) (fluorescent image), (d) scaffold with cells treated with calcein AM (sample) (fluorescent image). The red scale bar is 0.1 cm in length.	62
Figure 17. Images on day 7 of (a) MG63 cells not treated with calcein AM (brightfield image), (b) MG63 cells treated with calcein AM (fluorescent image), (c) scaffold without cells treated with calcein AM (control) (fluorescent image), (d) scaffold with cells treated with calcein AM (sample) (fluorescent image). The red scale bar is 0.1 cm in length.	63
Figure 18. Images on day 1 of (a) MG63 cells not treated with BrdU kit (brightfield image), (b) MG63 cells treated with BrdU kit (fluorescent image), (c) scaffold without cells treated with BrdU kit (control) (fluorescent image), (d) scaffold with	

cells treated with BrdU kit (sample) (fluorescent image). The red scale bar is 0.1 cm in length.	67
Figure 19. Images on day 7 of (a) MG63 cells not treated with BrdU kit (brightfield image), (b) MG63 cells treated with BrdU kit (fluorescent image), (c) scaffold without cells treated with BrdU kit (control) (fluorescent image), (d) scaffold with cells treated with BrdU kit (sample) (fluorescent image). The red scale bar is 0.1 cm in length.	68
Figure 20. Schematic of air diffusing into cell-seeded scaffold	69
Figure 21. Matlab-generated oxygen concentration profiles for different magnitudes of the rate constant for (a) Type 1 on day 1, (b) Type 1 on Day 7, (c) Type 2 on day 7, (d) Type 3 on day 7 and (e) Type 4 on day 7.....	81
Figure 22. Mean (\pm SD) oxygen concentration profiles for controls and samples of architecture Type 1 and 2 on day 1 for (a) $n = 3$, (b) ignoring T1 sample from Set 2.	84
Figure 23. Mean (\pm SD) oxygen concentration profiles for controls and samples of architecture Type 3 and 4 on day 1 for (a) $n = 3$, (b) ignoring T4 sample from Set 2.	85
Figure 24. Mean (\pm SD) oxygen concentration profiles for controls and samples of architecture Type 1 and 2 on day 7 for (a) $n = 3$, (b) ignoring T1 control and T2 control from Set 1.	86
Figure 25. Mean (\pm SD) oxygen concentration profiles for controls and samples of architecture Type 3 and 4 on day 7 for (a) $n = 3$, (b) ignoring T3 control from Set 1.	87
Figure 26. Oxygen concentration profiles for (a) Type 1 on day1 from set 2, (b) Type 4 on day 1 from set 2.....	88
Figure 27. Type 1, day 1, set 2 (a) mean (\pm SD) % area of sample covered by live cells, (b) mean (\pm SD) % area fraction values for control i.e. background, (c) differences between corresponding mean levels of sample and control.....	89
Figure 28. Type 4, day 1, set 2 (a) mean (\pm SD) % area of sample covered by live cells, (b) mean (\pm SD) % area fraction values for control i.e. background, (c) differences between corresponding mean levels of sample and control.....	90
Figure 29. Oxygen concentration profile for Type 3, day 1, set 2.....	91
Figure 30. Type 3, day 1, set 2 (a) mean (\pm SD) % area of sample covered by live cells, (b) mean (\pm SD) % area fraction values for control i.e. background, (c) differences between corresponding mean levels of sample and control.....	92
Figure 31. Oxygen concentration profile for control and sample of Type 2 while (a) descending (D) and ascending (A) for Day 1, Set 1, (b) descending (D) only for Day 7, Set 3.	94
Figure 32. Oxygen concentration values in the top 0.4 cm for different scaffold types...	95
Figure 33. Cell viability as reflected by the mean % area of scaffold covered by viable cells for the different scaffold architectures for both days for the (a) top, (b) middle and (c) bottom regions. Graphs represent means ($n = 3$) \pm SD.....	96
Figure 34. Cell proliferation as reflected by the mean % area fraction for the different scaffold architectures for both days for the (a) top, (b) middle and (c) bottom regions. Graphs represent means ($n = 3$) \pm SD.	99

Figure 35. Profiles for the sample mean and the model for Type 1 ($P = 0.42$, $T = 1$) on (a) day 1 ($t = 86,400$ s) ($K = 0.00019$), (b) day 7 ($t = 604,800$ s) ($K = 0.00005$).	101
Figure 36. Profiles for the sample mean and the model for Type 2 ($P = 0.47$, $T = 1.25$) on (a) day 1 ($t = 86,400$ s) ($K = 0.00008$), (b) day 7 ($t = 604,800$ s) ($K = 0.00015$). ...	102
Figure 37. Profiles for the sample mean and the model for Type 3 ($P = 0.25$, $T = 1$) on (a) day 1 ($t = 86,400$ s) ($K = 0.00011$), (b) day 7 ($t = 604,800$ s) ($K = 0.00006$).	103
Figure 38. Profiles for the sample mean and the model for Type 4 ($P = 0.27$, $T = 1.88$) on (a) day 1 ($t = 86,400$ s) ($K = 0.00002$), (b) day 7 ($t = 604,800$ s) ($K = 0.00003$). ...	104
Figure 39. (a) Mean oxygen concentration, (b) mean cell viability, (c) mean cell proliferation for Types 1 and 2 on day 1.....	112
Figure 40. (a) Mean oxygen concentration, (b) mean cell viability, (c) mean cell proliferation for Types 3 and 4 on day 1.....	113
Figure 41 (a) Mean oxygen concentration, (b) mean cell viability, (c) mean cell proliferation for Types 1 and 2 on day 7.....	115
Figure 42. (a) Mean oxygen concentration, (b) mean cell viability, (c) mean cell proliferation for Types 3 and 4 on day 7.....	116

INTRODUCTION

The majority of tissue engineering techniques currently under investigation utilize a scaffold seeded with cells. These scaffolds are often designed for specific applications and fabricated from a variety of biomaterials such as biopolymers, synthetic polymers, ceramics or metals. Scaffolds must possess a number of basic characteristics, including certain physical, mechanical, chemical and structural/architectural properties that are dictated by the tissue to be regenerated.⁴ For the vast majority of tissues, nutrient transport through the scaffold is a critical factor in achieving success. In the normal *in vivo* scenario vasculature provides most of the nutrients essential for cells to function. However, such blood supply is not available for tissue engineered constructs either *in vitro* or during the immediate post-implantation phases *in vivo*. Thus, the ability of a scaffold to enable the adequate delivery of nutrients to resident cells is crucial for the success of any scaffold-based tissue engineering endeavor.

Since transport within the scaffold is mainly a function of diffusion, careful design of the diffusion characteristics of the scaffold is critical. These transport issues relate to oxygen and nutrient delivery, waste removal, protein transport and cell migration, which in turn are governed by scaffold porosity¹¹⁶ and permeability. The size, geometry, orientation, interconnectivity, branching and surface chemistry of pores and channels directly influence the extent and nature of nutrient diffusion and tissue in-growth.^{101,117} Quite often viable tissue formation is observed in the peripheral regions of scaffolds whereas the interior fails to support viable tissue due to lack of adequate diffusion.⁴² This may be a manifestation of the fact that as cells within the pores of the scaffold begin to proliferate and secrete extracellular matrix, they simultaneously begin to

occlude the pores and decrease the supply of nutrients to the interior.⁴⁵ Although scaffolds of small dimensions, of the order of a few millimeters, have usually been found to be well-infiltrated and occupied by viable cells, there is a real need for designing and evaluating bigger scaffolds along the length scales for practical *in vivo* applications, with suitable internal architectures. The appropriate scaling up of the scaffold dimensions proves to be very challenging given the mass transport and diffusion limitations experienced by cells in the interior of big scaffolds.

From an architectural point of view, transport issues within a scaffold are governed primarily by pore size, porosity, tortuosity and permeability. Thus, the overall goal of the present study was to examine the effect of these parameters on the availability of nutrients and degree of cellular activity within a model tissue engineering scaffold for bone. Moreover, a simple mathematical model was also used to describe these effects. Thus, the following specific aims were addressed:

Specific Aim 1: To investigate the availability of oxygen within the interior of scaffolds as a function of architectural parameters.

Hypothesis: The availability of oxygen in the interior of the scaffold is a function of architecture. Poly(ϵ -caprolactone) (PCL) scaffolds of a fixed pore size and porosity fabricated using a precision extrusion deposition (PED) system and possessing controlled ranges of tortuosity and permeability values were tested under static conditions. For each architecture, the oxygen concentration within the cell-seeded scaffold was measured as a function of distance from the surface using microelectrodes at days 1 and 7, to determine how architectural parameters affect diffusion of oxygen in the scaffold interior.

Specific Aim 2: To examine cell behavior in the interior of scaffolds as a function of architectural parameters and correlate to availability of oxygen.

Hypothesis: Cell behavior will be enhanced with increasing availability of oxygen.

MG63 osteoblast-like cells were statically seeded on scaffolds with different architectures. Cell viability and proliferation were examined as a function of depth at days 1 and 7. The findings were correlated with oxygen concentration values obtained from Aim 1.

Specific Aim 3: To develop a simple diffusion-based mathematical model to predict the availability of oxygen within a scaffold as a function of architectural parameters and depth.

Hypothesis: The mathematical model will reasonably depict the concentration-depth profile of oxygen in statically cell-seeded scaffolds. The process of oxygen diffusion in statically cell-seeded scaffolds will be modeled by analytically solving the mass transfer equation depicting the diffusion. The concentration-depth profiles of oxygen obtained from Aim 1 will be used to validate the model.

BACKGROUND

Chapter 1: Scaffold Architecture

The architectural properties of a scaffold mainly dictate the transport that occurs within it, which is primarily a function of diffusion. The transport issues comprise delivery of oxygen and other nutrients, removal of waste, transport of proteins and cell migration, which in turn are governed by scaffold porosity and permeability.⁴⁵ The size, geometry, orientation, interconnectivity, branching and surface chemistry of pores and channels directly affect the extent and nature of nutrient diffusion and tissue in-growth.^{101,117} Generally, living tissue is observed in the outer regions of scaffolds whereas the interior fails to support viable tissue due to lack of adequate diffusion.⁴² This may arise due to the fact that as cells within the pores of the scaffold begin to proliferate and secrete extracellular matrix (ECM), they simultaneously begin to block off the pores, thereby reducing the supply of nutrients to the interior. The formation of this surface layer of tissue with sparse matrix in the interior has been referred to as the “M&M effect”, referring to the popular brand of candy having a hard crust and soft core.⁴⁵

PORE SIZE AND SHAPE

A scaffold cannot be completely solid as cells need to grow within it and these need to be supplied with nutrients. Thus, the need for a scaffold to have holes or pores or channels seems obvious but not so obvious is what their shape and dimensions should be. The pore size should at least be a few times the size of the cells that will be seeded on it to provide enough space for the entry and exit of nutrients and waste, respectively. Also, blood vessels and growth factors may need to enter the construct as well. There is no common pore or channel size range that is suitable for all types of tissue growth as cells

making up different tissues have different dimensions. Sosnowski et al.⁹⁸ prepared poly(L-lactic acid)/poly(lactic-co-glycolic) acid (PLL/PLGA) scaffolds from microparticles with a bimodal pore size distribution. Macropores in the 50-400 microns range promoted osteoblast growth and proliferation within the scaffold where as micropores in the range of 2 nm-5 microns in the scaffold walls allowed for diffusion of nutrients and metabolites as well as products of polyester hydrolysis. Draghi et al.²² used three different porogens (gelatin microspheres, paraffin microspheres and salt crystals) to fabricate scaffolds from commonly used biodegradable materials via the solvent casting particulate leaching (SCPL) technique to see which allowed maximum control over scaffold morphology. Although all the porogens contributed to producing highly porous scaffolds, microsphere leaching produced well-defined spherical pores that resulted in better mechanical properties and lesser flow resistance.

Researchers have fabricated scaffolds with different pore sizes or even a range of pore sizes within the same scaffold to see their effect on cell growth and to mimic certain types of tissues. Oh et al.⁷⁷ fabricated cylindrical PCL scaffolds with gradually increasing pore sizes along the longitudinal axis using a novel centrifugation method to evaluate the effect of pore size on cell-scaffold interaction. The pore sizes within the scaffold gradually increased from 88 to 405 microns and the porosity from 80% to 94% due to the gradual increment of centrifugal force along the cylindrical axis. Chondrocytes, osteoblasts and fibroblasts were evaluated for their interaction *in vitro* with this PCL scaffold and *in vivo* using calvarial defects in a rabbit model. The scaffold section having pore sizes in the 380-405 micron range showed better chondrocyte and osteoblast growth while the 186-200 micron range was better suited for fibroblast growth. Moreover, the scaffold section with a 290-310 micron range pore size seemed to be best suited for new bone formation. This shows the existence of pore ranges that are ideal for the growth of

some cell types and that this range can change while the cells differentiate to form tissue.

Woodfield et al.¹¹³ investigated the ability of anisotropic pore architectures to control the zonal organization of chondrocytes and ECM components in scaffolds made of poly(ethylene glycol)-terephthalate-poly(butylene terephthalate) (PEGT/PBT). They used a 3D fiber deposition technique to produce scaffolds with either uniformly spaced pores (fiber spacing of 0.1 cm and pore size of 680 microns diameter) or pore size gradients (fiber spacing of 0.05-0.2 cm and pore size range of 200-1650 microns diameter), but having a similar overall porosity of about 80%. They found the gradient to promote anisotropic cell distribution similar to that found in the upper, middle and lower zones of immature bovine articular cartilage, irrespective of whether the method of cell seeding was static or dynamic. Additionally, they discovered a direct correlation between the zonal porosity and both DNA and glycosaminoglycan (GAG) content. Also, Harley et al.³⁰ produced cylindrical scaffolds with a radially aligned pore structure having a smaller mean pore size and lesser porosity towards the outside. Increasing the spinning time and/or velocity caused the formation of a large inner diameter hollow tube and a gradient of porosity along the radius due to increased sedimentation.

There is no consensus regarding the optimal scaffold pore size for bone regeneration in scaffolds, although a range of 50-400 μm was found to be optimum for the development of highest fixation strength in metallic implants possessing porous surfaces.^{7,8} Kuboki et al.⁴⁹ found that a pore size of 300-400 μm was optimal to efficiently promote bone formation in porous, honeycomb-shaped hydroxyapatite (HCHAP). They absorbed a solution of rh-BMP-2 on HCHAP scaffolds containing longitudinal tunnels of different diameters and implanted these subcutaneously into the backs of rats. The scaffolds with smaller diameter (90-120 μm) tunnels were found to promote chondrogenesis first, followed by vascular invasion leading to subsequent

osteogenesis, whereas with larger diameter (350 μm) tunnels there was direct osteogenesis without any cartilage formation, probably owing to vascularization from the onset. Thus, the authors concluded that the geometry of the BMP carrier controlled differentiation of cells to form bone or cartilage. However, there are studies that argue that smaller pore sizes may be adequate for bone growth⁴⁴ and that pore sizes in the 150 to 710 μm range do not have any significant effect on osteoblast behavior.^{42,43,80} Although results vary, an important underlying trend is the need for scaffolds to have a high porosity.

POROSITY

Porosity is the amount of void space within the scaffold structure. Several studies have emphasized the need for high porosity and high surface area-to-mass ratio for ensuring uniform cell delivery and tissue ingrowth.⁶⁹ Need has also been expressed for polymeric scaffolds to possess an open pore network for optimal diffusion of nutrients and waste.¹⁰⁵ Another study stated that a scaffold should ideally possess a porosity of 90% to allow for adequate diffusion during tissue culture and to provide sufficient area for cell-polymer interactions.²³ However, Goldstein et al.²⁶ have cautioned that polylactic-polyglycolic acid (PLG) scaffolds be prepared with a porosity not exceeding 80% for implantation into orthopaedic defects as it would otherwise compromise the integrity of the scaffold. Thus, in the case of polymeric scaffolds there may be a conflict between optimizing the porosity and maximizing mechanical properties. Further complicating matters is the finding by Agrawal et al.² that lower initial porosity and permeability results in a faster rate of degradation for PLG scaffolds and lower mechanical properties during the initial weeks. Wu et al.¹¹⁴ investigated the effects of porosity (80-95%) and pore size (50-450 microns) on the degradation of 85/15 PLGA

scaffolds, performed in phosphate-buffered saline (PBS) at 37 degrees C up to 26 weeks. Scaffolds possessing a higher porosity or smaller pore size degraded more slowly than those with a lower porosity or larger pore size as the latter had thicker pore walls and smaller surface areas that prevented the diffusion of acidic degradation products resulting in greater acid-catalyzed hydrolysis.

Thus, in view of these contradictory factors, there is a need to optimize scaffolds for bone regeneration based on their specific mechanical requirements balanced with their desired useful life and diffusion characteristics. One possible way of achieving this would be to optimize porosity with respect to nutrient availability and match it with biomaterials that can provide adequate mechanical properties. Lin et al.⁶¹ developed a general design optimization strategy for 3D internal scaffold architecture to have the required mechanical properties and porosity simultaneously, using the homogenization-based topology optimization algorithm for bone tissue engineering. Howk et al.³⁶ showed that it was possible to increase the porosity and strength of a bone tissue engineering scaffold through simple iterations in architectural design using CAD software and finite element analysis. The goal of their optimization was to maintain the strength of a design constant while increasing its porosity. Xie et al.¹¹⁵ selected mechano-active scaffolds that respond to applied compression stress without undergoing permanent deformation for engineering functional articular cartilage from a biomechanical point of view and then determined the best porosity. They used poly(lactide-co-caprolactone) (PLCL) sponges (pore size: 300-500 microns, porosity: 71-86%) as mechano-active scaffolds and determined that the lower their porosity, the nearer their mechanical properties came to those of native cartilage. Hence, the scaffold with a porosity of 71% was found to be the best suited for cartilage regeneration. Moroni et al.⁷² varied pores in size and shape by altering fiber diameter, spacing as well as orientation and layer thickness using the 3D

fiber deposition method in order to study their influence on dynamic mechanical properties. They observed a reduction in elastic properties like dynamic stiffness and equilibrium modulus as well as an increase of viscous parameters like damping factor and creep unrecovered strain as porosity increased.

Characterization of porosity is an important aspect of any scaffold fabrication protocol. There are several methods to determine the porosity of a scaffold and quite often more than one method is used to verify results obtained by the other method.^{37,67,109} A popular technique is the use of mercury intrusion porosimetry (MIP)^{9,26,37,58,68,74,76,83,103,109,110} in which void volume is determined by forcing mercury into the pores under pressure. This technique is based on the principle that the pressure required to force a non-wetting liquid such as mercury into pores, against the resistance imparted by liquid surface tension, is indicative of pore size and void volume.³

Porosity values may also be derived from scanning electron microscopy of cross-sections of scaffolds.^{7,8,37,40,58,78,95,100,109,122} Two-dimensional images and image analysis can yield the pore to polymer area, which is then extrapolated to three-dimensions to obtain estimates of porosity. Another rather simple technique involves the use of the Archimedes' Principle that requires the scaffold to be weighed when dry, wet and submerged in water.^{1,13} Yet another method used to obtain the porosity of a scaffold requires the use of its density,^{34,39,78,93} and is referred to by some as gravimetry.⁶⁸ Recently, helium pycnometry has also been employed for porosity measurement. This requires the sample to be sealed in a chamber that is purged, evacuated and pressurized with helium, which is then allowed to vent into an evacuated chamber. When the volumes of both chambers are known, the pressure decrease following venting is used to calculate the sample volume.⁶⁰

PORE INTERCONNECTIVITY

It is not sufficient for a scaffold to be porous but the pores in the scaffold need to be interconnected for efficient delivery of nutrients to the interior and removal of waste to the exterior of the scaffold. Pore interconnectivity also has implications as far as transport of proteins, cell migration and tissue ingrowth are concerned.

Griffon et al.²⁷ found chondrocyte proliferation and metabolic activity to improve with increasing interconnected pore size of chitosan sponges. Lee et al.⁵² produced poly(propylene fumarate) (PPF) scaffolds with controlled pore architecture to study the effects of pore size and interconnectivity on bone growth. They fabricated scaffolds with three pore sizes (300, 600 and 900 microns) and randomly closed 0%, 10%, 20% or 30% of the pores. Porosity and permeability decreased as the number of closed pores increased, especially when the pore size was 300 micron, as a result of low porosity and pore occlusion. Suh et al.¹⁰⁰ compared the proliferation of chondrocytes on equally porous (95%) PLG scaffolds prepared by the solvent casting and particulate leaching technique using two different porogens: salt and gelatin. The scaffolds produced using gelatin exhibited better cell attachment and proliferation, and this was attributed to better pore interconnectivity at the same porosity. Hou et al.³⁴ suggested that extraction of salt particles in a salt leaching process implied that the resulting pores were interconnected. However, complete removal of the salt does not necessarily ensure a permeable structure as there might be dead-end spaces with only a single opening thereby not permitting end-to-end interconnectivity of the whole structure.⁴⁵

Traditional scaffold manufacturing techniques have been modified to increase pore interconnectivity. Murphy et al.⁷³ imparted improved pore interconnectivity to PLGA scaffolds by partially fusing the salt before creating the polymer matrix via either the solvent casting/salt leaching process or the gas foaming/salt leaching process. Gross

et al.²⁸ made spheroid salt particles in a flame and sintered them to produce an interconnected salt template, which was filled with a carbonated fluorapatite powder and polylactic polymer to form a composite scaffold. A larger pore size was possible with the use of large spherical salt particles and this technique could be used to successfully produce scaffolds with good interconnectivity and graded pore sizes. Hou et al.³⁵ fabricated highly porous (93-98%) and interconnected scaffolds by freeze-drying polymer solutions in the presence of a leachable template followed by leaching of the template itself. Sugar or salt particles were fused to form the well-connected template, the interstices of which were filled with a polymer solution in solvent, followed by freeze-drying of the solvent and subsequent leaching of the template. This resulted in relatively large interconnected pores based on the template and smaller pores resulting from the freeze-drying process.

Darling et al.²⁰ and Wang et al.¹⁰⁷ used computed micro tomography (microCT) to quantify pore interconnectivity within their PCL scaffolds for bone tissue engineering that were manufactured by PED. They achieved pore interconnectivity greater than 98% in their scaffolds. Moore et al.⁷⁰ also used microCT followed by a custom algorithm to nondestructively quantify pore interconnectivity. The program calculated accessible porosities over a range of minimum connection sizes. The accessible porosity varied with connection size as a function of porogen content. However, microCT is still not widely available and researchers have improvised, like Li et al.⁵⁹ who appreciated the difficulty in obtaining 3D information about pore interconnectivity through 2D images and devised a rather simple, but novel experiment to verify the same. They soaked porous HA in black pigment dispersion and centrifuged it. After removal of pigments, they sectioned, dried and pictured the sample. Black colored pores were found to have been accessible either directly or via adjacent pores.

PERMEABILITY

The terms permeability and porosity are sometimes used interchangeably in tissue engineering. These terms have inherently different meanings where porosity indicates the amount of void space within a structure while permeability is a measure of the ease with which a fluid can flow through the structure.² Empirical relations for permeability and porosity have been described by Scheidegger⁸⁹ using various simplistic capillare models to represent the porous structure, for example the straight capillare model comprising a bundle of straight parallel capillaries, where the permeability $k = P^3/T^2 \cdot S^2$, where P is the porosity, T is the tortuosity i.e. the ratio of the flow path length to the model length and S is the average specific surface area i.e. the ratio of the area of the capillaries to the volume of the model. The tortuosity term is a reflection of the internal architecture of the scaffold and refers to the twisted path that a fluid would take through the interconnected pores in order to get from one end of the scaffold to the opposite end, divided by the straight line distance between the opposite faces.⁴⁵ The fluid will take the path of least resistance though the scaffold, thus changing its direction whenever its path is obstructed by the polymer. Tortuosity is, thus, the result of the hindrance offered to fluid flow by the polymer. Greater the hindrance, greater the tortuosity and lesser the permeability. The Kozeny equation describing permeability in a system by the equation $k = c \cdot P^3/S^2$ has also been modified to $c \cdot P^3/T \cdot S^2$ in order to incorporate the tortuosity term.^{17,89} Here c is a dimensionless constant, called the Kozeny constant, whose value depends on the geometry of the cross section of the capillary tube. However, T and S are difficult to determine independently and c varies considerably from one sample to the next as it is an empirical factor.¹⁷

Generally, an increase in porosity leads to an increase in permeability, but for this to happen the pores need to be highly interconnected.⁴⁵ Agrawal et al. have previously

shown that scaffolds can possess different permeabilities while maintaining similar porosity.^{1,2} Thus, permeability should be treated as an independent scaffold design parameter. A high permeability can translate into superior diffusion within the scaffold, which would facilitate the inflow of nutrients and the disposal of degradation products and metabolic waste.⁴⁵ Permeability is also affected by fluid-material interactions and thus influences the viscoelastic response of a scaffold. This in turn affects the fluid pumping movement of the scaffold.⁵¹ This is of importance in the design of scaffolds for articular cartilage repair, where mechanotransduction and cell apoptosis may be affected by hydrostatic pressure and flow-induced shear.

The porosity and permeability of a scaffold are obviously related to the physical and mechanical properties of a scaffold. For example, better mechanical properties may be obtained for a scaffold if it is made more solid and less porous. Less obvious is the fact that porosity and permeability can also have a significant impact on the chemical behavior of the scaffold, especially its degradation characteristics.⁴⁵ For example, as stated earlier it has been shown that low porosity and permeability PLG scaffolds degrade faster.^{2,6} Also, such scaffolds exhibit a lower decrease in their mass, molecular weight, and mechanical properties under dynamic fluid flow conditions compared to static conditions. ²This phenomenon has been attributed to the inhibition of autocatalytic degradation due to better diffusion or forced fluid flow.

Li et al.⁵⁸ found that porosity and pore size alone were inappropriate to describe the accessibility of inner voids in macroporous scaffolds. They advocated the use of the permeability/porosity ratio, which is an indicator of the percolative efficiency per unit porous volume of a scaffold, where permeability can be termed as the conductance normalized by size of sample and fluid viscosity. A positive correlation was possible between porosity and permeability provided there was good interconnection between the

pores. They found that permeability could represent a combination of five important scaffold parameters: porosity, pore size and distribution, interconnectivity, fenestration size and distribution and pore orientation.

Wang et al.¹⁰⁸ wanted to optimize scaffold morphology for connective tissue engineering to overcome the problem of disproportionately high tissue formation at surfaces of scaffolds grown in bioreactors relative to their interior. Thus, they determined geometric parameters for PEGT/PBT scaffolds using SEM, microCT and flow permeability measurements and then seeded fibroblasts on these scaffolds under dynamic flow conditions for 2 weeks. Only scaffolds with an intermediate pore interconnectivity supported homogeneous tissue formation throughout the scaffold with complete filling of all pores. Hollister et al.³³ used an integrated image-based design along with SFF to create scaffolds with the desired elasticity and permeability from a variety of biomaterials including degradable polymer, titanium and ceramics to fit any craniofacial defect. The scaffolds supported significant bone growth in minipig mandibles for a range of pore sizes from 300 to 1200 microns. Huang et al.³⁸ used scaffolds made of chitosan and PLGA with longitudinally oriented channels running through them to serve as guides for nerve generation. They found chitosan to be a better scaffold for nerve guidance compared to PLGA owing to its high permeability and characteristic porous structure.

In addition to traditionally used direct permeation experiments, based on Darcy's law, as conducted by Spain et al.⁹⁹ and Li et al.,⁵⁸ researchers have begun to use magnetic resonance imaging (MRI) and microCT for measuring permeability as well. Neves et al.⁷⁵ used MRI to determine construct permeability to a low molecular weight MR contrast agent and correlate the findings with measurements of cell growth and energetics. They used perfusion bioreactors to seed mature sheep meniscal fibrochondrocytes on polyethylene terephthalate (PET) fabric to produce bioartificial meniscal cartilage

constructs. Knackstedt et al.⁴⁸ used microCT with a resolution of 16.8 microns to measure a number of structural characteristics like pore volume-to-surface-area ratio, pore size distribution, permeability, tortuosity, diffusivity and elastic modulus of coral bone graft samples.

Chapter 2: Modeling of Diffusion in Tissue Engineering Scaffolds

With diffusion in tissue engineering scaffolds increasingly receiving importance, some research groups have attempted to model the process. Galban et al.²⁴ developed a mathematical model of chondrocyte generation and nutrient consumption to analyze the behavior of cell growth in biodegradable polymer matrices of different thicknesses. They concluded that restricted nutrient diffusion was not the sole factor limiting cell growth in polymers of varying thicknesses as all kinetic growth functions required variations in the kinetic parameters to fully describe the effects of polymer thickness. They advocated including the effects of biological waste, growth moderating biological species as well as presence of the extracellular matrix (ECM) to increase the sensitivity of their model. Scaffold architecture could also be an important component in the above model to more accurately describe the cell growth kinetics.

Botchwey et al.¹⁰ developed a one-dimensional model to study the efficiency of glucose diffusion to osteoblast-like cells in PLG scaffolds under static and dynamic culture conditions. They assumed that the scaffold possessed cylindrical channels with a fixed cell density consuming the same amount of glucose in the absence of flow. They utilized an equation developed by Petrov et al.⁸¹ to formulate the homeostatic diffusion problem within lacunar-canalicular systems in conjunction with suitable boundary conditions to obtain an analytical solution for concentration of glucose(C) as a function of depth (x) within the scaffold:

$$C(x) = C_o - \frac{Nr}{2Dn\sigma} (Lx - x^2)$$

where,

Co: glucose concentration at the exterior boundary of the scaffold (g m^{-3})

N: total number of cells within the scaffold

r: single osteoblast rate of glucose consumption (g s^{-1})

L: thickness of scaffold (m)

l: length of cylindrical pores within scaffold (m)

D: Diffusivity of glucose ($\text{m}^2 \text{s}^{-1}$)

n: total number of cylindrical pores

σ : average cross-sectional area of pores (m^2)

For the dynamic case they assumed that neither would the geometry of the scaffold change nor would the scaffold degrade over the period they considered for modeling purposes. Also, the scaffold cell density was once again held constant and glucose consumption was assumed to be uniform as a function of depth within the scaffold. They utilized equations¹¹ for calculating permeability in a cylindrical scaffold having cylindrical channels in conjunction with the drag force imparted on a cylinder and Darcy's law to derive the velocity of fluid flow through the scaffold (V):

$$V = \frac{-K \Delta P}{\eta L}$$

where,

K: permeability (m^2)

η : fluid viscosity ($\text{kg m}^{-1} \text{s}^{-1}$)

$\Delta P/L$: pressure gradient (N m^{-3})

Volume of fluid within pores of the scaffold (ΔM), quantity of glucose consumed by this volume (ΔQ) and average residence time of fluid within this volume (T) were used to relate V to change in nutrient concentration (ΔC) within the scaffold, resulting in the following equation:

$$\Delta C = \frac{N}{n} \frac{\Delta x}{l} \frac{r}{\sigma V}$$

where,

Δx : incremental depth within scaffold (m)

Based on their model they concluded that passive glucose diffusion was unable to maintain minimum glucose concentration beyond a few hundred microns within modeled constructs. Also, the maximum depth of modeled glucose penetration was found to increase linearly with internal perfusion rate and pore size. The internal fluid flow rate, in turn, was influenced by pore volume, pore diameter and pore tortuosity of the scaffold. Their calculations indicated that static and some incorrectly designed dynamic culturing environments led to areas of nutrient concentration inadequate to sustain cell viability. They suggested a need to balance flow-induced nutrient flux with the effects of fluid shear stress, which could interfere with attachment and growth of cells on the exterior during culturing.

Malda et al.⁶⁵ measured oxygen concentrations as a function of depth within osteochondral explants and spinner flask-seeded cylindrical scaffolds, made of segmented block copolymers of alternating PEGT and PBT, using a glass microelectrode system. The microelectrode, having a tip diameter of 5 μm , was used in combination with a micromanipulator to determine oxygen profiles with a spatial resolution of 10 μm . Prior to each measurement, the electrode was calibrated using a two-point calibration with air-saturated culture media and a saturated (anoxic) sodium sulphate solution. The samples were confined by surrounding with Parafilm® so as to allow diffusion only from the top. They were placed in a flow cell perfused with air-saturated culture medium at 37° C for an hour to equilibrate. The electrode was then lowered into the constructs up to a depth of 2500 μm and oxygen concentration was recorded at 100 μm intervals during the ascent of

the electrode. The electrode was lowered at three locations on the surface of each cylindrical scaffold, including the center and the edge. At all three locations the decrease in oxygen concentration with depth followed the same trend. The increasing rapidity of this decrease with depth was attributed to greater cellularity and low diffusivity of oxygen in the constructs. Up to 27 days, oxygen tension towards the periphery of the scaffold was found to decrease faster and this was speculated to be due to higher cell concentrations in the region. However, by day 41 all three locations had almost identical profiles, owing to the chondrocyte distribution becoming more homogeneous.

They developed a mathematical model to quite accurately predict the oxygen profiles within the explants and constructs, using the following mass balance:

$$\frac{\partial C_{O_2}(x,r,t)}{\partial t} = D \left(\frac{\partial^2 C_{O_2}(x,r,t)}{\partial x^2} + \frac{\partial^2 C_{O_2}(x,r,t)}{\partial r^2} + \frac{2}{r} \frac{\partial C_{O_2}(x,r,t)}{\partial r} \right) - r_o(x,r,t)$$

with the following boundary conditions:

$$x = Z, \frac{\partial C(Z,r)}{\partial x} = 0,$$

$$x = 0, C(0,r) = C_{\text{medium}} (= 21\%),$$

$$r = R, \frac{\partial C(x,R)}{\partial r} = 0,$$

where,

C_{O_2} : local oxygen concentration (mol m^{-3})

x : distance within scaffold (m)

r : radius (m)

t : time (s)

D : diffusion coefficient of oxygen in construct ($\text{m}^2 \text{s}^{-1}$)

Z : thickness in the x direction (m)

R: radius of construct (m)

r_o : oxygen consumption rate by chondrocytes ($\text{mol m}^{-3} \text{ s}^{-1}$), given by:

$$r_o(x, r, t) = C_{\text{cell}}(x, r, t) \frac{Q_{\text{max}} C_{\text{O}_2}(x, r, t)}{K_m + C_{\text{O}_2}(x, r, t)}$$

where,

C_{cell} : cell density (cells m^{-3})

Q_{max} : maximal oxygen consumption rate ($\text{mol cell}^{-1} \text{ s}^{-1}$)

K_m : oxygen concentration at half maximal oxygen consumption (mol m^{-3})

These equations could not be solved analytically owing to their complexity and had to be solved numerically by dividing the construct into layers in the transverse and radial directions. This, however, gave them the ability to alter the value of r_o from one layer to the next, which can change dramatically as a function of cell distribution, especially as a function of depth, within the scaffold. The model was found to be very sensitive to changes in C_{cell} , Q_{max} and D . Using ranges of C_{cell} , D and K_m available from literature, the model was fitted to the measured gradients in native cartilage by varying Q_{max} . However, for the constructs, the value of r_o obtained after measuring C_{cell} , estimating D and K_m and varying Q_{max} was found to be lower than the range found for chondrocytes in native cartilage. Also, the study did not control for any architectural parameters within the scaffold. The 0.5 cm thick scaffolds were fabricated by compression molding followed by salt leaching, thereby producing a random porous structure. Moreover, the oxygen diffusion coefficient for constructs was estimated based on the assumption that diffusion took place via the shortest route possible and not via the route of least resistance. Also, measurements for oxygen concentration and cell distribution were carried out up to a depth of only 0.25 cm.

Lewis et al.⁵⁵ built on this model by incorporating cell proliferation, which was made to depend solely on local oxygen concentration. The growth rate was a product of the cellular proliferation rate and cell density. They assumed cell death to be negligible during the initial period of cell culture. The growth rate was initially modeled as a Michaelis-Menten type behavior but they found the experimental data to best fit a linear response. The dominant mechanism for cellular oxygen consumption was assumed to be entirely due to proliferation, thereby causing the oxygen consumption rate to be proportional to the growth rate. They concluded that constructs that relied solely on diffusion for their oxygen supply would always produce proliferation-dominated regions close to the periphery. They intended to enhance their model by including contact inhibition, cell senescence, inhibitor production and phenotypic changes to better explain the observed trends. They noted that in order for tissue engineering approaches to be practical, the oxygen supply to the construct center needed to exceed a simple diffusive regime and/or a reduction in the rate of cellular proliferation at the periphery. Techniques to improve oxygen supply to the scaffold interior could include tailoring of scaffold geometry to enhance flow of nutrients.

Croll et al.¹⁹ modeled the diffusion of oxygen in a 1.5-6 cm diameter dome-shaped scaffold fed by a blood vessel loop at its base. The model incorporated vascular growth, cell migration and the effect of cell density on effective oxygen diffusivity. The authors concluded that the dynamic, homogeneous cell seeding methods often employed in scaffolds of small dimensions were not applicable to large scale scaffolds and proposed the implantation of a small tissue biopsy close to the blood supply within the scaffold to ensure success. Large scaffolds homogeneously pre-seeded with cells would invariably fail even at low cell-seeding densities as cells more than a few millimeters from the nearest blood supply would eventually necrose. They also found that during

early stages of cell infiltration, the effect of cell density on the effective diffusion coefficient could be neglected as the density began to have a significant impact on diffusivity only during the consolidation phase when the scaffold was fully vascularized.

Landman et al.⁵⁰ extended the work of Lewis et al.⁵⁵ and Croll et al.¹⁹ to develop a one-dimensional model of oxygen concentration, cell proliferation and cell migration for a scaffold containing an arteriovenous loop *in vivo*. The model of a vascularized scaffold also supported a vascularization front that moved at a constant speed. Effects of vascular growth, homogeneous and heterogeneous seeding, cell diffusion as well as critical hypoxic oxygen concentration were also considered, allowing for a theoretical assessment of cell-seeding strategy in a vascularized scaffold. They concluded that heterogeneous cell seeding was the only way to reduce hypoxic conditions, provided the vascularization front moved into the scaffold quite rapidly. They justified this by noting that in case of homogeneous cell distribution, represented by soaking the scaffold in a cell solution, oxygen concentration decreased across the scaffold with the highest level at the vascularization front. Cell density increased throughout, but much more rapidly in the vascularized region or close to it, giving rise to a heterogeneous distribution of cells throughout the scaffold, with hypoxic regions being developed further away from the advancing front. In case of a heterogeneously seeded scaffold, represented by placing a small biopsy of tissue adjacent to the blood vessel, except for a narrow region at the vascularization front, almost the entire scaffold was hypoxic. During the initial period, cells would diffuse away from the front but their density would drop rapidly due to unavailability of oxygen to sustain proliferation. However, if the rate of advancement of the vascularization front was to exceed the rate of cell diffusion, the majority of cells would have access to oxygen, thereby eliminating any hypoxic region. Thus, the only

way to ensure that a construct remained non-hypoxic was to advance the vascularization front beyond the bulk of the proliferating and migrating cell population.

Shanbhag et al.⁹¹ used Brownian dynamics and Monte Carlo simulations to model effective nutrient diffusivity in scaffolds having an inverted colloidal crystal (ICC) geometry. The geometry of scaffolds possessing this structure can be described as hexagonally packed spherical cavities connected to each other by circular channels. They modeled oxygen and glucose molecules as point particles, which have no dimension and their diffusion characteristics are independent of the concentration of nutrients in the medium in which they diffuse. They determined the effective diffusivity of these molecules to be 0.3 times their diffusivity in free solution for a scaffold having spherical cavities close-packed on a face-centered cubic lattice having 12 openings. However, their model neglected the presence of cells that could occlude the cavities as well as nutrients that could adsorb on the walls of the cavity, both of which could greatly affect the concentration gradients of the nutrients as they get consumed by the cells. The authors went on to culture human stromal cells on these scaffolds and successfully modeled the effect of static and dynamic cell seeding on nutrient penetration within these scaffolds.⁹² They concluded that the performance of the scaffold could be enhanced with a judicious choice of the velocity for dynamic culturing. However, their model had not accounted for the previous limitations nor for interactions between cells, between cell colonies and between cells and the surface, all of which they hoped to incorporate in future models.

Sanz-Herrera et al.⁸⁷ geometrically characterized a specific family of scaffolds based on a face cubic centered (FCC) arrangement of pores by applying homogenization theory to a representative volume element. Cell migration within the scaffold was modeled as a diffusion process based on Fick's law while bone growth velocity was assumed to be proportional to cell concentration and regulated by mechanical stimulus in

the form of strain energy. Scaffold resorption was considered to be much slower than bone regeneration, and thus the scaffold was assumed to be nonresorbable for the purposes of analysis. The geometric model led to analytical formulae for porosity and specific surface area, which were incorporated in the equation for permeability using Kozeny's equation. The model prediction of 19 and 23% of bone regeneration for non-grafted and grafted scaffolds, respectively, both with an initial porosity of 76%, was found to be in agreement with experimental studies conducted on rabbit femurs. Bone formation was restricted to the boundary and found to be absent in the interior of scaffolds lacking an interconnected pore network.

Lemon et al.⁵⁴ formulated a multiphase model comprising motile cells and water inside a rigid scaffold material. The model also accounted for cell proliferation and variation of scaffold porosity in space. They concluded that improved cell penetration into the scaffold interior could be achieved by increasing cell motility. For the purposes of cartilage generation, this would require using mesenchymal stem cells (MSCs) rather than chondrocytes as the former are very motile and have a very high proliferative capacity relative to the latter. They also advocated perfusion of nutrients through the scaffold at a judicious flow rate during incubation to increase nutrient availability. The model did not predict a significant difference between static and dynamic cell seeding techniques as far as cell growth within the scaffold was concerned as both techniques predicted low cell densities near the center due to lack of nutrients.

Chung et al.¹⁵ developed a mathematical model incorporating cell motility due to random walks to describe the interaction between chondrocyte proliferation and glucose consumption based on a porous medium approach using a volume averaging method. The cell diffusion coefficient in the scaffold was assumed to be constant. However, they assumed the porosity of the scaffold to be so high that it did not inhibit nutrient transport.

Thus, the solid scaffold matrix was ignored and a biphasic porous medium comprising cell colony space (cells and ECM) and interstitial fluid was assumed. They advocated the design of scaffold materials and architectures favoring random walks of cells for increasing growth rates as this would help cells spread more uniformly thereby preventing them from competing for nutrients in areas where they might be localized. They further refined their model to examine the effects of media perfusion and time-dependent changes in porosity and permeability caused due to cell growth, which were modeled as a Carman-Kozeny type equation to incorporate the dependence of permeability on porosity.¹⁶ The model incorporated modified Contois cell-growth kinetics containing nutrient saturation and limited cell growth rates while nutrient consumption was defined by Michaelis-Menton kinetics.

Thus, the past couple of years have seen a surge in the area of diffusion modeling within tissue engineering scaffolds with the models getting increasingly complex and realistic to account for the various mechanical, chemical and physical stimuli that the cells growing in these environments are exposed to. Some findings, like those by Croll et al.¹⁹ and Landman et al.⁵⁰ that advocate heterogeneous cell seeding of large scaffolds seem to be quite controversial considering that research has so far advocated homogeneous cell seeding. However, it is through studies involving sophisticated modeling like those described above, that one can design studies to further confirm their claims and verify by conducting animal experiments, as performed by Sanz-Herrera et al.,⁸⁷ that will enable us to recognize and appreciate the true power of mathematical modeling and drastically reduce the time towards developing an ideal tissue engineered construct.

Chapter 3: Scaffold Fabrication Techniques

SOLVENT CASTING AND PARTICULATE LEACHING (SCPL)

The most commonly used scaffold fabrication technique is solvent casting followed by particulate leaching, wherein the pore size of the resulting scaffold is controlled by the size of the porogen, and porosity is controlled by the porogen/polymer ratio. This method involves mixing a water-soluble porogen in a polymer solution followed by casting the mixture into a mold of the desired shape. The solvent is removed by evaporation or lyophilization and the porogen is leached out by immersion in deionized water. Although salt is the most commonly used porogen, sugar as well as gelatin^{62,100} and paraffin spheres⁶⁴ are also used and these are sometimes modified to enhance scaffold functionality.⁵⁶ This method is the most widely used owing to its simplicity. However, natural porogen dispersion allows little control over the internal scaffold architecture and pore interconnectivity. Also, the thickness of the scaffold that can be fabricated by this method is hindered by difficulty removing the porogen from deep within the scaffold interior.⁶³ This has led to the modification of the SCPL technique to produce greater pore interconnectivity in some cases,^{1,64,73,109} and to new techniques like rapid prototyping (RP), also known as solid free form fabrication (SFF), in others,^{57,97,101,121} Agrawal et al.¹ modified the technique by vibrating the mold while dissolving the salt, thereby preventing the particles from settling due to gravity, thereby enhancing permeability of the scaffold by creating better pore interconnectivity and more even distribution of pores.

RAPID PROTOTYPING (RP)/SOLID FREEFORM FABRICATION (SFF)

RP techniques involve building 3D objects using layered manufacturing methods and offer several advantages over the traditional porogen leaching method, mainly independent control over the micro- and macro-scale features enabling fabrication of complex structures customizable to the shape of the defect or injury.¹⁰⁴ The process, in general, comprises the design of a scaffold model using computer-aided design (CAD) software, which is then expressed as a series of cross-sections.⁸⁶ Corresponding to each cross-section, the RP machine lays down a layer of material starting from the bottom and moving up a layer at a time to create the scaffold. Each new layer adheres to the one below it, thereby providing integrity to the finished product. Agrawal et al.⁴ and Yang et al.¹¹⁸ have provided comprehensive reviews weighing the pros and cons of traditional scaffold materials and fabrication methods. The different types of techniques encompassed by SFF include fused deposition modeling (FDM), precision extrusion deposition (PED), selective laser sintering (SLS), stereolithography (STL) and 3D printing (3DP).¹⁰¹

FDM^{12,39,84,88,121} utilizes a moving nozzle that extrudes a polymeric fiber in the horizontal plane and once a layer is completed, the plane is lowered and the procedure is repeated. PED is very similar to FDM, except that scaffold material in the form of granules or pellets is directly extruded and deposited in the form of fibers without the need of having to change these into precursor filaments as is the case with FDM.¹⁰⁷

Pressure-assisted microsyringe (PAM)¹⁰⁴ is like FDM but requires no heat and has greater resolution but cannot incorporate micropores using particulate leaching owing to the syringe dimensions. This method involves deposition of polymer solution in solvent through a syringe fitted with a 10-20 μm glass capillary needle. The solvent acts as the binding agent and the size of the polymer stream deposited can be altered by varying the

syringe pressure, solution viscosity, tip diameter of the syringe as well as speed of the motor.¹⁰⁶

SLS^{14,102,111,112} involves building objects by sintering powder on a powder bed using a beam of infrared laser. The laser beam interacts with the powder to increase the local temperature to the glass transition temperature of the powder, causing the particles to fuse to each other as well as the layer underneath.¹¹⁷ Laser power and scanning speed affect sintering significantly.²⁹ Also, control over the finished product can be achieved by varying the laser processing parameters as these, in turn, control the degree of particle fusion and porosity.²⁹

STL^{5,18,96} uses an ultraviolet (UV) laser beam to selectively polymerize a liquid photocurable monomer, a layer at a time.⁸⁶ The CAD data guides the UV beam onto the liquid surface, which is then lowered to enable the liquid photopolymer to cover the surface.

3DP involves ink jet printing of a binder onto a ceramic,^{47,90} polymer^{25,79,86} or composite^{85,94} powder surface, one layer at a time. The movement of the jet head, which dispenses the binder, is controlled by the CAD cross-sectional data. Adjacent powder particles join as the binder dissolves.⁸⁶

Some researchers have combined two or more manufacturing techniques in order to optimize their scaffold designs. Taboas et al.¹⁰¹ coupled SFF with conventional sponge scaffold fabrication techniques (phase separation, emulsion-solvent diffusion and porogen leaching) to develop methods for casting scaffolds possessing designed and controlled locally as well as globally porous internal architectures. Dellinger et al.²¹ used a SFF technique based on the robotic deposition of colloidal pastes to produce hydroxyapatite (HA) scaffolds of different architectures with porosities spanning multiple length scales. Macropores (100-600 microns) were obtained by spacing the HA rods

appropriately where as micropores (< 30 microns) were produced by including polymer microsphere porogens in the HA paste and controlling the sintering of scaffolds. Moroni et al.⁷¹ combined 3D fiber deposition and phase separation to create a shell-core fiber architecture by viscous encapsulation resulting in scaffolds with a biphasic polymer network.

The main advantage of RP techniques is their ability to finely control the microstructure and macrostructure of scaffolds and thus produce complex topographies from a computer model; their main drawbacks are the low resolutions achievable by the current systems and the types of polymeric materials that can be used.¹¹⁷ Sachlos et al.⁸⁶ have not only discussed the conventional scaffold fabrication techniques and their drawbacks but have also described various SFF techniques and how they can overcome current scaffold design limitations. Tsang et al.¹⁰⁴ have discussed the various fabrication techniques by dividing them based on their mode of assembly i.e. fabrication with heat, binders, light and molding where as Hutmacher et al.⁴¹ have described SFF techniques by dividing them based on their processing technology. Yeong et al.¹¹⁹ have well articulated the various RP techniques and their emerging sub-branches as well as compared these methods and tabulated their strengths and weaknesses.

Chapter 4: Measurement of Oxygen Concentration

Oxygen concentration has been primarily measured using one of two methods: polarographic, requiring the use of an oxygen microelectrode or phosphorescence quenching, requiring the use of oxygen sensitive material.

OXYGEN MICROELECTRODE

Revsbech⁸² developed an oxygen microsensor containing two cathodes: a sensing cathode and a guard cathode which removed all the oxygen diffusing toward the tip from the internal electrolyte reservoir. This microelectrode was found to have exceptional stability and was easy to construct. The slimmer cathodes and slimmer outer casings ensured a low diffusional supply of oxygen to the cathode tip from the electrolyte reservoir, resulting in a low residual (zero) current when exposed to anoxic environments. In this situation, the current in the measuring circuit was dependent only on the diffusional supply of oxygen to the membrane surface. However, the microsensor is extremely fragile and has to be handled with utmost care, preferably using a micromanipulator.

Mamchaoui et al.⁶⁶ used a similar system to measure oxygen consumption of intact alveolar type II cell monolayers via an open air method and an oxygraph chamber method. The open air method utilized a glass oxygen microelectrode positioned in the strict vertical position using a micromanipulator and was connected to a nanoammeter. The electrode was calibrated by immersion in cell culture medium equilibrated with pure nitrogen and air. The tip of the electrode was then brought into contact with the culture medium surface, visible by tangential illumination, and left to equilibrate for 30-60 minutes. Linear gradients were obtained while ascending the electrode from a depth of

0.18 cm in 200 micron steps, rather than while descending the electrode, probably due to the hydrodynamic profile of the electrode. The oxygraph chamber method involved using a semi-miniature Clark electrode fitted to a small (600 μ l) airtight chamber. The oxygen electrode was calibrated and equilibrated with room air following which the cell suspension was slowly introduced through an opening at the bottom of the chamber so as to drive out microbubbles through a corresponding opening in the top. The openings were closed simultaneously once the chamber was filled and the cell suspension was continuously stirred using a magnetic bar.

They found the open air method to be simple to implement, allowing measurement of oxygen consumption on intact cell monolayers as they continued to grow. The only assumptions made were that the oxygen consumption did not change during the course of measurement and that the cells were uniformly distributed at the bottom of the well. The sensitivity of this method depended on the oxygen electrode response and resolution of the amplifier. Its only drawback was the need to wait for a steady state to be established before making measurements, thereby precluding the study of transients. The oxygraph chamber, on the other hand, required an absolute seal and avoidance of trapped bubbles, both of which were difficult conditions to meet. Also, it required detachment of the cells, which may have affected their viability and metabolic properties because of the stresses that they would have been exposed to. This may have contributed to the two methods yielding similar results for only freshly isolated cells and not for cultured cells.

The oxygen microelectrode has also been used for measuring dissolved oxygen profiles in biofilms¹²⁰ and, more recently, in scaffolds⁶⁵.

PHOSPHORESCENCE QUENCHING

Oxygen-dependent quenching of phosphorescence has proved to be a powerful method for measuring oxygen concentrations in biological samples owing to its rapid response time and accurate measurement of oxygen partial pressure over the physiologically relevant range (10^{-2} -760 Torr).⁵³ Haselgrove et al.³¹ quantified oxygen consumption in chondrocytes at physiological tensions by monitoring the quenching of palladium coproporphyrin fluorescence. Cells were suspended in Hank's balanced salt solution containing 20 mM HEPES, 0.2% bovine serum albumin and 10 μ l of a solution containing 1M palladium coproporphyrin in dimethylformamide in a 0.25 ml air-tight glass cuvette. The buffer was gassed with nitrogen to reduce oxygen tension to within the physiological range, following which the cuvette was sealed and placed in a fluorometer. At intervals, the time constant of the phosphorescence quenching was measured, from which the time course of the decay of oxygen tension was calculated. These data were used to determine the cellular oxygen consumption rate as a function of oxygen concentration.

Lee et al.⁵³ used oxygen-dependent phosphorescence quenching of Pd-meso-tetra(4-carboxyphenyl)porphyrin (PdTCPP) to measure oxygen concentration in mouse liver carcinoma and human cervical carcinoma cells to study cancer treatment using photodynamic therapy. The Stern-Volmer relationship was used to convert measured phosphorescence using the equation

$$I_0/I = \tau_0/\tau = 1 + K_q \tau_0[\text{O}_2]$$

where,

I_0 and I are phosphorescence intensities in the absence and presence of oxygen concentration $[\text{O}_2]$, respectively

τ_0 and τ are lifetimes in the absence and presence of oxygen, respectively

K_q is the biomolecular quenching constant

The oxygen concentration can be replaced with oxygen partial pressure to obtain

$$pO_2 = (1/K_q)(1/\tau - 1/\tau_0)$$

Kellner et al.⁴⁶ used oxygen-sensitive luminescent optical sensor foils to generate two-dimensional maps of oxygen distribution over cartilage cross-sections. The calculation of oxygen pressures from the accumulated raw data were based on the fact that the luminescent light emitted from the porphyrin sensor was quenched in a concentration-dependent manner by the presence of oxygen. They too used a form of the Stern-Volmer equation to calculate the oxygen partial pressure.

MATERIALS AND METHODS

Chapter 5: Construct Specifications

SCAFFOLD MATERIAL AND METHOD OF FABRICATION

We were interested in studying the effect of scaffold architecture on oxygen diffusion and cell function in the scaffold interior and thus needed to use a fabrication technique that could produce scaffolds having a desired internal structure. Since SCPL has little control over the internal scaffold architecture and pore interconnectivity we had to turn to SFF techniques to fabricate our scaffolds. However, since we did not have the capability to fabricate scaffolds using SFF at our university, we were fortunate to collaborate with Dr. Wei Sun, Associate Professor, Department of Mechanical Engineering and Mechanics, Drexel University, Philadelphia, PA. The bio-manufacturing facility in his laboratory had a precision extrusion deposition (PED) system that could generate scaffolds according to our specifications. Scaffold fabrication using the PED system has been described earlier (Chapter 3). All of the scaffolds were manufactured using the 0-90° laydown pattern i.e. the fibers in adjacent layers were laid down perpendicular to one another, with the nozzle temperature maintained at 90° C. Sheets of the scaffold material of dimensions 4 cm x 3 cm x 1 cm were generated, from each of which 6 cylindrical scaffolds of heights and diameters 1 cm were bored out.

We decided to use PCL as the scaffold material as it is suitable to fabricate scaffolds using the PED system and has been widely used for bone and cartilage applications. Although our project did not entail the generation of bone or cartilage tissue, we planned to use osteoblast-like cells, thereby further justifying the use of PCL. PCL is a biocompatible, semicrystalline, bioresorbable polymer with favorable properties

for thermoplastic processing and has one of the slowest degradation rates of all biodegradable polymers. The slow rate of degradation was ideal from a modeling point of view as well, since the model assumed that there would be no scaffold degradation over the duration of the study, which lasted 1 week. PCL has a melting temperature of 60° C and a glass transition temperature of -60° C. PCL was obtained from Aldrich, St. Louis, MO in pellet form. Its molecular weights were M_n 42,500 Da and M_w 65,000 Da.

CELL TYPE SELECTION

MG63 cells (ATCC, Manassas, VA), which are human osteoblast-like osteosarcoma cells, were chosen because they are a homogeneous (clonal) population, are well-characterized and easy to culture. They represent an immature stage in osteogenic differentiation and respond to 1,25(OH)₂ vitamin D₃ and parathyroid hormone by producing increased amounts of alkaline phosphatase specific activity. In addition they have an unknown defect which prohibits normal extracellular matrix production and mineralization. Also, since they are osteosarcoma cells they undergo unregulated proliferation and do not display contact inhibition.

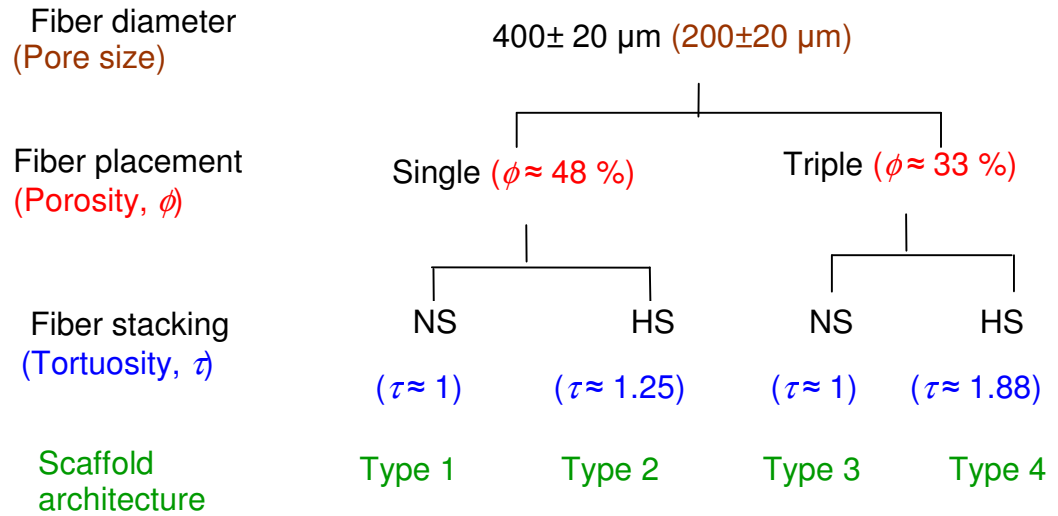
SCAFFOLD ARCHITECTURAL PARAMETER SELECTION

The primary architectural parameters of interest were porosity and permeability. We were interested in determining how scaffolds of the same porosity, but having different permeabilities, would affect cell behavior and oxygen diffusion within the scaffold. For this we had to introduce the effect of tortuosity in the scaffold fabrication procedure. From a review of the literature of scaffolds used for bone regeneration we determined that an appropriate pore or channel size to select would be 200 microns. This would be suitable for the static seeding of MG63 cells as well, since their size is in the tens of microns and this would allow them to penetrate deep within the scaffold. In order to

come up with values of tortuosity having a large enough difference between them to seem to have a significant effect on the permeability, the porosity of the scaffolds had to be compromised. A review of the literature revealed the need for having a scaffold with high porosity for ensuring cell growth within the scaffold. However, our need to maximize differences in tortuosity, coupled with the resolution of the PED system, dictated the porosity and permeability of the resulting scaffolds. Figure 1 has a chart depicting the different scaffold architectural parameters selected. Thus, we obtained scaffolds with 4 distinct architectural parameter combinations (Types 1, 2, 3 and 4). All 4 kinds of architectures had the same fiber diameter (400 microns) and pore size (200 microns). The placement of the PCL fibers as either single (Figure 2) or in triplicate (Figure 3) during the PED process determined the porosity of the resulting cylindrical scaffolds of diameter 1 cm and height 1 cm. The way the fibers in alternate layers were staggered with respect to one another dictated the tortuosity of the scaffolds, which was estimated from their side view. Porosity was also estimated from the side views as shown in Figure 4. Since the scaffold fibers had a very regular structure and the internal architecture was well known, estimation of porosity by this method was felt to be fairly accurate and was verified by carrying out measurements using a helium pycnometer.

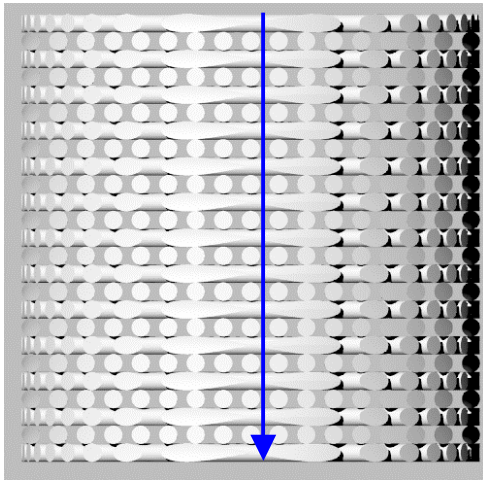
The porosity and permeability measurements were carried out on scaffolds whose top and bottom ends were left unaltered while the scaffolds used for cell studies and oxygen concentration measurements had an impermeable layer of PCL sealing the bottom. This layer was incorporated during the PED fabrication process itself to prevent diffusion of nutrients from the bottom in order to maximize the depth up to which we could study one-dimensional oxygen diffusion. In addition to this, the scaffolds with the sealed bases were surrounded with a biocompatible tubing of low oxygen permeability

during the experiment to minimize diffusion of oxygen into the scaffolds from the sides, thereby resulting in the scaffolds having only their tops exposed for oxygen diffusion.

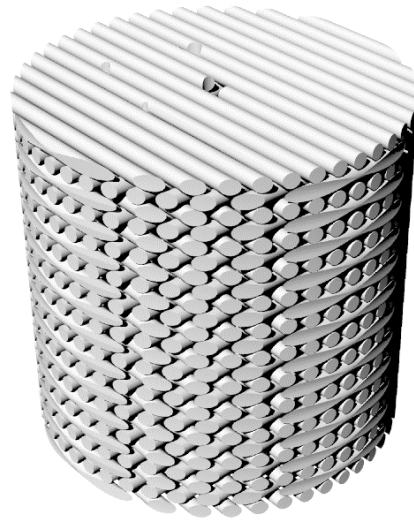


NS: Not Staggered; HS: Highly Staggered
 ϕ : Porosity; τ : Tortuosity

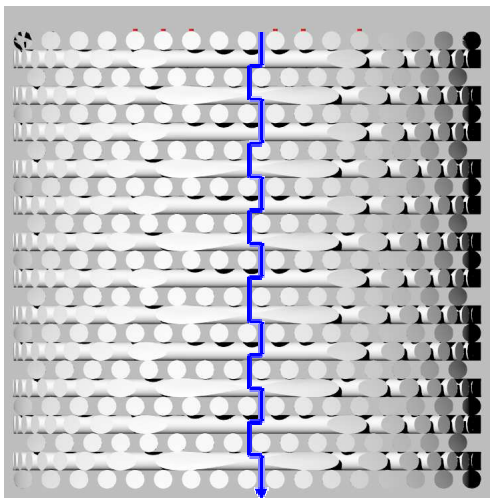
Figure 1. Scaffold architectural parameters selected.



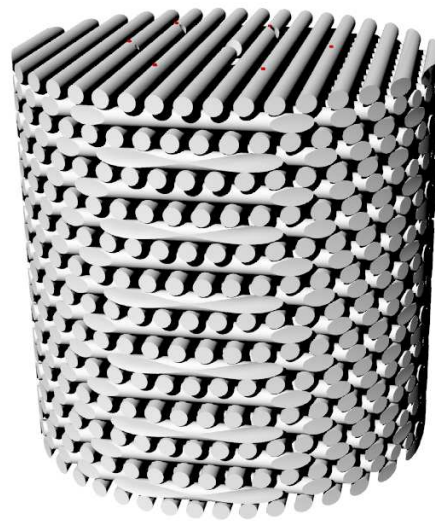
(a)



(b)

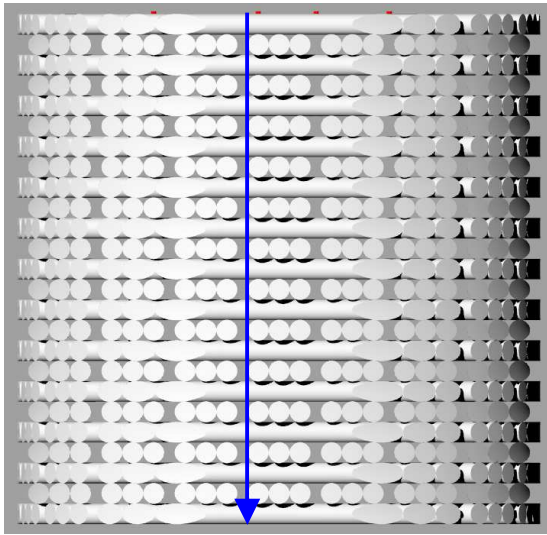


(c)

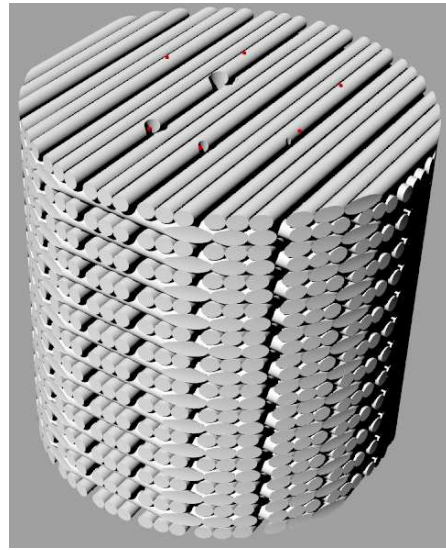


(d)

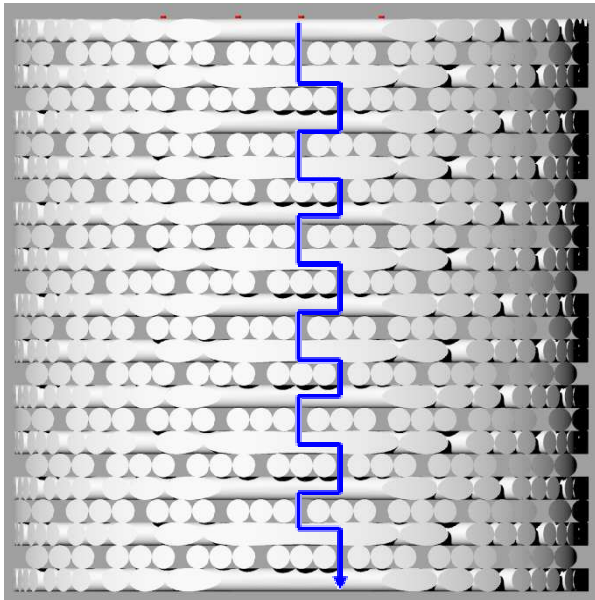
Figure 2. Type 1 (a) side view, (b) isotropic view. Type 2 (c) side view, (d) isotropic view. Images were generated using Rhinoceros® (McNeel North America, Seattle, WA). The blue arrows indicate the probable path that fluid would take to go from top to bottom if it follows the path of least resistance and is used to estimate tortuosity.



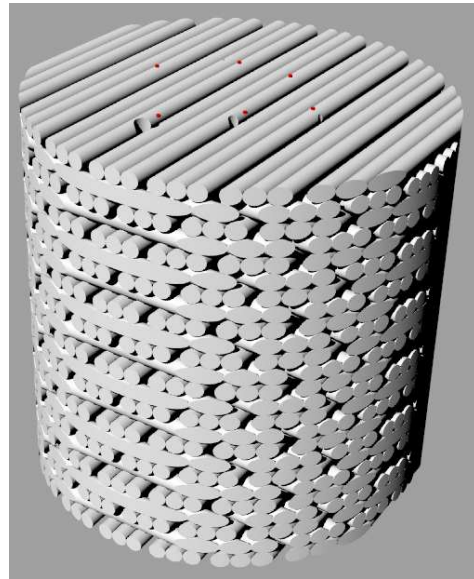
(a)



(b)



(c)



(d)

Figure 3. Type 3 (a) side view, (b) isotropic view. Type 4 (c) side view, (d) isotropic view. Images were generated using Rhinoceros® (McNeel North America, Seattle, WA). The blue arrows indicate the probable path that fluid would take to go from top to bottom if it follows the path of least resistance and is used to estimate tortuosity.

Porosity = $\frac{\text{Area of empty space}}{\text{Area of rectangle}}$

= $\frac{\text{Area of rectangle} - \text{Area of 2 semicircles}}{\text{Area of rectangle}}$

= $\frac{2R(2R+x) - \pi \cdot R^2}{2R(2R+x)} = \frac{2(2R+x) - \pi \cdot R}{2(2R+x)}$

= $\frac{(6 - \pi)R}{6R} = \frac{2.857 * 100}{6} = 47.6\% \sim 48\%$

(a)

Porosity = $\frac{\text{Area of rectangle} - \text{Area of 3 circles}}{\text{Area of rectangle}}$

= $\frac{2R(6R+x) - 3\pi \cdot R^2}{2R(6R+x)} = \frac{2(6R+x) - 3\pi \cdot R}{2(6R+x)}$

= $\frac{14 - 3\pi}{14} = 0.3265 = 32.7\% \sim 33\%$

(b)

Figure 4. Estimating porosity from side view of scaffold schematics for architectures of (a) Type 1 and 2, (b) Type 3 and 4.

Chapter 6: Measurement of Scaffold Porosity

A helium pycnometer (AccuPyc 1330, Micromeritics, Norcross, GA) was used to measure the porosity of the scaffolds of Types 1-4 (n = 6 for Types 1 and 2, n = 4 for Types 3 and 4). The number of samples for Types 1 and 2 were greater than those for Types 3 and 4 as two samples from each of the lower porosity group were damaged. The scaffolds used here were the same ones used for permeability measurements. Care was taken to see that the samples were dry and handled with forceps. Three repeated measurements were taken on each of the samples of each of the four types of scaffolds. The output of the pycnometer was recorded, following which vernier calipers were used to measure the height and diameter of each scaffold in order to determine its volume. The output of the pycnometer was subtracted from the calculated volume of the scaffold to obtain the porosity (Table 1).

Table 1. Porosity of scaffolds

	Type of scaffold architecture			
	Type 1 (n = 6)	Type 2 (n = 6)	Type 3 (n = 4)	Type 4 (n = 4)
Mean porosity (%)	42.32	46.5	25.38	26.72
Standard deviation (%)	0.63	0.65	1.67	1.58
Estimated porosity (%)	47.6	47.6	32.7	32.7
Difference in porosity (%)	5.28	1.1	7.32	5.98

Chapter 7: Measurement of Scaffold Permeability

A device, termed the permeability tester, was designed and fabricated in order to quantify the permeability of the architecturally distinct scaffolds. The device comprised a long PVC pipe with a ball valve near its lower end to control the flow of water (Figure 5). The lower end of the pipe penetrated a dismountable polycarbonate adapter, which helped connect the pipe to the aluminum platform supported on four legs. The specimen whose permeability had to be measured was press-fitted into a hole in the aluminum platform. The diameter of the hole was just slightly less than 1 cm so as to provide a snug fit to the scaffold. Once the specimen was press-fitted into the hole and its upper surface was flush with the upper surface of the metal platform, the polycarbonate base was secured over the hole with screws. An empty graduated beaker was placed below the hole to collect the deionized water flowing down the hole. The upper end of the PVC tube had a hose barb that helped connect the tube to an open water reservoir via a silicone tube. The reservoir had a large cross-sectional area and a stopcock to control the flow of water. The reservoir needed to be kept open in order to expose it to atmospheric pressure. It had a large cross sectional area so as to maintain a relatively low change in hydrostatic pressure during the course of measuring permeability (k). The stop cock on the water reservoir and the valve on the metal tube were opened to allow a certain volume of deionized water (Q) to pass through the specimen and collect in the graduated beaker. The duration ($t = 10$ seconds) over which this volume was collected was measured using a stop watch with a least count of 1 second. The hydraulic head (h) i.e. height of the water level in the reservoir measured from the top of the scaffold and expressed in pressure units (Pa), was measured using a tape and maintained at 1 meter. Since the cross sectional area of the reservoir was large, it did not have to be filled with water very often to maintain the hydraulic head at

100 cm. The length of the specimen ($L = 1$ cm) and its cross-sectional area ($A = \pi*d^2/4$, where $d = 1$ cm) were known. The viscosity of water ($\mu = 1$ centipoise) ($1 \text{ cp} = 0.001 \text{ Pa}\cdot\text{s}$) is also known. Thus, permeability was calculated using a form of Darcy's Law: $k = Q.\mu.L / (h.A.t)$. The units for permeability are m^2 or Darcy (D), where $1\text{D} = 10^{-12} \text{ m}^2$.

Before starting the experiment, all scaffold samples were submerged in deionized water so as to ensure removal of air bubbles. Once a scaffold was press-fitted into the hole of the aluminum table and the tester assembled, water from the reservoir was allowed to flow through the tubing and pipe to remove any trapped air from the flow path, which would be visible in the form of a distorted water front descending through the transparent tubing. Each sample was subjected to 3 repeated measurements. The number of samples for Types 1 and 2 ($n = 6$) were greater than those for Types 3 and 4 ($n = 4$) as two samples from each of the lower porosity group were damaged. Figure 6 shows the mean values for permeability \pm SD. The permeability data were analyzed for statistical differences using a 1-way ANOVA followed by a Tukey's test at the 0.05 level of significance. It revealed that there were significant differences between Types 1 and 3, Types 1 and 4, Types 2 and 3, and Types 2 and 4. There were no significant differences between architectures of the same porosity (Types 1 and 2, and Types 3 and 4).

We were also interested in measuring tortuosity of the different architectures to see how they would relate to the values we estimated. However, measuring tortuosity is extremely difficult as it is very tedious to experimentally determine the flow path length for the fluid through the scaffold. In order to accurately measure tortuosity one would need to track the fluid front from the time it impacts the top of the scaffold till the time it exits the bottom in order to quantify the flow path length. Since this proved to be a daunting task, we decided to calculate retention time of the fluid within the scaffold to reflect its tortuosity. A scaffold whose architecture is more tortuous would retain fluid for

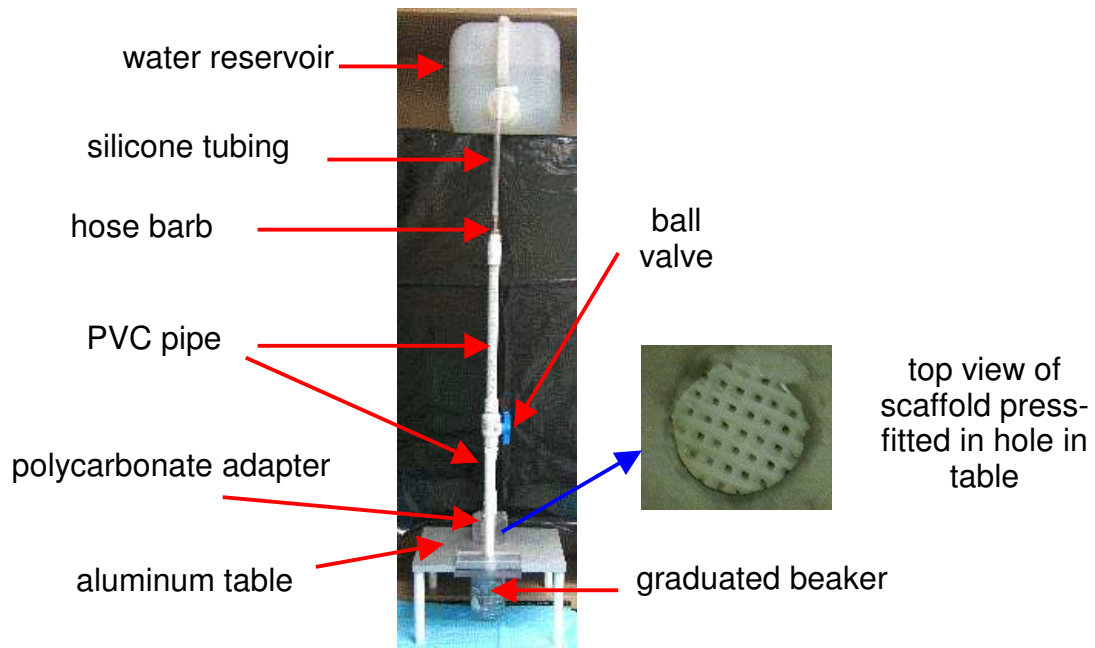


Figure 5. Permeability tester.

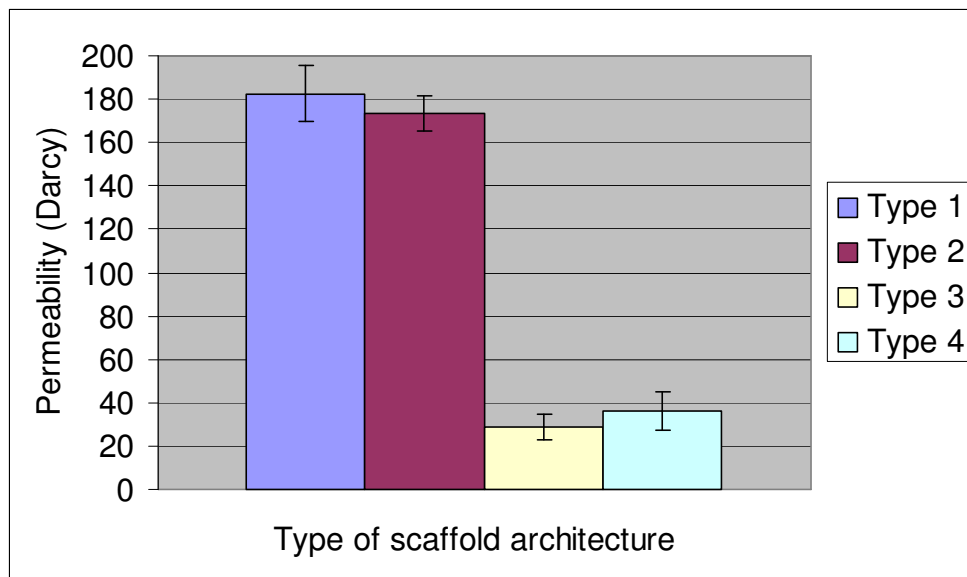


Figure 6. Permeabilities of different scaffold architectures.

longer and would be less permeable. The parameters measured for calculating permeability were also used for calculating water retention time (T seconds) within the scaffold. For this purpose, volumetric flow per unit area (q) was determined using $q = Q/A.t$ with units of velocity (m/s). Further, velocity of water within the pores (v) was calculated using $v = q/\phi$, where ϕ is the mean measured porosity from Table 1. Thus, $T = 0.01/v$, where 0.01 represents the length of scaffold expressed in meters. Figure 7 depicts the mean values \pm SD for water retention time calculated for the various scaffold architectures. The water retention time data were analyzed for statistical differences using ANOVA followed by a Tukey's test at the 0.05 level of significance. Once again, significant differences were observed only between scaffolds of different porosities.

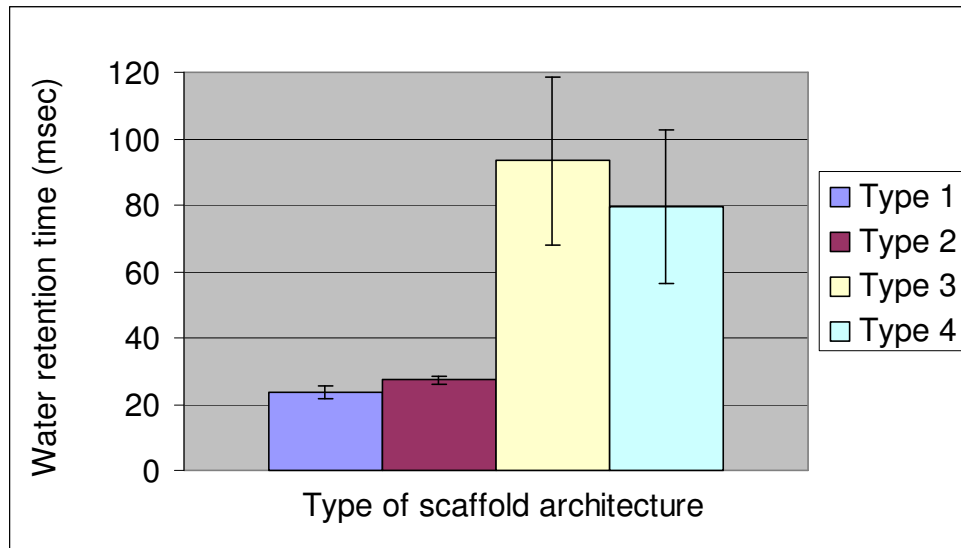


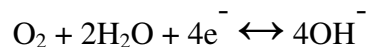
Figure 7. Water retention times for different scaffold architectures.

Chapter 8: Measurement of Oxygen Concentration

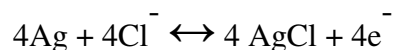
A Clark-style glass oxygen microelectrode with a guard cathode (Unisense, Aarhus N, Denmark) having a tip diameter of 500 microns and surrounded by a 21 gauge (0.081 cm) hypodermic needle of length 4 cm, was used for measuring oxygen concentration. The needle functioned as a sheath to protect the extremely fragile sensor tip as it descended into the construct. The tip of the needle was beveled and raised slightly above the sensor tip thereby exposing the sensor tip while simultaneously protecting it from mechanical damage. The Clark-style sensor comprised an internal oxygen cathode, reference anode and an electrolyte. An outer glass housing with a small silicone membrane separated the sensor components from the measurement sample. The guard cathode served the purpose of consuming oxygen from the internal electrolyte solution thereby lowering the background signal of the electrode and increasing its resolution, especially at or near anoxic conditions in addition to increasing response time.

THEORY OF POLAROGRAPHIC OXYGEN MEASUREMENT

The Clark-style microelectrode is a polarographic electrode that requires an externally supplied potential (from the dissolved oxygen meter) to function and consumes a negligible amount of oxygen. When two electrodes are polarized with a potential of somewhat less than -1 V in an electrolytic solution containing dissolved oxygen, current will flow as a result of the reduction of oxygen at the cathodic (negatively polarized) surface. The reaction at the cathode can be expressed as:



while oxidation occurs at the anode:



The voltage-current relationship for a polarographic oxygen electrode is linear below -0.5 V reaching a plateau from -0.5 to -1 V and then again increasing. In the plateau region the current is limited by the rate at which oxygen can diffuse to the cathode. Thus, an oxygen electrode operated at a polarization voltage set to the midpoint (-0.8 V) of the plateau region will be diffusion limited, wherein virtually all of the oxygen molecules reaching the cathode are immediately reduced, resulting in zero oxygen concentration at the cathode surface and a current that is limited by the rate at which oxygen can diffuse to this zero concentration region. The diffusion rate is a function of the oxygen diffusion coefficient of the membrane and media surrounding the cathode as well as dissolved oxygen concentration, which, in turn, is proportional to the oxygen partial pressure, temperature and salinity.

APPARATUS FOR OXYGEN CONCENTRATION MEASUREMENT

A manual micromanipulator (Marzhauser, Germany) with a resolution of 0.001 cm and range of 5 cm in the vertical direction was used to secure and move the oxygen sensor (Figure 8). The oxygen sensor connected to a chemical microsensor (Diamond General, Ann Arbor, MI) that was used for calibrating the sensor as well as recording the output (Figure 9). Before each pair of measurements on a scaffold without cells (control) and a scaffold with cells (sample), the sensor was calibrated using a two-point calibration. This comprised alternately exposing the sensor tip to the maximum and minimum concentrations of oxygen that the sample would be exposed to in the incubator, which was maintained at 5% CO₂ and 37° C, and then accordingly adjusting the microsensor output to 21% and 0% respectively, corresponding to the concentration of oxygen in the gas-saturated media. For this purpose, a dual chamber calibration cell (Diamond General, Ann Arbor, MI) containing 2 calibration vessels, each with its own

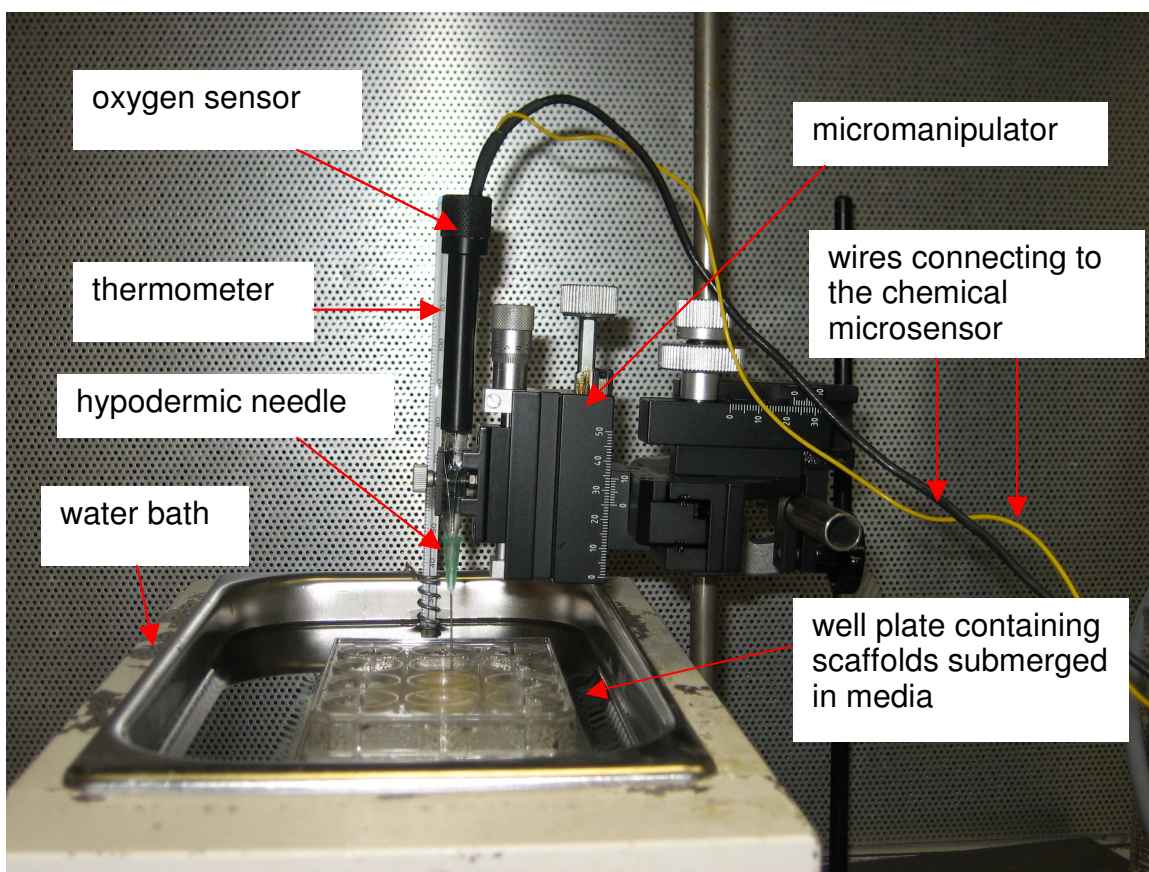


Figure 8. Measurement of oxygen concentration



Figure 9. Chemical microsensor

valves and gas dispersion tubes and submerged under deionized water, were used (Figure 10). The gas dispersion tube from one vessel connected to a gas cylinder (Praxair Distribution, Inc., Austin, TX) containing a gaseous mixture comprising 5.1% CO₂, 20.9% O₂ and balance N₂, corresponding to the maximum concentration of oxygen that the scaffold would be exposed to, while the tube from the other vessel connected to a gaseous cylinder comprising 5% CO₂ and balance N₂, which is basically 0% O₂ and corresponded to the lowest concentration of oxygen that the scaffold would experience (Figure 11). The media in each calibration vessel through which the calibration gases were bubbled should have ideally been the same as that in which the scaffolds were being cultured. However, this resulted in a lot of protein adsorption and deposition on the conduits used for bubbling the gas through the media and required frequent cleaning and disassembling of the apparatus. Thus, saline having salinity (0.64%) equal to that of Dulbecco's Modified Eagle Medium (DMEM) that formed the major component of our culture media, was used instead. Since oxygen concentration also depends on temperature, an immersion thermostat (Lauda, Germany) set to 37° C was used for warming the water in the calibration cell for conducting the sensor calibration.

CALIBRATION OF SENSOR

A day prior to the measurement of oxygen concentration, the calibration chamber was filled with deionized water up to 2 cm from the top. 80 ml of saline (0.64 %) was poured in the 2 calibration vessels. The sensor was clamped to a stand and lowered into one of the beakers and left to stabilize at the operating voltage (-0.80 V) and at the temperature (37° C) at which measurements were going to be made, for at least 1 hour. If the sensor had not been used for a week, it was polarized for at least 12 hours.

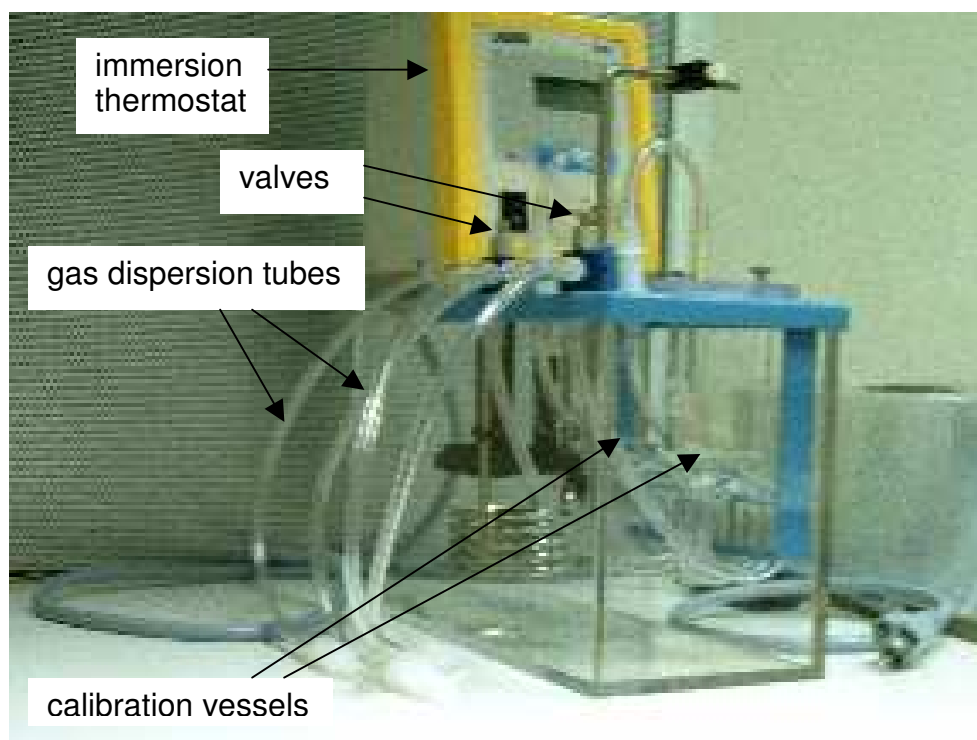


Figure 10. Calibration cell

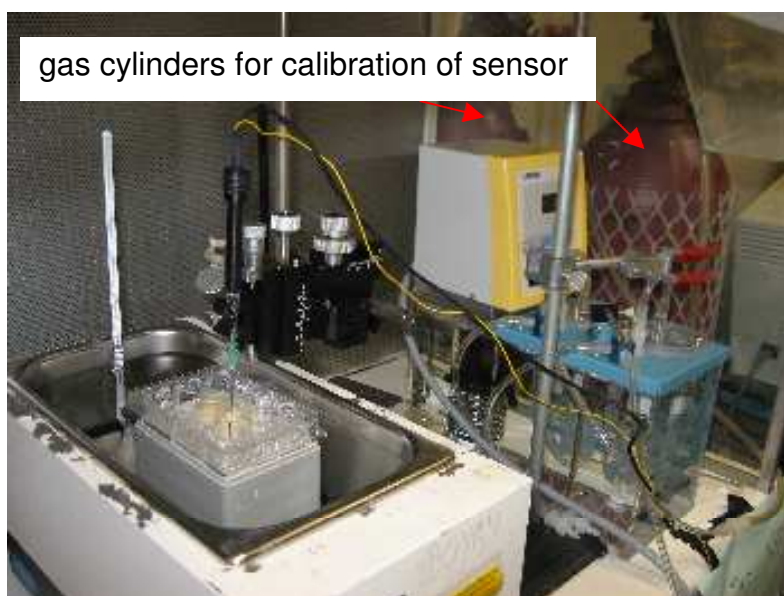


Figure 11. Apparatus for oxygen concentration measurement

Since oxygen partial pressure and current have a linear relationship, a two point calibration was used, meaning that the electrode response in two solutions with known oxygen concentrations was determined. The two known oxygen concentrations selected were the extremes that the cell-seeded scaffold would be exposed to. For this purpose, gas supplies were connected and the pressure adjusted such that a moderate stream of bubbles was released through the saline. First, the microelectrode tip was immersed in the calibration vessel bubbled with the maximum oxygen concentration for 5 minutes, which was sufficient time to saturate the saline with oxygen and for the meter reading to stabilize. The coarse and fine gain knobs were then adjusted for the chemical microsensor to read 21.0%. Next, the microelectrode tip was immersed in the other calibration vessel and the oxygen depleted gas was bubbled through the solution for 5 minutes. After the reading stabilized the coarse and fine zero controls were adjusted for the microsensor to reflect a reading of 0.0. These two steps of setting the microsensor reading at the higher and lower oxygen concentration values were repeated until constant readings were obtained at both ends of the scale without requiring any further adjustment of the 'gain' or 'zero' setting knobs. Once this was accomplished, a properly polarized microelectrode gave a linear output across the calibrated range.

PROTOCOL FOR MEASUREMENT OF OXYGEN CONCENTRATION

Eight cylindrical PCL scaffolds (two of each Type (Type 1, 2, 3, 4)) of height 1cm and diameter 1cm with a hole drilled through their center just short of penetrating their impermeable base, were immersed in 70% ethanol and placed under UV light overnight for sterilization. The scaffolds were then thoroughly washed thrice with sterile Dulbecco's Phosphate Buffered Saline (DPBS) 1X, without calcium chloride and without magnesium chloride (Gibco®, Invitrogen, Carlsbad, CA) by vigorous pipetting to remove

any remaining traces of ethanol before submerging in a solution of fibronectin from bovine plasma (Sigma-Aldrich, St. Louis, MO) in PBS (20 µg/ml) to enhance cell attachment. 1.5 ml of the above solution was sufficient to submerge a single scaffold placed in a 24 well plate. The scaffolds were once again subjected to vigorous pipetting in the fibronectin solution so as to cause the scaffold to be uniformly coated with fibronectin. These submerged scaffolds were then placed in the incubator maintained at 5% CO₂ and 37° C for 4 hours.

Thereafter, scaffolds were handled with autoclaved forceps to press-fit them within autoclaved rings of height 1cm placed in 12 well plates, such that the tops of the rings were flush with the tops of the scaffolds. These rings were cut from a piece of PharmaPure™ tubing (Saint-Gobain, Akron, OH) of internal diameter 3/8 inch (0.95 cm) and external diameter 5/8 inch (1.59 cm). This tubing was selected for its excellent biocompatibility as well as nontoxic and nonhemolytic properties in addition to low oxygen permeability (200 x 10⁻¹¹ cm³.cm/cm².s.cm Hg). The permeability coefficient was provided by the manufacturer and calculated using the formula, permeability coefficient = amount of gas (cm³) x tubing wall thickness (cm) / surface area of tubing internal diameter (cm²) x time (s) x pressure drop across tubing wall (cm Hg). 100 µl of full media (89% DMEM (Cellgro®, Mediatech, Herndon, VA), 10% fetal bovine serum (Atlanta Biologicals, Lawrenceville, GA), 1% penicillin/streptomycin (Gibco®, Invitrogen, Carlsbad, CA)) was added atop each scaffold following which a pellet of 2 million MG63 cells in 50 µl of full media was deposited evenly across the top of four scaffolds (samples), one of each Type. No cells were added to the remaining four scaffolds (controls) comprising one of each Type.

Hypodermic needles (18 gauge, ½ inch (0.127 cm)) (Air-Tite Products Co., Inc, Virginia Beach, VA) were previously modified by removing their plastic bases and

beveled tops and five holes were drilled into their side at regular intervals of 0.2 cm in order to facilitate free movement of nutrients and waste into the part of the needle that would be immersed within the scaffold. These modified needles were autoclaved and their ends having the holes were inserted head first into the hole at the center of each sample and control using sterile forceps. The needles were pushed down till they could be pushed down no further, indicating their bottom had contacted the impermeable scaffold base. The diameter of the hole was selected so as to provide a snug fit to the needle once inserted. A drill bit of diameter 0.13 cm was used to drill the hole. The open end of the needle on top was then covered with a circular disc of diameter 0.5 cm having adhesive on the bottom ('bindi') that stuck firmly to the needle top thereby minimizing diffusion of gases across the top of the needle.

The samples and controls were then placed in the incubator for an hour to allow enough time for the cells to attach to the scaffold. The samples and controls were then gradually submerged in full media containing HEPES (25mM) (Invitrogen, Carlsbad, CA) by the slow addition of media from the sides of each well up to a level such that the media was just able to cover the top of the scaffold. HEPES acted as a buffer in order to maintain pH as the cells were exposed to different concentrations of CO₂ in the incubator (5%) and the laboratory (~0.03%). Each well plate containing a single sample and control pair of each Type was incubated and media was replaced every second day.

On the days of interest (days 1 and 7), the sensor was calibrated as described above. Simultaneously, the well plate containing the sample and control of Type 1 was placed in the water bath maintained at a certain temperature so as to ensure that the contents of the well plate were at 37° C (Figure 12 (a)). The lid of the well plate was removed and 2 pairs of forceps were used to remove the needle covered by the 'bindi' on

top: one pair to hold down the ring surrounding the scaffold and the other pair to pull out the needle with the attached 'bindi'. The sample and control were left uncovered in the well plate for 1 hour for them to equilibrate with the laboratory atmosphere (20.9% O₂, 25° C) (Figure 12 (b)). Ideally, oxygen concentration should be measured under the same conditions that the constructs were cultured under (5%CO₂, 37° C). However, it is currently impractical to have such a robust set up in an incubator-like environment. Also, the time period between taking out the constructs from the incubator and beginning the measurements needs to be minimized so as to be able to capture the true effect of scaffold architecture on oxygen diffusion. Preliminary experiments revealed that a period of 1 hour was required for transient effects arising due change in atmospheric conditions of the incubator and the laboratory work area to subside. Thus, measurements were carried out on the control and then the sample at the end of an equilibration period of 1 hour.

For the purpose of actually taking the measurement, the calibrated sensor was positioned over the control in the well plate using the micromanipulator. The sensor was carefully descended into the hole at the center of the control and readings were recorded at 0.1 cm intervals beginning at the top of the hole while descending into the scaffold (Figure 13). The reading for oxygen concentration at each depth of interest was read off the display of the chemical microsensor once it stabilized. Once the sensor could descend no further, readings were taken while retracting the sensor, halting at 0.1 cm intervals. The procedure was repeated for the corresponding sample. After the measurements were complete for a control-sample pair of one Type, the pair was returned to the incubator for performing cell viability studies using calcein AM (Molecular Probes, Eugene, OR).

The procedure was repeated for all other types of scaffold architecture pairs. This completed one set. Measurements on two more sets comprising a control-sample pair



(a)

(b)

Figure 12. Constructs just removed from the incubator (a) placed in the water bath; (b) being equilibrated.



Figure 13. Hypodermic needle surrounding the sensor being descended into the construct.

analyzed for oxygen concentrations on days 1 and 7 were performed for a total of 3 sets (i.e. n = 3) (Table 2). For a few samples, oxygen concentration was measured at 0.01 cm incremental depths in the top 0.4 cm so as to get a more detailed profile as one would expect to see the maximum changes occurring in this region.

In order to compare the oxygen concentration profiles to one another as well as correlate with the cell viability and cell proliferation findings, the mean values for oxygen concentration were computed for the top (0-0.3 cm), middle (0.4-0.6 cm) and bottom (0.7-0.9 cm) parts of the samples. A 3-way ANOVA was performed on these means to determine if significant differences existed at the 0.05 level of significance.

Table 2. Selection of control(c) and sample(s) scaffolds for oxygen concentration measurement

Set No.	Day 1				Day 7			
	Type of scaffold architecture				Type of scaffold architecture			
	1	2	3	4	1	2	3	4
1	1 c, 1 s	1 c, 1 s	1 c, 1 s	1 c, 1 s	1 c, 1 s	1 c, 1 s	1 c, 1 s	1 c, 1 s
2	1 c, 1 s	1 c, 1 s	1 c, 1 s	1 c, 1 s	1 c, 1 s	1 c, 1 s	1 c, 1 s	1 c, 1 s
3	1 c, 1 s	1 c, 1 s	1 c, 1 s	1 c, 1 s	1 c, 1 s	1 c, 1 s	1 c, 1 s	1 c, 1 s

Chapter 9: Measurement of Cell Viability

Cell viability in the structurally distinct scaffolds was detected using calcein AM (acetoxymethyl) (Molecular Probes, Eugene, OR). In live cells the nonfluorescent calcein AM is converted to a green-fluorescent calcein, after AM ester hydrolysis by intracellular esterases. Calcein AM is retained in cells that have intact membranes. It does not label dead cells and is rapidly lost under conditions that cause cell lysis. Twelve cylindrical PCL scaffolds (six each of Type 1 and 2) ($n = 3$) of height 1cm and diameter 1cm with impermeable bases were immersed in 70% ethanol and placed under UV light overnight for sterilization. The scaffolds were then thoroughly washed thrice with sterile DPBS by vigorous pipetting to remove any remaining traces of ethanol before submerging in a solution of fibronectin in PBS (20 $\mu\text{g/ml}$) to enhance cell attachment. 1.5 ml of the above solution was sufficient to submerge a single scaffold placed in a 24 well plate. The scaffolds were subjected to vigorous pipetting with the fibronectin solution so that the scaffold would be uniformly coated with fibronectin. These submerged scaffolds were then placed in the incubator maintained at 5% CO_2 and 37° C for 4 hours.

Thereafter, scaffolds were handled with autoclaved forceps to press-fit them within autoclaved PharmaPure™ tubing rings of height 1cm placed in 12 well plates, such that the tops of the rings were flush with the tops of the scaffolds. 100 μl of full media was added atop each scaffold following which a pellet of 2 million MG63 cells in 50 μl of full media was deposited evenly across the top of the scaffolds (samples). The samples were then placed in the incubator for an hour to allow enough time for the cells to attach to the scaffold. The samples were then gradually submerged in full media by the slow addition of media from the sides of each well up to a level that the media was just able to cover the top of the scaffold. Media were replaced every second day.

At the first time point of interest (day 1) the ring surrounding a sample was removed and the sample was washed gently in DPBS thrice to remove serum esterase activity that is generally present in serum-supplemented growth media, as serum esterases could cause some increase in extracellular fluorescence by hydrolyzing calcein AM. Gentle washing is required as cells could detach from the scaffold if washing is vigorous. 1 ml of DPBS was added to previously prepared 5 μ l aliquots of calcein AM to form a working concentration of 5 μ M, which were covered with aluminum foil to keep them protected from light in order to retain their activity. Each sample was submerged in the working solution and placed in the incubator (5%CO₂, 37° C) for 60 minutes.

At the completion of 1 hour, the calcein AM-treated scaffold was vertically sectioned simultaneously into four divisions: left side, left middle, right middle and right side using a custom-made three-pronged box cutter having titanium edge blades (Lenox, East Longmeadow, MA). A hammer was used on the rear end of the device to facilitate cutting the construct. The left middle and right middle divisions had two sides each, therefore resulting in a total of six surfaces (Figure 14) that were imaged under a Leica MZ16 FA fluorescence stereomicroscope (Heerbrugg, Switzerland) using a 0.5X objective at a magnification of 40.7, resulting in a zoom of 20.35. Calcein AM has an absorption maximum around 492 nm and an emission maximum around 517 nm. Thus, a mercury arc source was used for exciting the cells and a green fluorescence protein (GFP) filter was used for isolating the emission spectra from the cells that were fluorescing, indicative of their being viable. For ease of comparing and visualizing, the construct surface to be imaged was divided into a maximum of six parts: top left, top right, middle left, middle right, bottom left and bottom right (Figure 15). Thus, a single scaffold could ideally yield a maximum of 36 parts (6 surfaces with each surface having 6 parts).

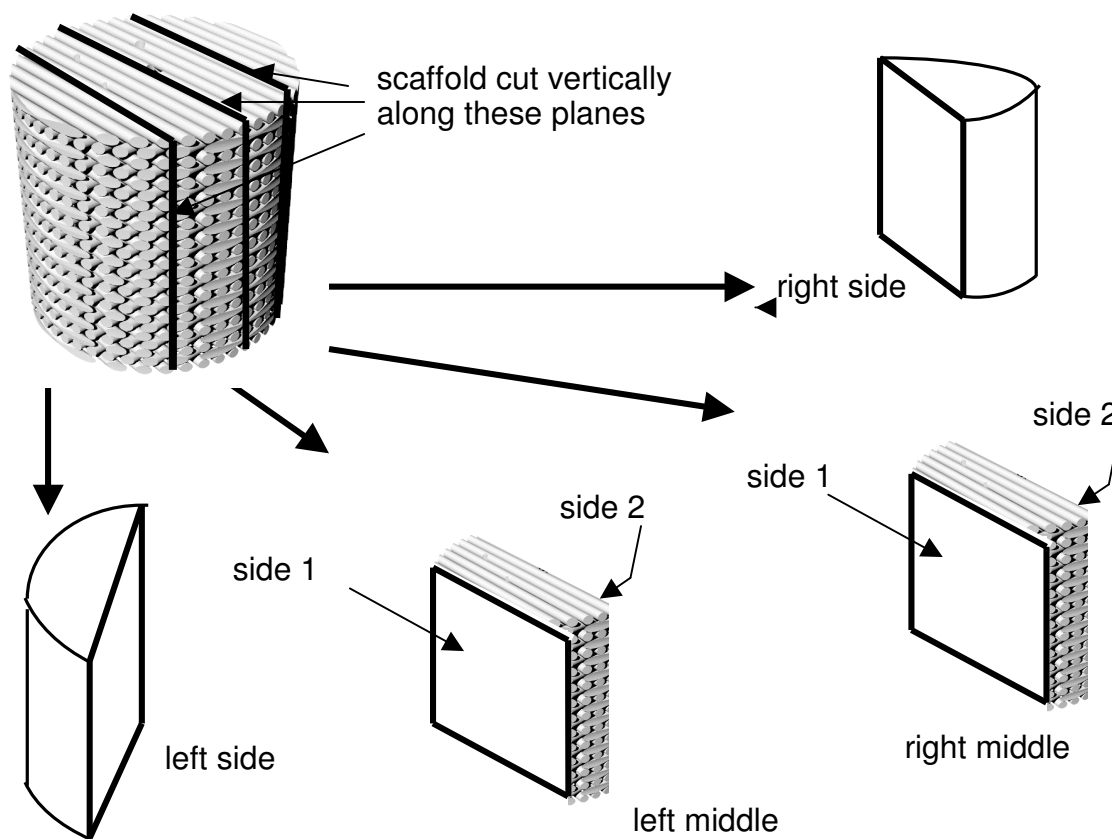


Figure 14. Schematic depicting sectioning of scaffold resulting in the generation of six surfaces for viewing under the fluorescence microscope

However, not every surface contained each of the possible 6 parts as the outer blades used for sectioning the scaffolds would continue to fan outwards as the box cutter cut deeper into a scaffold, resulting in the left and right side divisions quite often having very little of the bottom parts remaining. Also, the left and right middle divisions had one of their faces at a slope due to this uneven cutting and their orientation with respect to the camera had to be adjusted accordingly so as to get good resolution images. Drops of full media were gently added atop each division to prevent the cells from desiccating during imaging. The procedure was repeated on day 7. Six scaffolds, each of Type 3 and 4 ($n =$

3) were also subjected to the same procedure, with 3 of each type being evaluated on day 1 and the remaining 3 of each type on day 7 (Table 3).

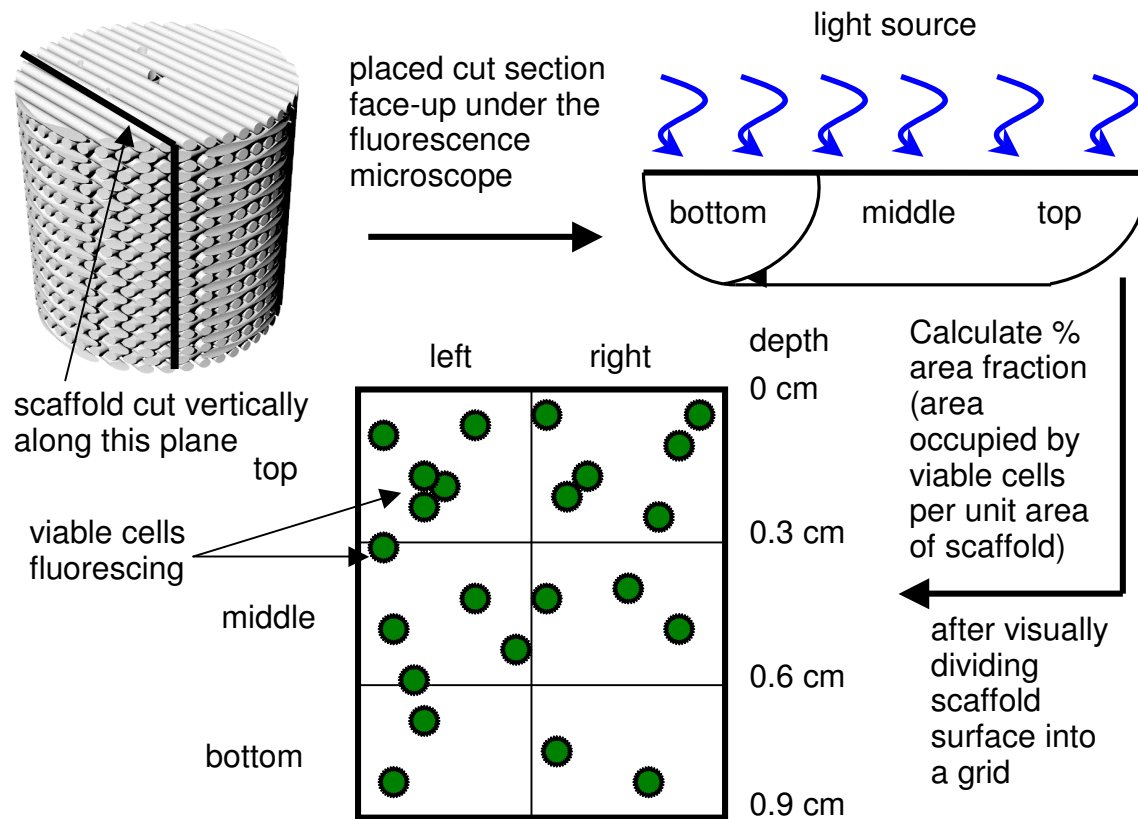
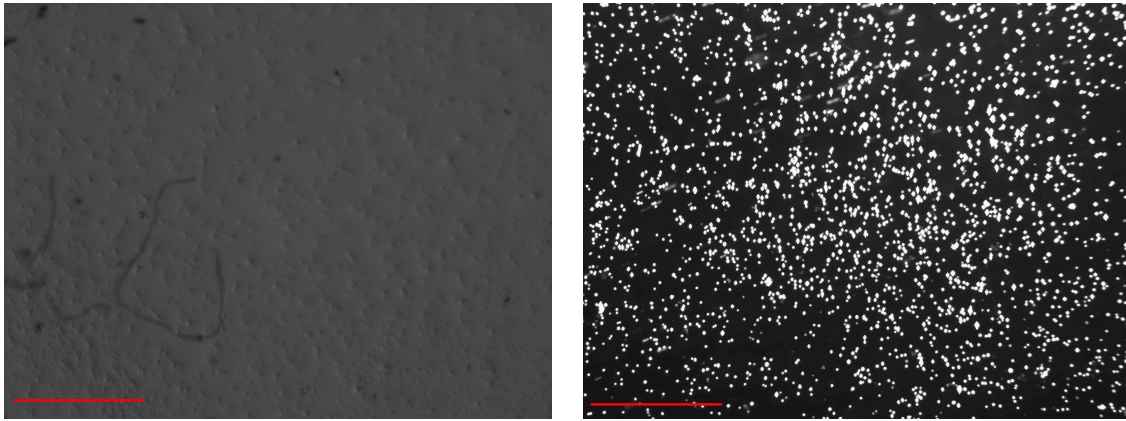


Figure 15. Schematic depicting fluorescence imaging of a scaffold surface after sectioning.

Table 3. Selection of constructs for cell viability measurement (n = 3).

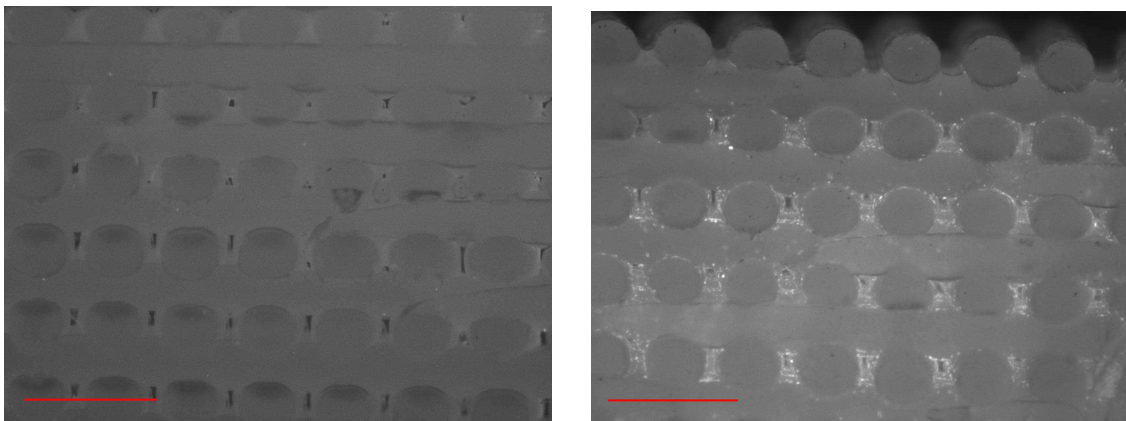
Set No.	Type of Scaffold Architecture	Constructs evaluated on Day 1	Constructs evaluated on Day 7
1	1	3	3
	2	3	3
2	3	3	3
	4	3	3

Image analysis was performed using the National Instruments Vision Assistant 8.0 software (National Instruments, Austin, TX). Image analysis entailed importing the 8 bit image (Figures 16 (d), 17 (d)), captured on the fluorescence microscope, into the software environment and using a series of software-generated functions for calculating percent area fraction. This series of steps involved subjecting the original image to a filter for highlighting the details of the fluorescing objects in the picture, followed by applying a 'square lookup table' in order to improve the contrast and brightness of the image. The resulting image was subjected to thresholding for the purpose of isolating the fluorescing cells from the background. A number of different thresholding functions were available out of which three were mainly employed depending on which one was most successful in detecting the cells. The three thresholding functions were manual threshold, a local background correction threshold and an auto entropy threshold. Out of these, the manual threshold was predominantly used. However, not all fluorescing material was cellular. There were contaminants that fluoresced and had to be discarded from the image before the area fraction could be calculated. For this purpose an image mask function, comprising shapes of different kinds that could mask user-defined areas, was employed to mask any non-cellular fluorescing contaminant. Since viable cells, cultured in media for the same time as those on the scaffolds, treated with calcein AM were imaged under the fluorescence microscope (Figures 16 (b), 17 (b)) at the same magnification as that being employed to capture the scaffold images, one could confidently isolate the contaminants based on size and intensity of fluorescence. After masking all the contaminants, a function calculating the percent area per unit image area was employed. This generated a value for each isolated, fluorescing entity. The values thus generated were summed up for that particular image to obtain its percent area fraction, which is



(a)

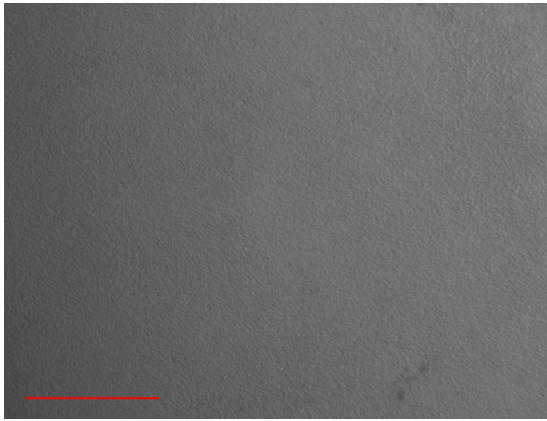
(b)



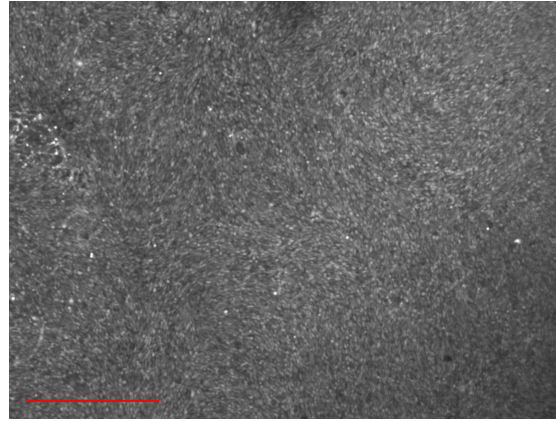
(c)

(d)

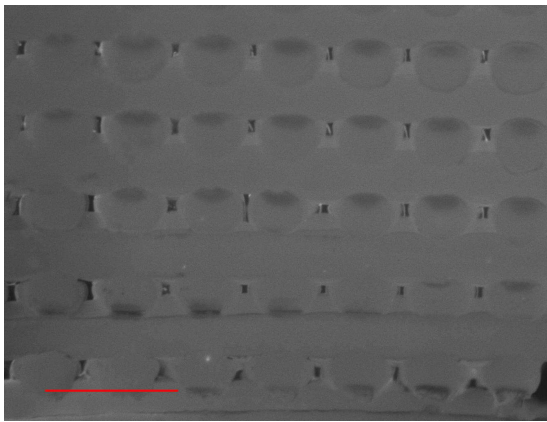
Figure 16. Images on day 1 of (a) MG63 cells seeded in a well, not treated with calcein AM (brightfield image), (b) MG63 cells treated with calcein AM (fluorescent image), (c) scaffold without cells treated with calcein AM (control) (fluorescent image), (d) scaffold with cells treated with calcein AM (sample) (fluorescent image). The red scale bar is 0.1 cm in length.



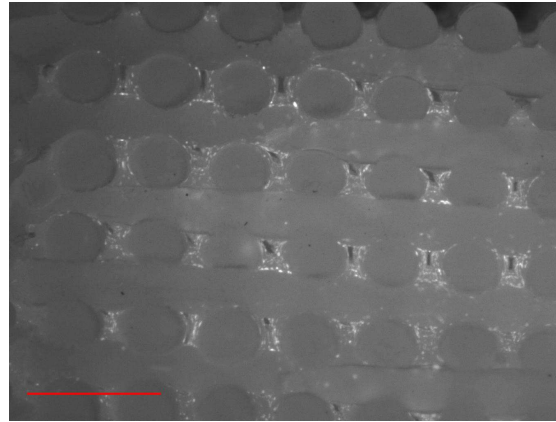
(a)



(b)



(c)



(d)

Figure 17. Images on day 7 of (a) MG63 cells not treated with calcein AM (brightfield image), (b) MG63 cells treated with calcein AM (fluorescent image), (c) scaffold without cells treated with calcein AM (control) (fluorescent image), (d) scaffold with cells treated with calcein AM (sample) (fluorescent image). The red scale bar is 0.1 cm in length.

indicative of the cell viability for the area subtended by the image. For the present study, cell viability was defined as the area occupied by live cells per unit area of the scaffold, expressed as a percentage.

The above procedure for image analysis was repeated for every construct part imaged. A mean value for the % area fraction for each region (top, middle and bottom) of a construct was obtained by averaging the % area fraction values for all parts lying in that region, for example, the top left and top right parts for all the 6 surfaces were averaged to get the mean % area fraction for the top region for that specific construct. To get the grand mean % area fraction for a specific Type of scaffold, for a particular region, on the day of interest, the values for the region of interest were averaged across the same Type ($n = 3$). A 3-way ANOVA was used to determine if significant differences existed between different regions on different days for the four different scaffold architectures at the 0.05 level of significance.

Chapter 10: Measurement of Cell Proliferation

Cell proliferation or DNA synthesis is typically quantified by detecting the incorporation of radioactive [³H]-thymidine into cellular DNA using autoradiography. However, since this assay is labor intensive, and uses expensive as well as potentially hazardous materials, 5-Bromo-2'-deoxy-uridine (BrdU) was the assay of choice. It too is incorporated in the DNA of actively dividing cells. Cells that have incorporated BrdU into their DNA can be quickly detected using a monoclonal antibody against BrdU and an enzyme- or fluorochrome-conjugated second antibody.

Cell proliferation was measured using the BrdU labeling and detection kit 1 (Roche Applied Science, Germany). The kit comprised BrdU labeling reagent, washing buffer concentrate (PBS), incubation buffer, Anti-BrdU (mouse monoclonal antibody) with nucleases and Anti-mouse Ig- fluorescein (from sheep). At the time point of interest, the cell-seeded scaffolds were removed from their surrounding ring and submerged in 10 μ M BrdU labeling medium before being placed in the incubator (5% CO₂, 37° C) for 45 minutes. The BrdU labeling medium was then aspirated and the constructs were washed thrice in the washing buffer solution. The constructs were then submerged in ethanol fixative for 30 minutes at -20° C and then washed thrice in washing buffer solution. Anti-BrdU working solution was then used to submerge the constructs, which were again incubated for 30 minutes. The constructs were again washed thrice with washing buffer solution before being submerged under Anti-mouse Ig-fluorescein working solution and incubated for 30 minutes. After washing the constructs thrice in washing buffer solution a final time, they were left submerged in the buffer solution and kept in a well plate covered by aluminum foil and stored in the refrigerator at 4° C for 30 minutes.

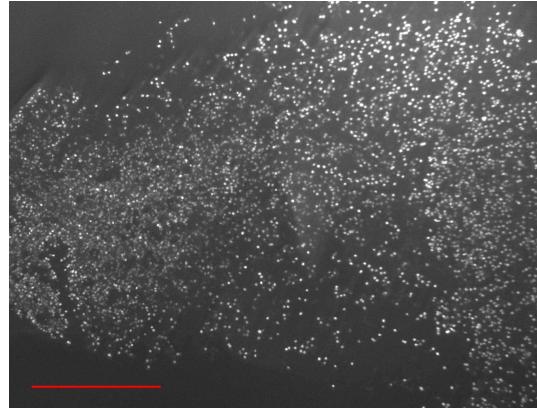
For viewing the cells that had incorporated the BrdU, the constructs were subjected to the same sectioning and fluorescence microscope imaging regimen as described for cell viability in Chapter 9. The excitation and emission spectra for Anti-mouse Ig-fluorescein, that binds to the Anti-BrdU which, in turn, binds to BrdU, matches that of calcein AM i.e. the former too has an excitation wavelength in the range of 450-500 nm and can be detected in the 515-565 nm (green) range. The collected images (Figures 18, 19) were also analyzed in the same way that the images for cell viability were analyzed, as described in Chapter 9. For the present study, cell proliferation was defined as the area occupied by proliferating cells per unit area of the scaffold, expressed as a percentage. Table 4 indicates the selection of constructs for performing the cell proliferation experiment. Since a total of 3 sets of experiments were performed with 1 sample in each set of each Type for each day, we have a sample size (n) of 3. A 3-way ANOVA was used to determine if significant differences existed between different regions on different days for the four different scaffold architectures at the 0.05 level of significance.

Table 4. Selection of constructs for cell proliferation measurement (n = 3).

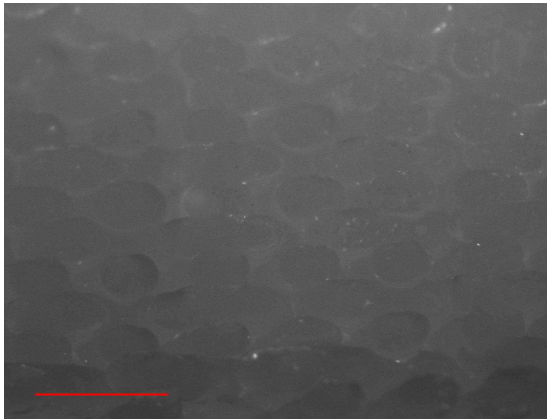
Set No.	Constructs evaluated on Day 1				Constructs evaluated on Day 7			
	Type of scaffold architecture				Type of scaffold architecture			
	1	2	3	4	1	2	3	4
1	1	1	1	1	1	1	1	1
2	1	1	1	1	1	1	1	1
3	1	1	1	1	1	1	1	1



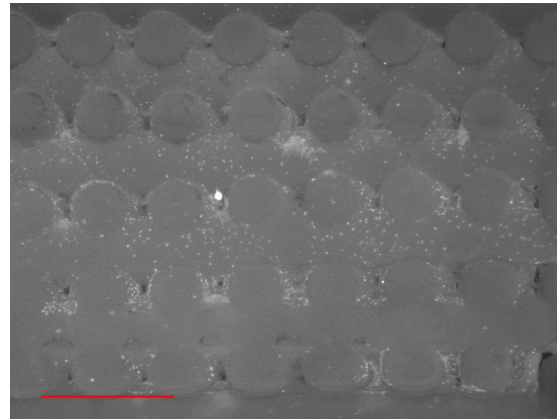
(a)



(b)

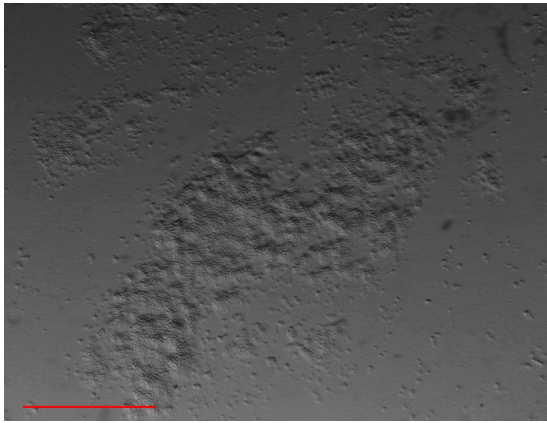


(c)

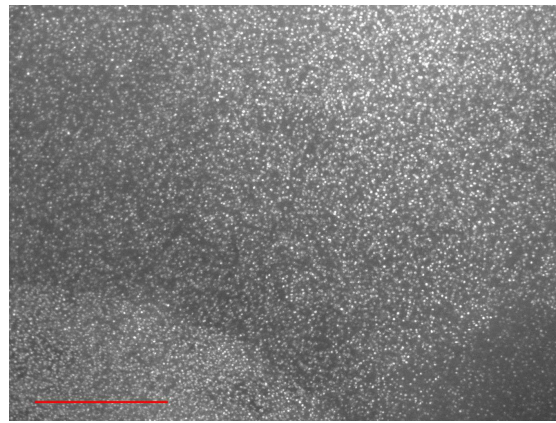


(d)

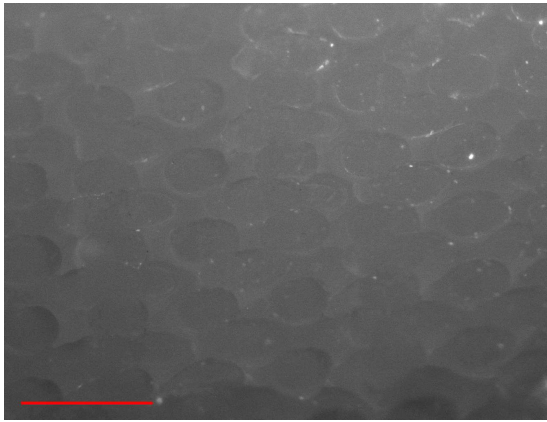
Figure 18. Images on day 1 of (a) MG63 cells not treated with BrdU kit (brightfield image), (b) MG63 cells treated with BrdU kit (fluorescent image), (c) scaffold without cells treated with BrdU kit (control) (fluorescent image), (d) scaffold with cells treated with BrdU kit (sample) (fluorescent image). The red scale bar is 0.1 cm in length.



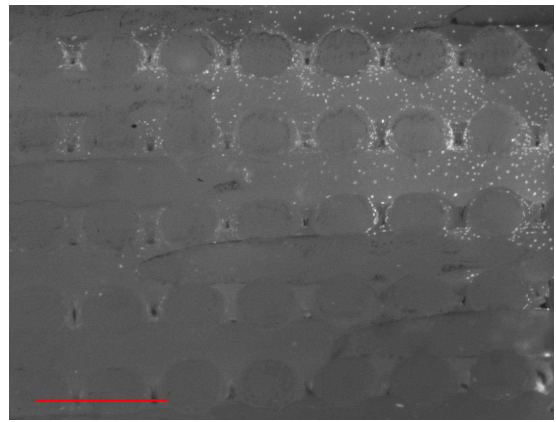
(a)



(b)



(c)



(d)

Figure 19. Images on day 7 of (a) MG63 cells not treated with BrdU kit (brightfield image), (b) MG63 cells treated with BrdU kit (fluorescent image), (c) scaffold without cells treated with BrdU kit (control) (fluorescent image), (d) scaffold with cells treated with BrdU kit (sample) (fluorescent image). The red scale bar is 0.1 cm in length.

Chapter 11: Mathematical Model for Diffusion of Oxygen

A simple mathematical model was developed to predict the oxygen concentration profiles within the architecturally distinct scaffolds seeded with cells. Since cells were seeded uniformly over the top surface of the scaffold, changes in oxygen concentration were expected only as a function of depth i.e. in the y direction (Figure 20). Thus, differentiation was not carried out with respect to radius ' r ' or angle ' θ ', as would normally be the case when dealing with cylindrical structures.

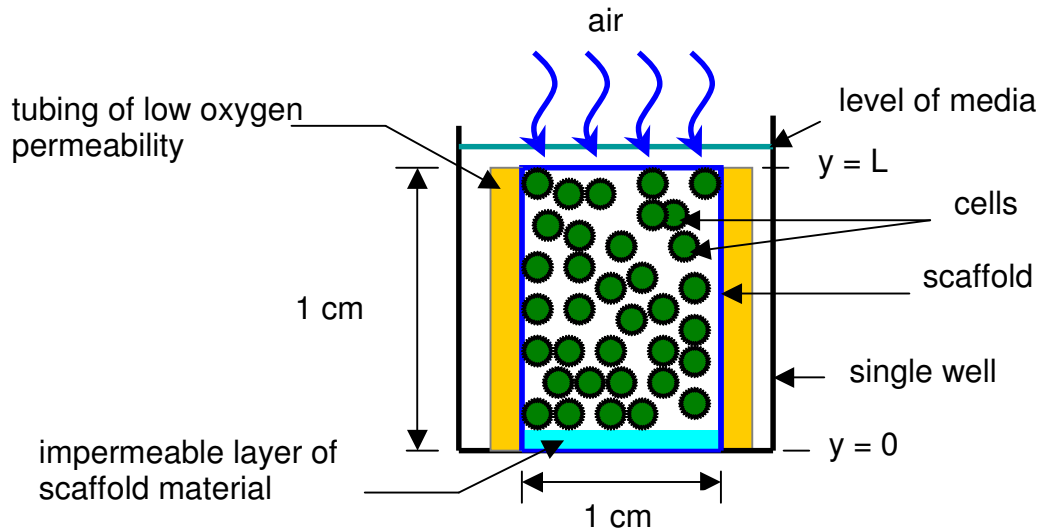


Figure 20. Schematic of air diffusing into cell-seeded scaffold

Assumptions of the model include uniform distribution of cells throughout the scaffold, uniform consumption of oxygen by cells throughout scaffold, constant diffusivity of oxygen in media, no diffusivity of oxygen through polymer, constant porosity and tortuosity of scaffold over duration of the experiment and no degradation of scaffold over duration of the experiment.

The mass balance for one-dimensional diffusion of oxygen from the top of a statically cell-seeded cylindrical scaffold sealed from all sides as well as the bottom, resting in a well is given by:

in = out + reaction+ accumulation

$$A \left(-D_{\text{eff}} \cdot \frac{\partial c' x_{\text{O}_2, \text{m}}}{\partial y} \cdot \Delta t \right) \Big|_y = A \left(-D_{\text{eff}} \cdot \frac{\partial c' x_{\text{O}_2, \text{m}}}{\partial y} \cdot \Delta t \right) \Big|_{y+\Delta y} + (-R_{\text{O}_2, \text{m}}) \cdot A \cdot \Delta y \cdot \Delta t + (A \cdot \Delta y \cdot c' \cdot x_{\text{O}_2, \text{m}}) \Big|_{t_2} - (A \cdot \Delta y \cdot c' \cdot x_{\text{O}_2, \text{m}}) \Big|_{t_1} \dots \dots \dots \text{(I)}$$

where,

$$t_2 = t_1 + \Delta t$$

A: Cross sectional area of scaffold

$D_{\text{eff}} = D \frac{\phi}{\tau}$: Effective diffusion of oxygen,

D : Diffusivity of oxygen in medium, ϕ : porosity; τ : tortuosity

units: m^2/sec

$c' = c \cdot \phi$: Total number of moles/lit of (medium+scaffold), since $c = \frac{\text{moles}}{\phi \cdot v}$, $c' = \frac{\text{moles}}{v}$

where 'v' is the volume of the scaffold

c: Total number of moles/lit of medium

$x_{\text{O}_2, \text{m}}$: mole fraction of oxygen in medium i.e $\frac{\text{moles of oxygen}}{\text{Total number of moles}}$

Δy : Distance across which oxygen diffuses

$-R_{\text{O}_2, \text{m}}$: Rate of consumption/disappearance of oxygen. units: moles/lit.sec

Canceling the 'A' terms we get:

$$D_{\text{eff}} \cdot \left[\left. -\frac{\partial c' x_{O_2,m}}{\partial y} \right|_y - \left. -\frac{\partial c' x_{O_2,m}}{\partial y} \right|_{y+\Delta y} \right] \cdot (\Delta t) = (-R_{O_2,m}) \cdot \Delta y \cdot (\Delta t) + \Delta y \cdot (c' x_{O_2,m} \Big|_{t_2} - c' x_{O_2,m} \Big|_{t_1})$$

Taking Δy on LHS and Δt on RHS we get

$$\left[\frac{D_{\text{eff}} \left(\frac{\partial c' x_{O_2,m}}{\partial y} \right) \Big|_{y+\Delta y} - D_{\text{eff}} \left(\frac{\partial c' x_{O_2,m}}{\partial y} \right) \Big|_y}{\Delta y} \right] = -R_{O_2,m} + \frac{(c' x_{O_2,m} \Big|_{t_2} - c' x_{O_2,m} \Big|_{t_1})}{\Delta t}$$

Setting the limits $\Delta y \rightarrow 0$ and $\Delta t \rightarrow 0$ we get

$$\frac{\partial}{\partial y} \left(D_{\text{eff}} \cdot \frac{\partial c' x_{O_2,m}}{\partial y} \right) = -R_{O_2,m} + \frac{\partial c' x_{O_2,m}}{\partial t}$$

Let $C_{O_2,m} = c' x_{O_2,m}$

And $-R_{O_2,m} = K \cdot C_{O_2,m}$ (units of K : /sec)

$$\frac{\partial C_{O_2,m}}{\partial t} - \frac{\partial}{\partial y} \left(D_{\text{eff}} \cdot \frac{\partial C_{O_2,m}}{\partial y} \right) = -K C_{O_2,m} \quad \dots\dots\dots\text{(II)}$$

Considering diffusivity to be constant:

$$\frac{\partial C_{O_2,m}}{\partial t} = D_{\text{eff}} \cdot \left(\frac{\partial^2 C_{O_2,m}}{\partial y^2} \right) - K C_{O_2,m} \quad \dots\dots\dots\text{(III)}$$

Boundary conditions:

$$1) C_{O_2,m} \Big|_{y=L} = C_{O_2,s}$$

where, $C_{O_2,s}$ = concentration of oxygen in solution

$$2) \left. \frac{\partial C_{O_2,m}}{\partial y} \right|_{y=0} = 0$$

$$\text{Initial Condition: } C_{O_2,m} \Big|_{0 < y < L} = C_{O_2,s}$$

In order to solve this differential equation we will need to non-dimensionalize the equation by defining the following:

$$\psi = \frac{C_{O_2,m}}{C_{O_2,s}} ; \xi = \frac{y}{L} ; \tau = \frac{D_{\text{eff}} \cdot t}{L^2} ; \phi^2 = \frac{k \cdot L^2}{D_{\text{eff}}}$$

Hence,

$$\partial \psi = \frac{\partial C_{O_2,m}}{C_{O_2,s}} ; \partial \xi^2 = \frac{\partial y^2}{L^2} ; \partial \tau = \frac{\partial D_{\text{eff}} \cdot t}{L^2} ; \phi^2 = \frac{k \cdot L^2}{D_{\text{eff}}}$$

We can now attempt to represent (III) in terms of the non-dimensionalized terms:

$$\frac{\frac{\partial C_{O_2,m}}{C_{O_2,s}}}{\frac{\partial D_{\text{eff}} \cdot t}{L^2}} = \frac{\frac{\partial^2 C_{O_2,m}}{C_{O_2,s}}}{\frac{\partial y^2}{L^2}} - \frac{k \cdot L^2}{D_{\text{eff}}} \cdot \frac{C_{O_2,m}}{C_{O_2,s}} \quad (\text{terms in bold cancel})$$

Thus, (III) gets modified to:

$$\frac{\partial \psi}{\partial \tau} = \frac{\partial^2 \psi}{\partial \xi^2} - \phi^2 \psi \quad \dots\dots\dots(1)$$

with Boundary Conditions (BCs):

$$1) \tau > 0 \quad \xi = 1 \quad \psi = 1 \dots \dots \dots (A)$$

$$2) \tau > 0 \quad \xi = 0 \quad \frac{\partial \psi}{\partial \xi} = 0 \dots \dots \dots (B)$$

and Initial Condition:

$$1) \tau = 0 \quad 0 < \xi < 1 \quad \psi = 1 \dots \dots \dots (C)$$

The solution can be written in the form:

$$\psi(\xi, \tau) = V(\xi, \tau) + W(\xi) \dots \dots \dots (D)$$

	Transient	Steady state	
$\frac{\partial \psi}{\partial \xi} = \frac{\partial V}{\partial \xi} + \frac{\partial W}{\partial \xi}$			\dots \dots \dots (2)

$\frac{\partial \psi}{\partial \tau} = \frac{\partial V}{\partial \tau}$			\dots \dots \dots (3)
--	--	--	-----------------------

$\frac{\partial^2 \psi}{\partial \xi^2} = \frac{\partial^2 V}{\partial \xi^2} + \frac{\partial^2 W}{\partial \xi^2}$			\dots \dots \dots (4)
--	--	--	-----------------------

Substituting (3) and (4) in (1) we get

$$\frac{\partial V}{\partial \tau} = \frac{\partial^2 V}{\partial \xi^2} + \frac{\partial^2 W}{\partial \xi^2} - \phi^2 \psi$$

$$\frac{\partial V}{\partial \tau} = \frac{\partial^2 V}{\partial \xi^2} + \frac{\partial^2 W}{\partial \xi^2} - \phi^2 (V + W) \dots \dots \dots (5)$$

At steady state

i.e. as $\tau \rightarrow \infty$, $V = 0$, hence, $\psi = V + W = W$

Thus, $\frac{\partial^2 W}{\partial \xi^2} - \phi^2 W = 0$

i.e. $\frac{\partial^2 W}{\partial \xi^2} = \phi^2 W$

The general solution for this is, $W = A.e^{\phi \xi} + B.e^{-\phi \xi}$

Using BC#1 condition 1: at $\xi = +1$, $W = 1$. Thus, $1 = A.e^{\phi} + B.e^{-\phi}$ (6)

Using BC#2: at $\xi = 0$, $\frac{\partial W}{\partial \xi} = 0$. Thus, $0 = A\phi e^0 - B\phi e^0$ i.e. $A = B$ (8)

From (6) and (8),

$$A = \frac{1}{e^{-\phi} + e^{\phi}} \text{ (Since, from (8), } A = B)$$

$$\text{Thus, } A = \frac{1}{2 \cosh \phi}$$

$$\text{Now, } W = A.e^{\phi \xi} + B.e^{-\phi \xi} = \frac{1}{2 \cosh \phi} \cdot 2 \cosh \phi \xi = \frac{\cosh \phi \xi}{\cosh \phi} \text{(9)}$$

This is the solution for steady state.

For the **transient part**, let $V(\xi, \tau) = e^{-\phi^2 \tau} \cdot U(\xi, \tau)$(10)

$$\text{Then, } \psi = e^{-\phi^2 \tau} \cdot U(\xi, \tau) + W(\xi)$$

$$\frac{\partial V}{\partial \tau} = e^{-\phi^2 \tau} \cdot \frac{\partial U}{\partial \tau} - \phi^2 \cdot e^{-\phi^2 \tau} \cdot U$$

$$\frac{\partial^2 V}{\partial \xi^2} = e^{-\phi^2 \tau} \cdot \frac{\partial^2 U}{\partial \xi^2}$$

Substituting the above in (5) we get:

$$e^{-\phi^2 \tau} \cdot \frac{\partial U}{\partial \tau} - \phi^2 \cdot e^{-\phi^2 \tau} \cdot U = e^{-\phi^2 \tau} \cdot \frac{\partial^2 U}{\partial \xi^2} + \frac{\partial^2 W}{\partial \xi^2} - \phi^2 (V + W)$$

Using (10):

$$e^{-\phi^2 \tau} \left[\frac{\partial U}{\partial \tau} - \phi^2 \cdot U \right] = e^{-\phi^2 \tau} \cdot \frac{\partial^2 U}{\partial \xi^2} + \frac{\partial^2 W}{\partial \xi^2} - \phi^2 \cdot e^{-\phi^2 \tau} \cdot U(\xi, \tau) - \phi^2 \cdot W$$

$$e^{-\phi^2 \tau} \left[\frac{\partial U}{\partial \tau} - \phi^2 \cdot U - \frac{\partial^2 U}{\partial \xi^2} + \phi^2 U \right] = \frac{\partial^2 W}{\partial \xi^2} - \phi^2 \cdot W$$

We recognize that the RHS of the above equation is 0, since W is the steady state solution for the differential equation.

$$\frac{\partial U}{\partial \tau} = \frac{\partial^2 U}{\partial \xi^2}$$

We now solve the equation using the well known method of separation of variables:

Let $U = F(\xi).G(\tau)$

$$\frac{\partial U}{\partial \tau} = F \frac{\partial G}{\partial \tau}$$

$$\frac{\partial^2 U}{\partial \xi^2} = G \frac{\partial^2 F}{\partial \xi^2}$$

Thus,

$$F \frac{\partial G}{\partial \tau} = G \frac{\partial^2 F}{\partial \xi^2}$$

$$\text{Let, } \frac{1}{G} \frac{\partial G}{\partial \tau} = \frac{1}{F} \frac{\partial^2 F}{\partial \xi^2} = K = -p^2$$

Then,

$$F'' + p^2 F = 0 \dots \dots \dots (11)$$

The general solution for (11) is: $F(\xi) = A \cos(p\xi) + B \sin(p\xi)$

And

$$\frac{\partial G}{\partial \tau} + p^2 G = 0 \dots \dots \dots (12)$$

The general solution for (12) is: $\frac{\partial G}{\partial \tau} = -p^2 G$

$$\int \frac{\partial G}{G} = \int -p^2 \partial \tau$$

$$\ln G = -p^2 \tau + c$$

$$\ln \left(\frac{G}{G_0} \right) = -p^2 \tau$$

$$G = G_0 e^{-p^2 \tau}$$

Now, from Boundary Condition 2 i.e. (B)

$$\text{When } \xi = 0, \frac{\partial \psi}{\partial \xi} = 0$$

$$\text{i.e. } \frac{\partial \psi}{\partial \xi} = \frac{\partial V}{\partial \xi} + \frac{\partial W}{\partial \xi} = 0$$

$$\text{i.e. } e^{-\phi^2 \tau} \cdot \frac{\partial U}{\partial \xi} + \frac{\partial W}{\partial \xi} = 0$$

$$\text{i.e. } e^{-\phi^2 \tau} \frac{\partial}{\partial \xi} \left[(A \cos p\xi + B \sin p\xi) \cdot G_0 e^{-p^2 \tau} \right] + \frac{\partial}{\partial \xi} \left[\frac{e^{\phi\xi} + e^{-\phi\xi}}{e^{-\phi} + e^{\phi}} \right]$$

$$e^{-\phi^2 \tau} \left[\frac{\partial}{\partial \xi} A \cos p\xi \cdot G_0 e^{-p^2 \tau} + \frac{\partial}{\partial \xi} B \sin p\xi \cdot G_0 e^{-p^2 \tau} \right] + \frac{\partial}{\partial \xi} \left[\frac{e^{\phi\xi} + e^{-\phi\xi}}{e^{-\phi} + e^{\phi}} \right]$$

$$e^{-\phi^2 \tau} \cdot A \cdot p(-\sin p\xi) \cdot G_0 e^{-p^2 \tau} + e^{-\phi^2 \tau} \cdot B \cdot p \cdot \cos p\xi \cdot G_0 e^{-p^2 \tau} + \frac{\phi e^{\phi\xi} - \phi e^{-\phi\xi}}{e^{-\phi} + e^{\phi}}$$

Substituting $\xi = 0$ in the above equation we get

$$0 + e^{-\phi^2 \tau} \cdot B \cdot p \cdot \cos p\xi \cdot G_0 e^{-p^2 \tau} + 0 = 0$$

But, since $e^{-\phi^2 \tau}, G_0, e^{-p^2 \tau}$ are constants they cannot be 0

Thus, $B \cdot p = 0$

But p cannot be 0, thus $B = 0$.

Now, from (A) and (D) when $\xi = 1, V + W = 1$

i.e. $e^{-\phi^2\tau} \cdot U(\xi, \tau) + W = 1$

i.e. $e^{-\phi^2\tau} \cdot F(\xi) \cdot G(\tau) + W = 1$

but, for $\xi = 1, W = 1$ from (6)

Thus, $F \cdot G = 0$

But, since $G \neq 0, F = 0$ (Since G_0 is a constant and can't be 0 and neither can $e^{-p^2\tau}$)

i.e. $A \cos(p\xi) + B \sin(p\xi) = 0$

For $\xi = 1, A \cos(p) + B \sin(p) = 0$

Thus, $A \cos(p) = 0$ (since $B = 0$)

Thus, $p = \frac{(2n+1)\Pi}{2}, A = 1, \text{ For } n = 0, 1, 2, 3, \dots$

Now, $U = F \cdot G$

i.e. $U = [A \cos(p\xi) + B \sin(p\xi)] \cdot [G_0 e^{-p^2\tau}]$

$$U = \sum_{n=0}^{\infty} A \cos\left[\frac{(2n+1)\Pi\xi}{2}\right] G_0 \exp\left[-\frac{(2n+1)^2 \Pi^2 \tau}{4}\right]$$

From (10),

$V(\xi, \tau) = e^{-\phi^2\tau} \cdot U(\xi, \tau)$

i.e. $V(\xi, \tau) = e^{-\phi^2\tau} \cdot \sum_{n=0}^{\infty} A \cos\left[\frac{(2n+1)\Pi\xi}{2}\right] G_0 \exp\left[-\frac{(2n+1)^2 \Pi^2 \tau}{4}\right]$

From (D),

$\psi(\xi, \tau) = V(\xi, \tau) + W(\xi)$

$$\psi = e^{-\phi^2\tau} \cdot \sum_{n=0}^{\infty} A \cos\left[\frac{(2n+1)\Pi\xi}{2}\right] G_0 \exp\left[-\frac{(2n+1)^2 \Pi^2 \tau}{4}\right] + \frac{\cosh \phi\xi}{\cosh \phi} \dots\dots(13)$$

From (C):

At $\tau = 0, e^{-\phi^2\tau} \cdot U(\xi, \tau) + W = 1$

i.e. $U + W = 1$

$$\sum_{n=0}^{\infty} A \cos\left[\frac{(2n+1)\Pi\xi}{2}\right] G_o \exp\left[-\frac{(2n+1)^2 \Pi^2 \tau}{4}\right] + \frac{\cosh \phi \xi}{\cosh \phi} = 1$$

$$\sum_{n=0}^{\infty} A \cos\left[\frac{(2n+1)\Pi\xi}{2}\right] G_o(1) + \frac{\cosh \phi \xi}{\cosh \phi} = 1$$

$$\text{Thus, } G_o = \left[1 - \frac{\cosh \phi \xi}{\cosh \phi}\right] \frac{1}{\sum_{n=0}^{\infty} \cos\left[\frac{(2n+1)\Pi\xi}{2}\right]} \quad (\text{since } A = 1)$$

Substituting for G_o in (13) we get,

$$\psi = e^{-\phi^2 \tau} \cdot \sum_{n=0}^{\infty} A \cos\left[\frac{(2n+1)\Pi\xi}{2}\right] \left[1 - \frac{\cosh \phi \xi}{\cosh \phi}\right] \frac{1}{\sum_{n=0}^{\infty} \cos\left[\frac{(2n+1)\Pi\xi}{2}\right]} \exp\left[-\frac{(2n+1)^2 \Pi^2 \tau}{4}\right] + \frac{\cosh \phi \xi}{\cosh \phi}$$

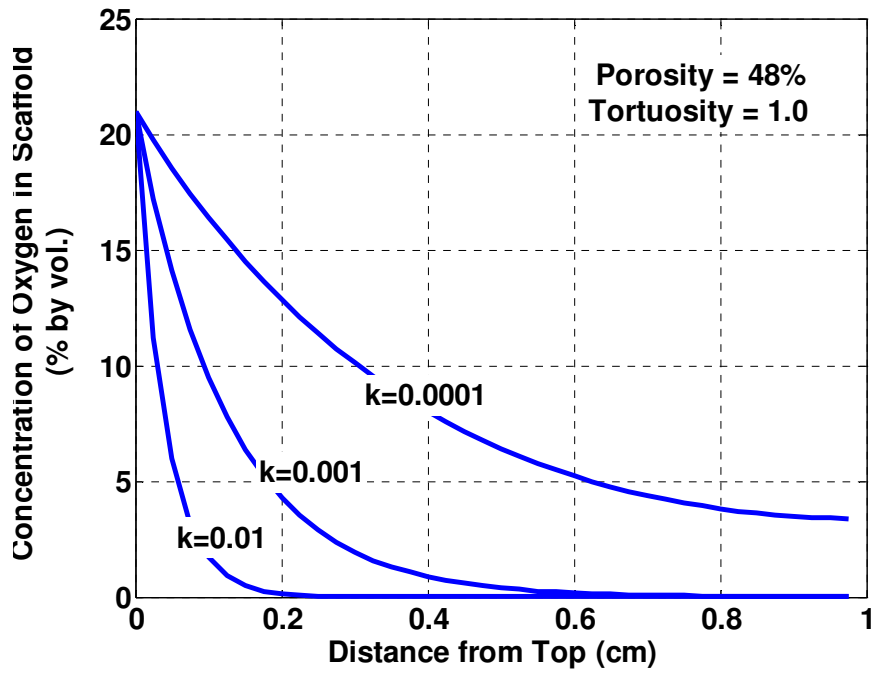
On resubstituting the dimensionalized quantities in the above equation, we get:

$$C_{O_2,m} = C_{O_2,s} \left[\frac{\cosh y \sqrt{\frac{K}{D_{eff}}}}{\cosh L \sqrt{\frac{K}{D_{eff}}}} + e^{-Kt} \sum_{n=0}^{\infty} \left(1 - \frac{\cosh y \sqrt{\frac{K}{D_{eff}}}}{\cosh L \sqrt{\frac{K}{D_{eff}}}} \right) \cdot \frac{H}{\sum_{n=0}^{\infty} \frac{\cos(2n+1)\Pi y}{2L}} \right]$$

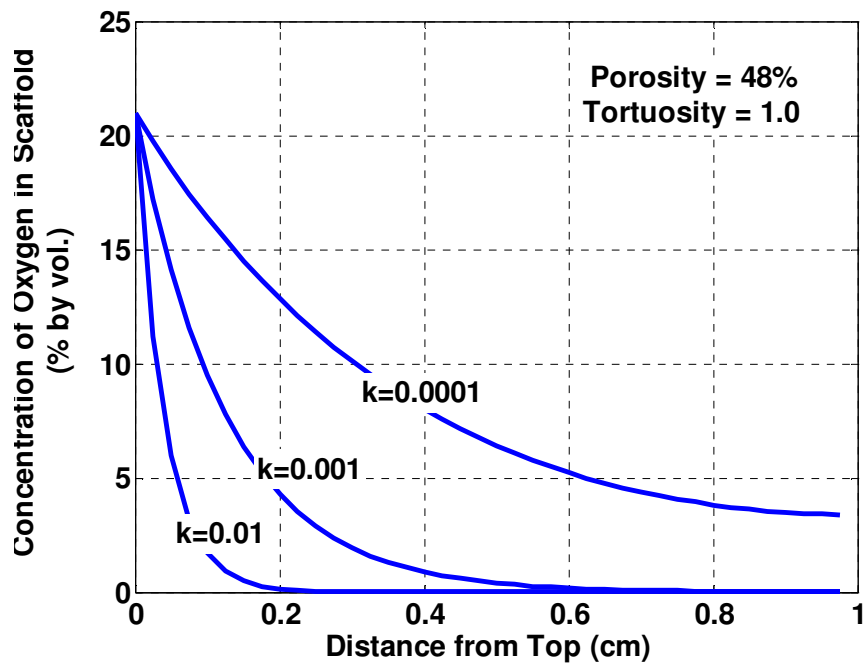
where,

$$H = \frac{\cos(2n+1)\Pi y}{2L} \exp\left(\frac{-(2n+1)^2 \cdot \Pi^2 \cdot D \cdot t}{4 \cdot L^2}\right)$$

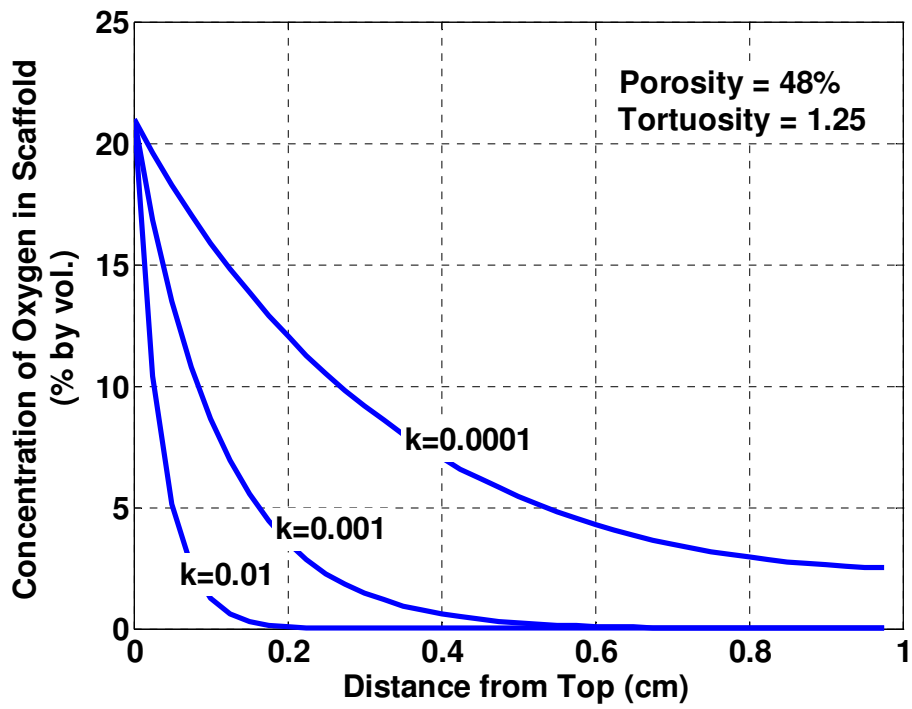
This is the analytical solution to the mass balance equation. This equation was coded in Matlab® Version 5.3 (Mathworks, Natick, MA) to generate profiles for different values of K , the rate constant that accounts for cell distribution and oxygen consumption.



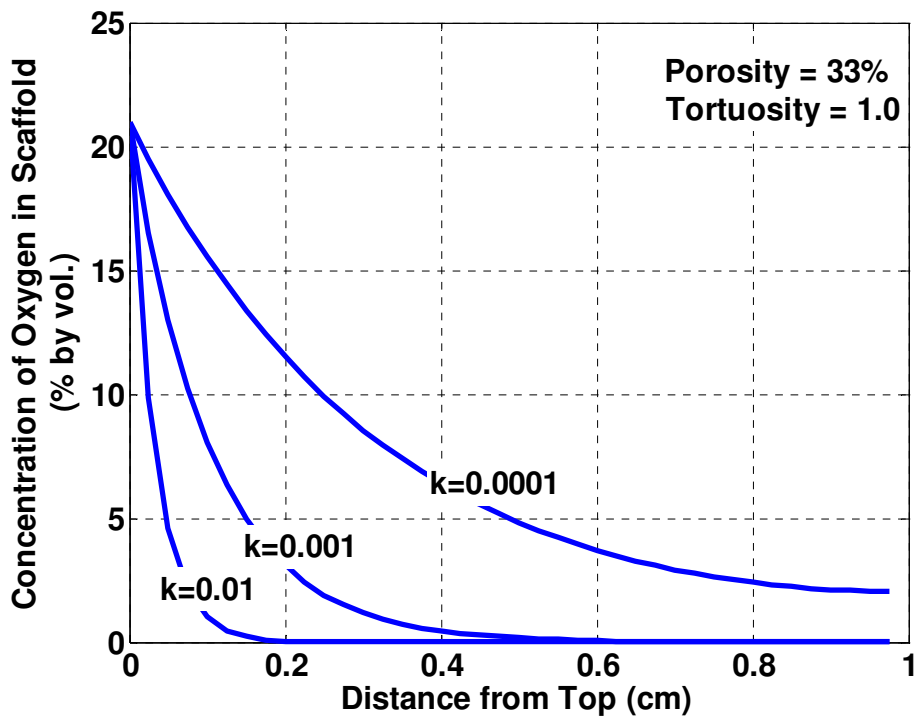
(a)



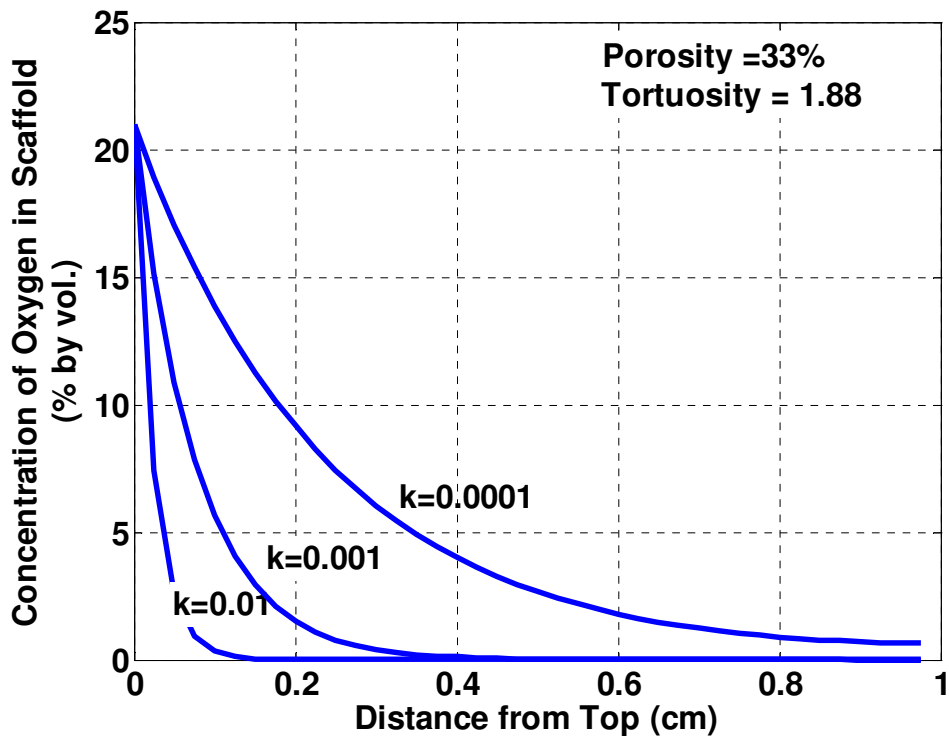
(b)



(c)



(d)



(e)

Figure 21. Matlab-generated oxygen concentration profiles for different magnitudes of the rate constant for (a) Type 1 on day 1, (b) Type 1 on Day 7, (c) Type 2 on day 7, (d) Type 3 on day 7 and (e) Type 4 on day 7.

Figure 16 shows oxygen concentration profiles of the different scaffold architectures. On comparing Figures 21 (a) and (b) we see that they are identical, indicating that the model predicts that a steady state will be reached by day 1 for Type 1. This prediction holds for all four types. As we go from Type 1 (Figure 21 (b)) to Type 2 (Figure 21 (c)) to Type 3 (Figure 21 (d)) to Type 4 (Figure 21 (e)) we see that the profiles for different values of k continue to become steeper indicating the effect that porosity and tortuosity have on diffusion of oxygen within the scaffold. The model was validated by

carrying out oxygen concentration measurements on cell-seeded scaffolds of the four types.

The above model was developed to represent a one-dimensional case of oxygen diffusing into the construct from the top. The scaffold was sealed from the bottom so as to be able to study the effect of one-dimensional diffusion over a longer length scale and to validate this prediction by experimental measurements. However, taking a more practical view, one would like to see the effect of three-dimensional diffusion of oxygen as this would most closely mimic the case of a construct being placed *in vivo*. This proves to be very challenging not only from a modeling point of view but from an experimental point of view as well.

From the point of view of modeling, every additional dimension adds to exponentially increasing complexity in the equations because of the non-linear, differential nature of the terms involved. For example, if the above cylindrical model was to be studied as a three-dimensional case of oxygen diffusion, one would have to include changes in $x_{O_2,m}$ with respect to radius 'r' and angle 'θ' in addition to depth 'y' in the mass balance equation we began with, which is normally the case when dealing with cylindrical structures. This would make the equation extremely difficult to solve analytically and then one has to resort to numerical techniques to solve such problems.⁶⁵ That is why a majority of the models that are solved analytically make simplifying assumptions.

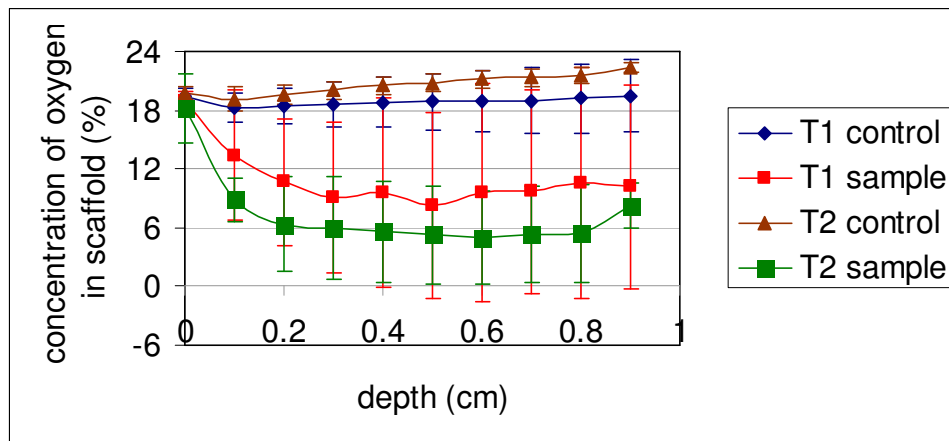
From an experimental point of view, it is expensive to have a perfusion or rotating bioreactor that can ensure uniform cell seeding in three dimensions. Even if one was successful in obtaining uniform cell distribution using a bioreactor, carrying out oxygen concentration measurements along the three dimensions (r, θ, y) would pose a big challenge, especially if one is interested in studying the effects of scaffold architecture.

This is because to obtain measurements to validate the model one would require to make holes within the construct if using a microelectrode system and the more the holes drilled along different dimensions, the more will the integrity of the scaffold be compromised thereby further diluting the effects of scaffold architecture. So far it has been extremely difficult to obtain more than a two dimensional map of oxygen distribution, which requires the surface for which the distribution needs to be obtained, to be in contact with an oxygen-sensitive foil (discussed in Chapter 4). The principle of phosphorescence quenching is used in order to generate the oxygen concentration profile in two dimensions.⁴⁶ This technique would, understandably, have limited use in measuring oxygen concentration in the interior of three-dimensional constructs.

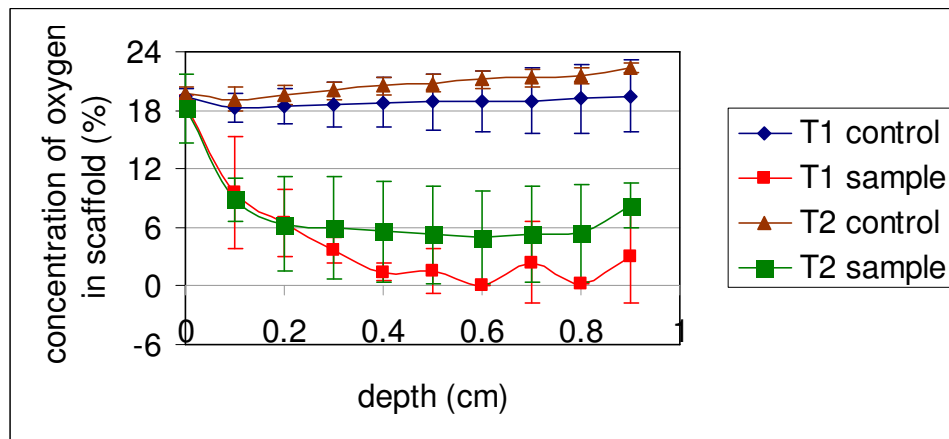
RESULTS

Chapter 12: Oxygen Concentration Measurement Results

The mean (\pm SD) profiles ($n = 3$) for oxygen concentration measurements of controls and samples of different architectures are plotted in Figures 22-25. The figures are plotted in pairs with both depicting the mean (\pm SD), the difference being that the first



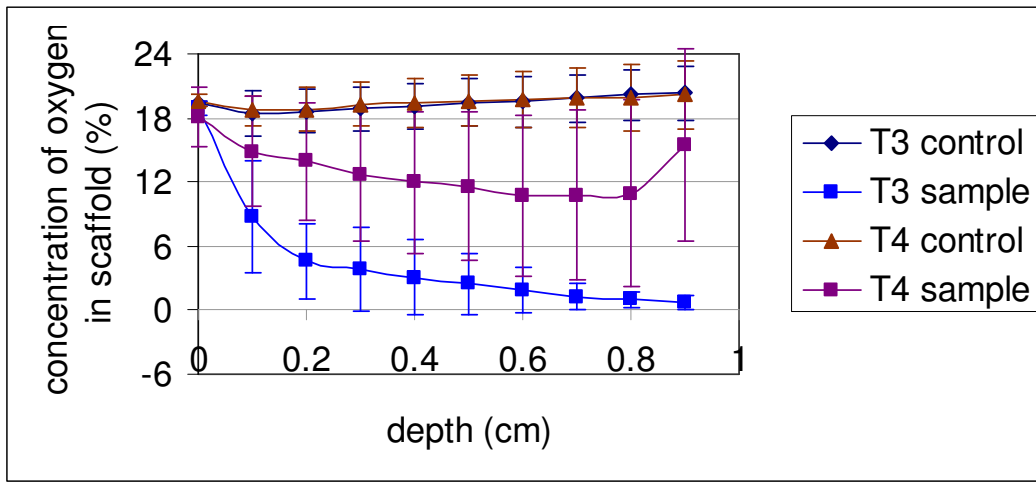
(a)



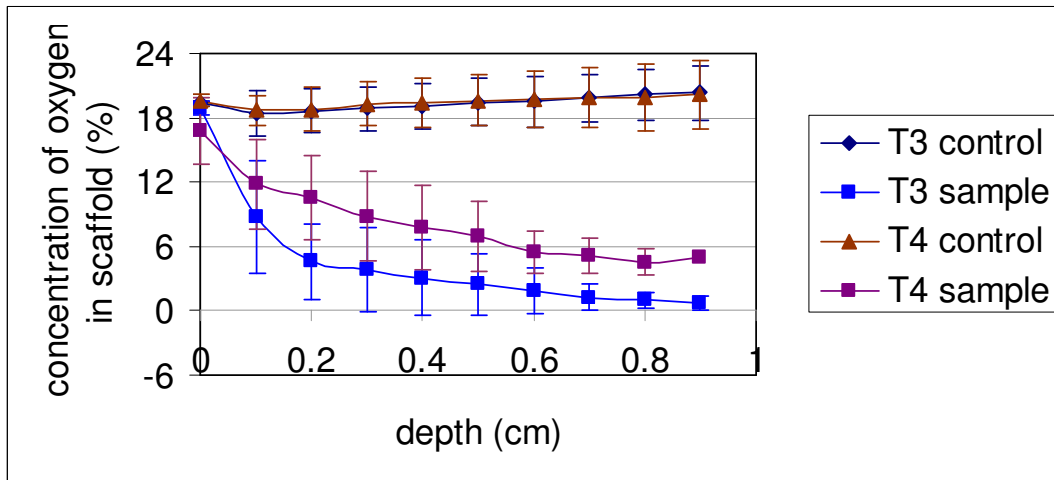
(b)

Figure 22. Mean (\pm SD) oxygen concentration profiles for controls and samples of architecture Type 1 and 2 on day 1 for (a) $n = 3$, (b) ignoring T1 sample from Set 2.

one in each pair reflects all the data for a particular Type and day ($n = 3$) while some of the data have been eliminated for generating the second one in the pair. The data for Type 1 on day 1 belonging to set 2 (Figure 22 (b)) and for Type 4 on day 1 belonging to set 2 (Figure 23 (b)) were eliminated because their oxygen concentration profiles were similar to their respective controls (Figure 26) and this was causing the over all data to have large



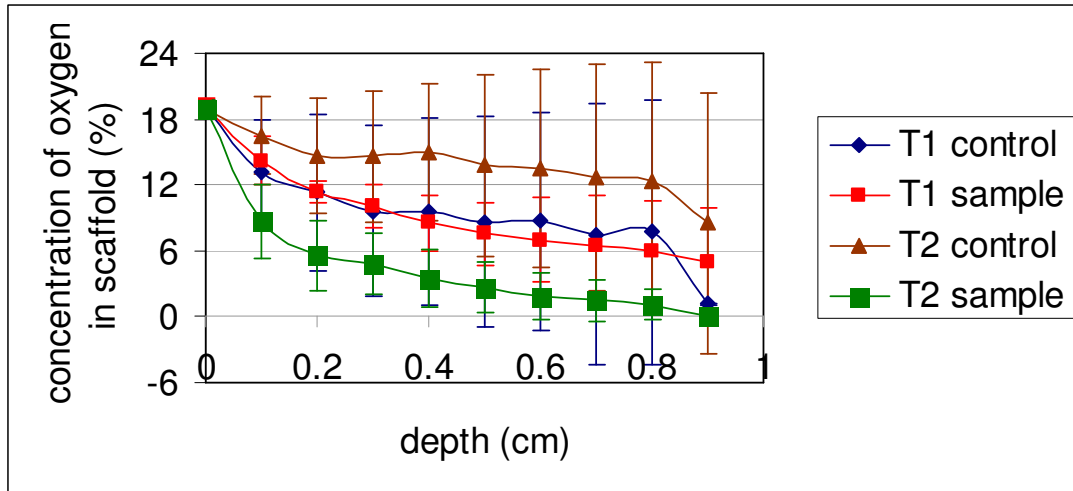
(a)



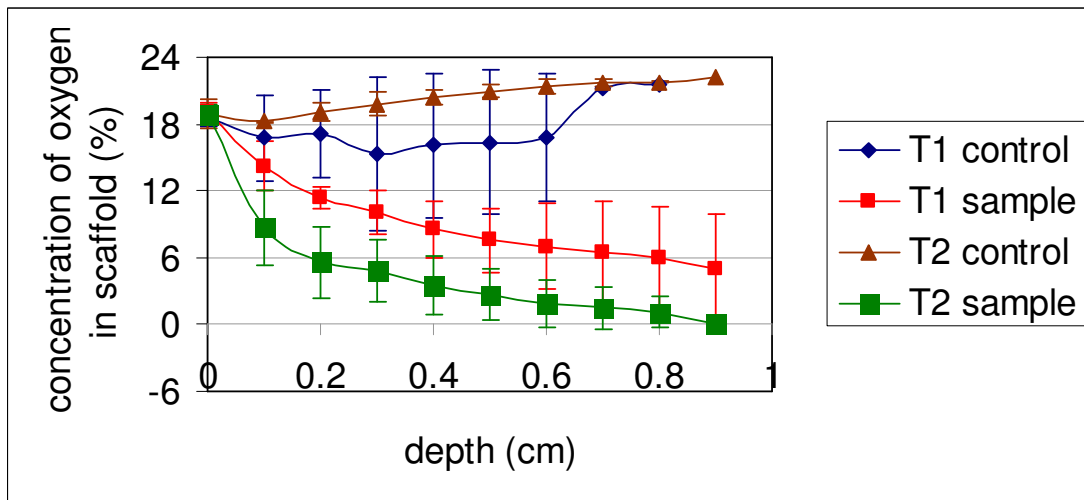
(b)

Figure 23. Mean (\pm SD) oxygen concentration profiles for controls and samples of architecture Type 3 and 4 on day 1 for (a) $n = 3$, (b) ignoring T4 sample from Set 2.

standard deviations. In order to further explore this discrepancy, the above samples and controls were subjected to cell viability analysis (Figures 27, 28). From Figure 27 (c) we see that the cell viability as reflected by the mean % area fraction values for the top, middle and bottom regions for Type 1 are not only low but very similar. This could be



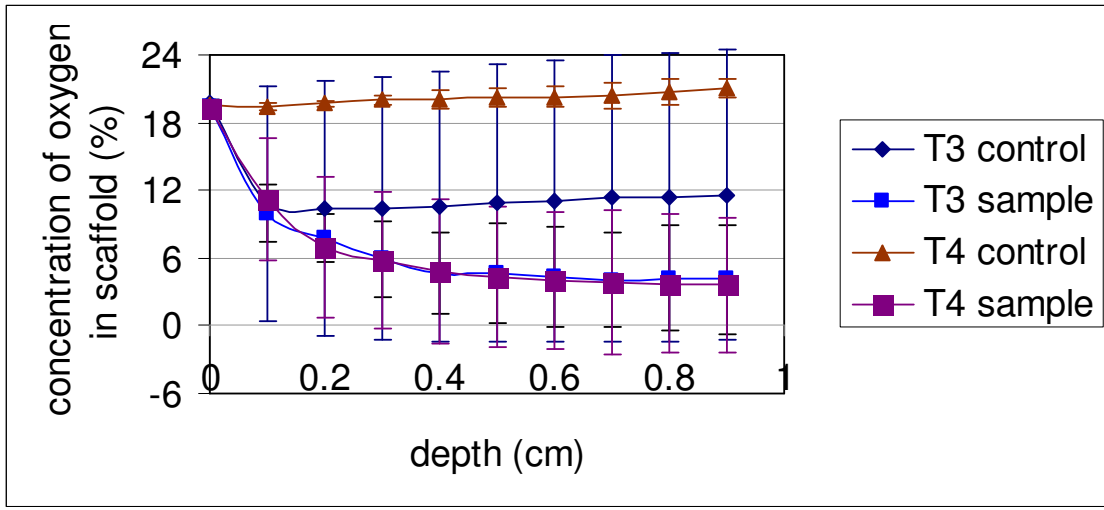
(a)



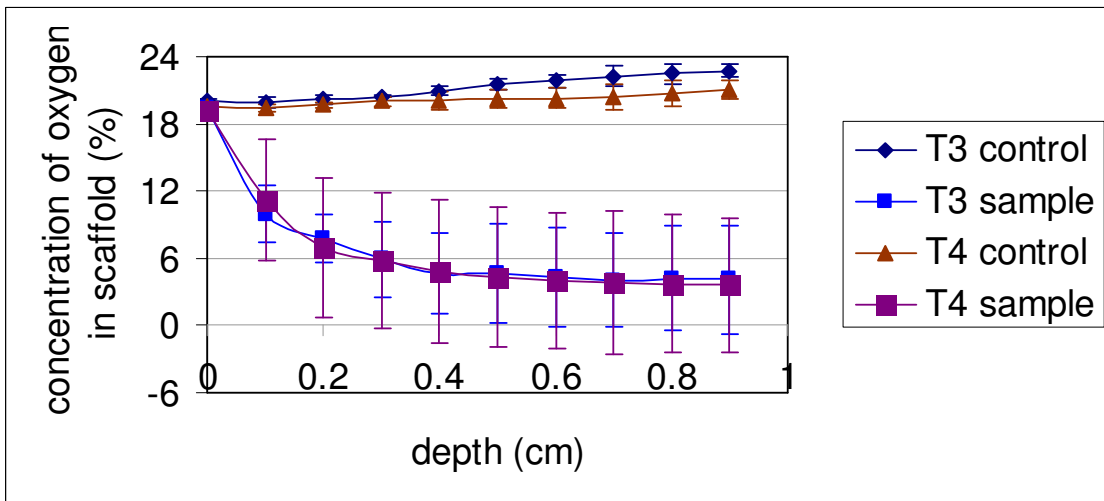
(b)

Figure 24. Mean (\pm SD) oxygen concentration profiles for controls and samples of architecture Type 1 and 2 on day 7 for (a) $n = 3$, (b) ignoring T1 control and T2 control from Set 1.

indicative of the presence of very few viable cells in the construct because of which there is no consumption of oxygen taking place causing its level to remain relatively flat like the control. This is even more pronounced in the case of Type 4 (Figure 28 (c)) where we find hardly any viable cells in the top region and none at all in the middle and bottom,



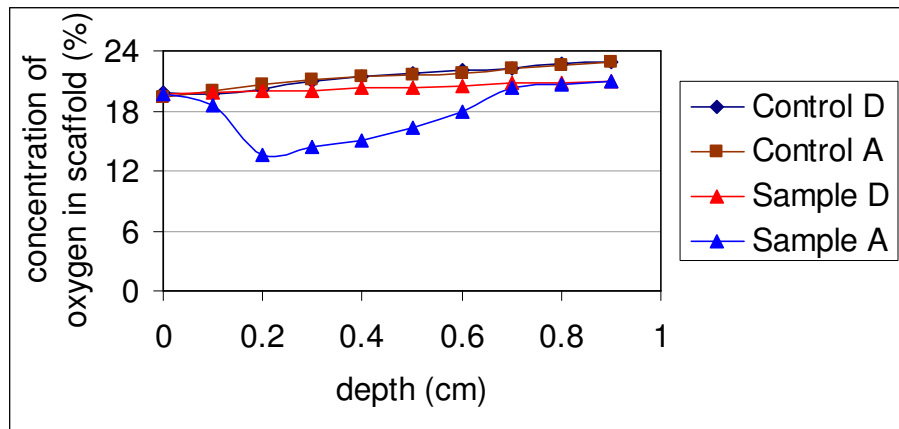
(a)



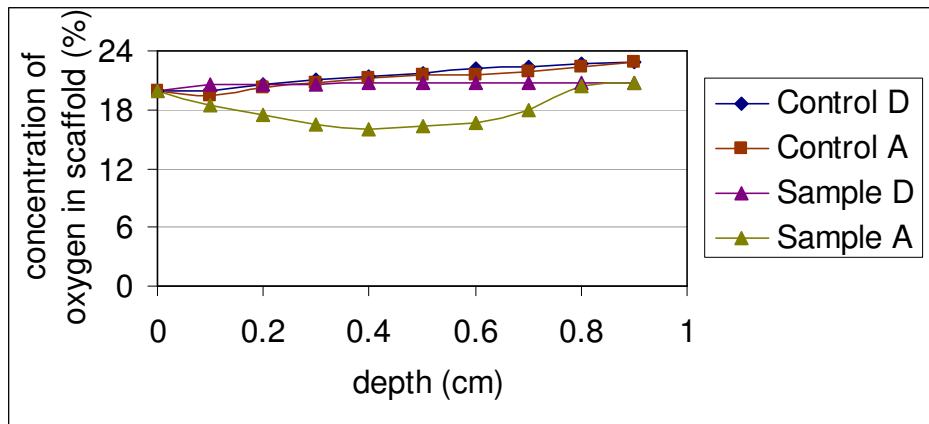
(b)

Figure 25. Mean (\pm SD) oxygen concentration profiles for controls and samples of architecture Type 3 and 4 on day 7 for (a) $n = 3$, (b) ignoring T3 control from Set 1.

thereby confirming the suspicion we had for Type 1. However, it would seem surprising as to why this would have occurred in just a couple of samples of a particular set. It turns out that this occurred for some samples from set 2, where the cells that were cultured for seeding were extremely confluent. It is highly possible that the cell pellets deposited atop the scaffolds of Type 1 and 4 had cells that had agglomerated due to their excessive

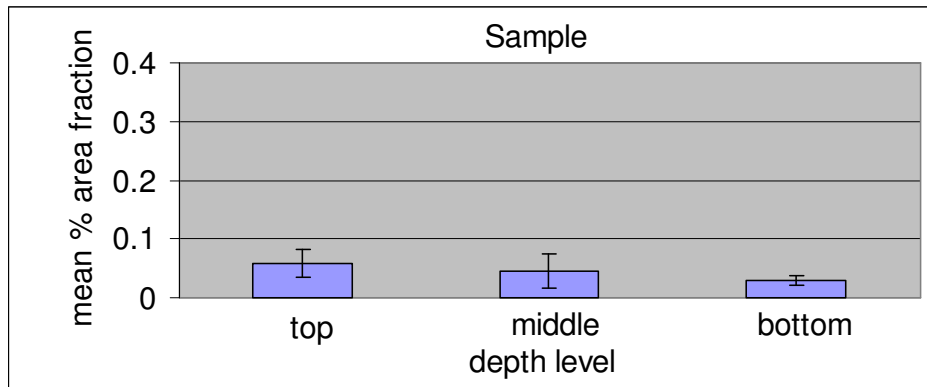


(a)

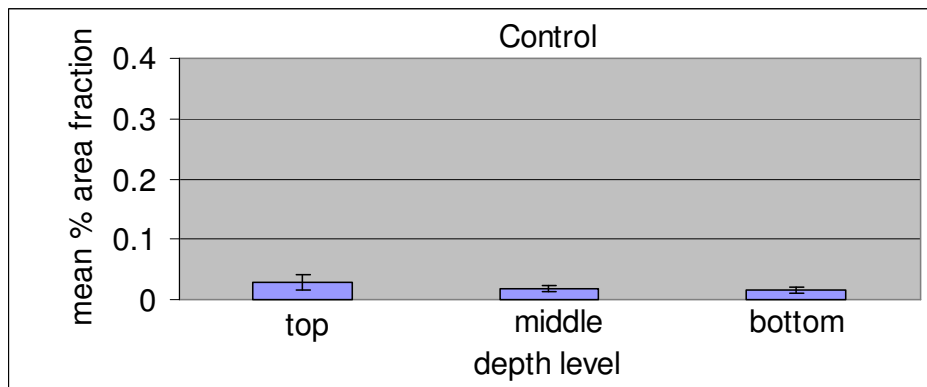


(b)

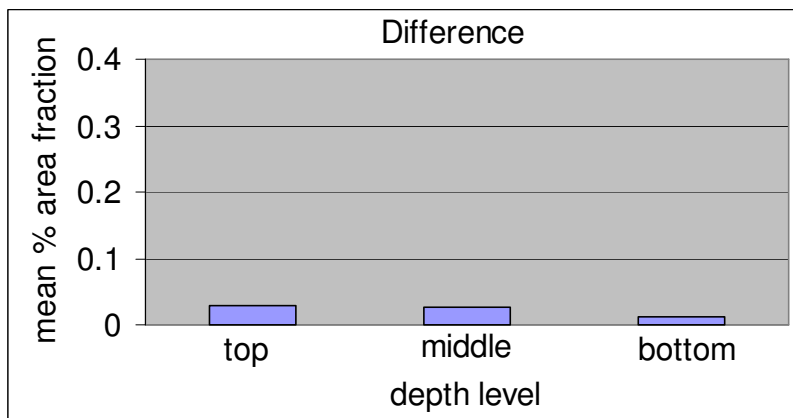
Figure 26. Oxygen concentration profiles for (a) Type 1 on day1 from set 2, (b) Type 4 on day 1 from set 2.



(a)

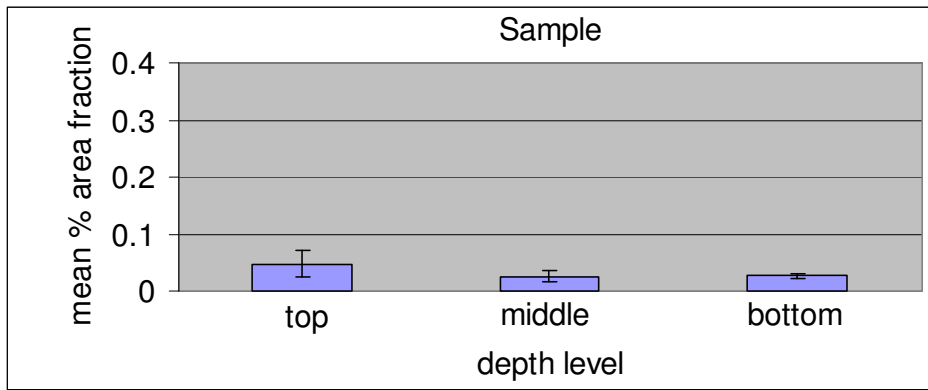


(b)

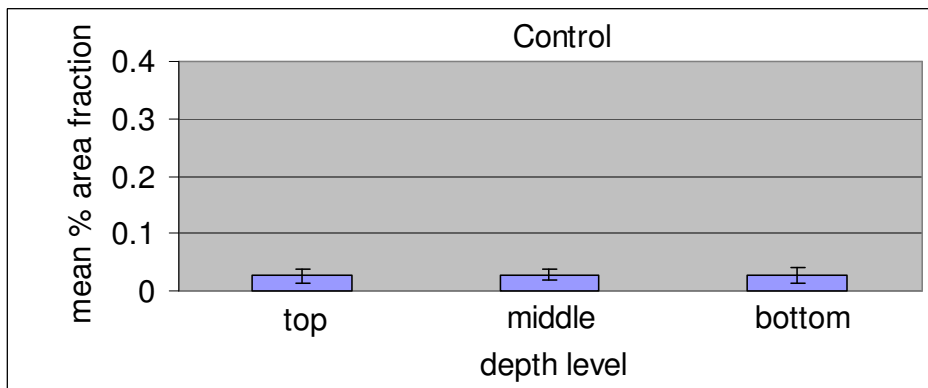


(c)

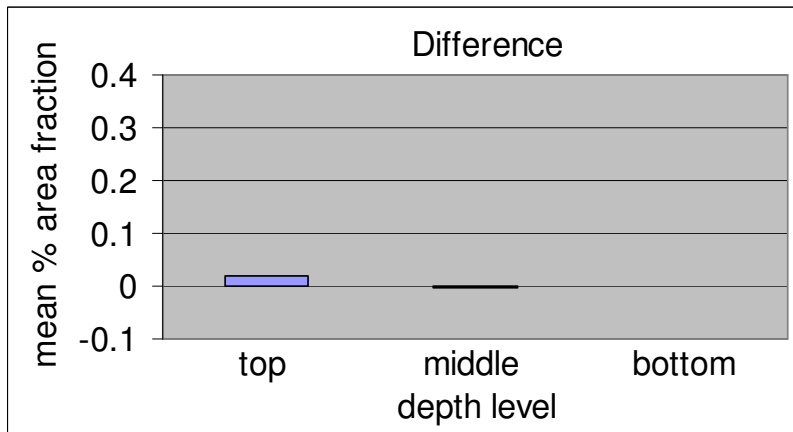
Figure 27. Type 1, day 1, set 2 (a) mean (\pm SD) % area of sample covered by live cells, (b) mean (\pm SD) % area fraction values for control i.e. background, (c) differences between corresponding mean levels of sample and control.



(a)



(b)



(c)

Figure 28. Type 4, day 1, set 2 (a) mean (\pm SD) % area of sample covered by live cells, (b) mean (\pm SD) % area fraction values for control i.e. background, (c) differences between corresponding mean levels of sample and control.

confluence. As a result, when the cell pellet was deposited, instead of percolating down the scaffold it could have remained on the top unable to penetrate the pores of the scaffold due to an increase in the size of the agglomerated cell mass. After an hour of the incubation of this construct when media was added to submerge the constructs, this agglomerate could have been washed off leaving behind very few cells in the scaffold. Thus, it is reasonable to eliminate the data sets as described above.

Another control-sample pair from the same set subjected to cell viability analysis at the conclusion of the oxygen concentration measurements allowed us to see how better cell viability data could correlate to a measurement of oxygen concentration (Figure 29, 30). From Figure 30 we observe that cell viability is maximum in the top region (Figure 30 (d)), which explains the sharp drop in the concentration profile (Figure 29) as the viable cells in the top region will be consuming most of the oxygen. The cells in the middle and bottom region are not as viable (Figure 30 (d)) and have lesser oxygen available to them than is available at the top due its depletion.

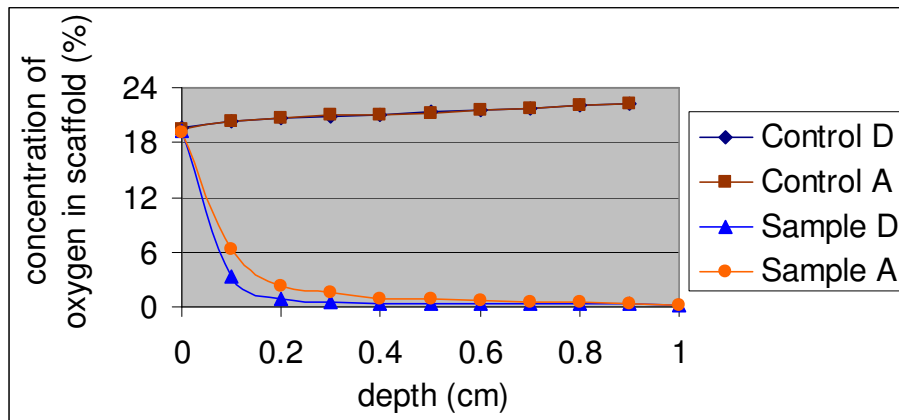
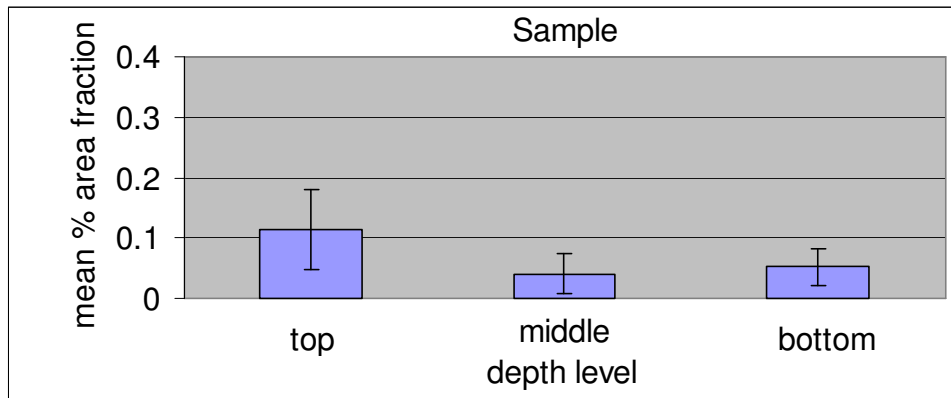
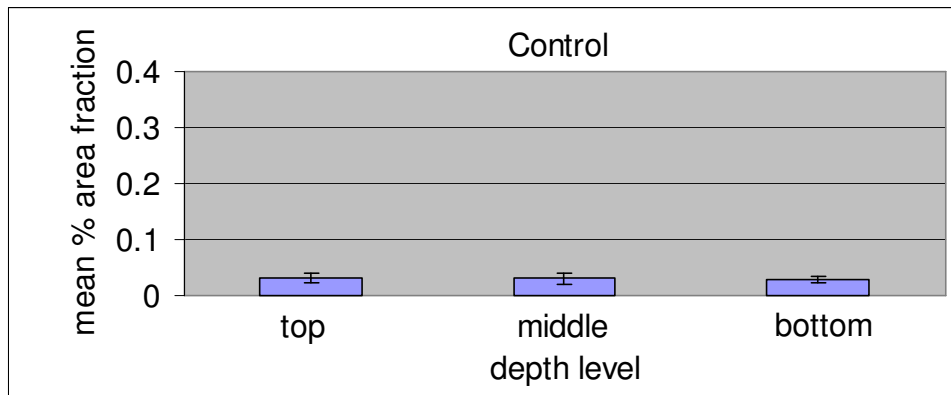


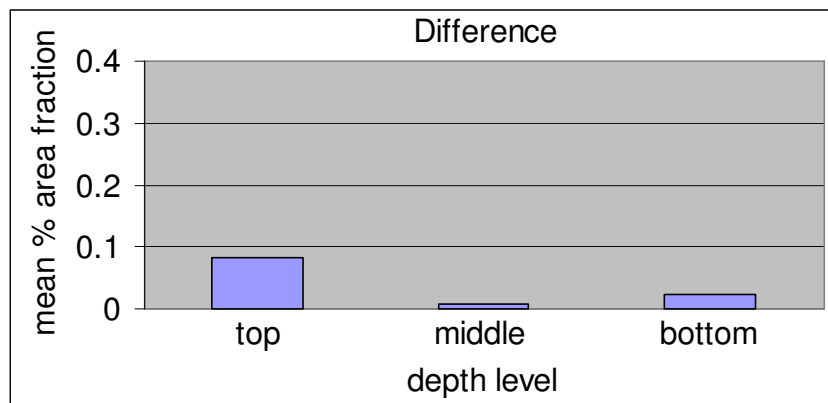
Figure 29. Oxygen concentration profile for Type 3, day 1, set 2.



(a)



(b)

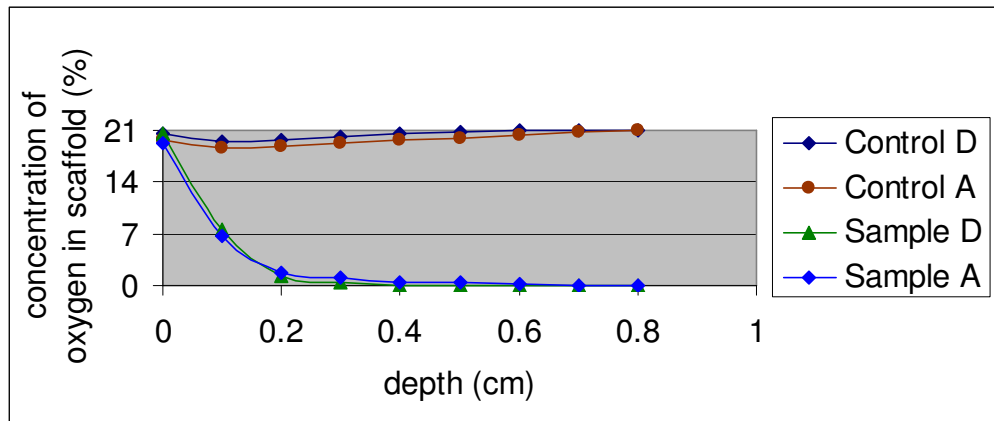


(c)

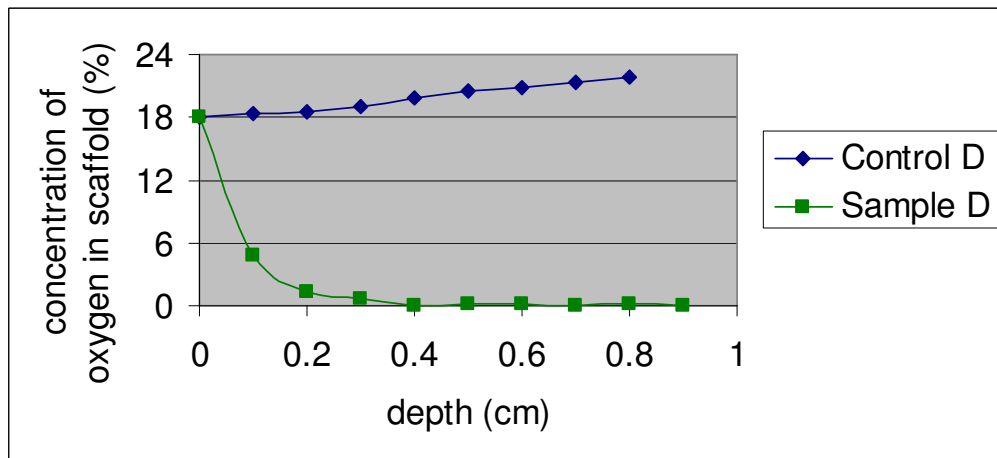
Figure 30. Type 3, day 1, set 2 (a) mean (\pm SD) % area of sample covered by live cells, (b) mean (\pm SD) % area fraction values for control i.e. background, (c) differences between corresponding mean levels of sample and control.

The control values for Types 1, 2 (Figure 24 (b)) and 3 (Figure 25 (b)) on day 7 from set 1 were eliminated because their profiles were very unsteady, once again causing the standard deviation values to become extremely large. All these controls belonged to set 1 from day 7 and had been reused from day 1. Since these were controls, no cells were deposited on them on day 1. Thus, after utilizing these scaffolds on day 1 as controls, they were put back in the incubator after changing their media and that of the samples to be used on day 7. Since no cells were deposited on these controls it was felt that reusing them would not be a problem in order to economize on the usage of these expensive, extremely difficult to procure, custom-made scaffolds. The reason for the strange profiles obtained in these controls could not be justified. One possibility that was explored was that the controls could have started degrading and gradually releasing their degradation product (hexanoic or caproic acid) in the media resulting in these strange profiles. This theory was tested by measuring oxygen concentration in full media containing three different concentrations of hexanoic acid (Aldrich, St. Louis, MO), each varying by an order of magnitude (1 ng/ml, 10 ng/ml and 100 ng/ml). However, in all three cases the oxygen concentration varied between 21-22% as a function of depth when checked over a period of 3 hours.

Values for oxygen concentration were initially recorded while descending as well as ascending, but these values were almost identical for controls as well as samples and, thus, subsequently measurements were taken only while descending (Figure 31).



(a)



(b)

Figure 31. Oxygen concentration profile for control and sample of Type 2 while (a) descending (D) and ascending (A) for Day 1, Set 1, (b) descending (D) only for Day 7, Set 3.

For a few samples oxygen concentration was recorded at 0.01 cm increments in the top 0.4 cm to get an idea of how the profiles varied, if at all, in the region closest to oxygen availability (Figure 32).

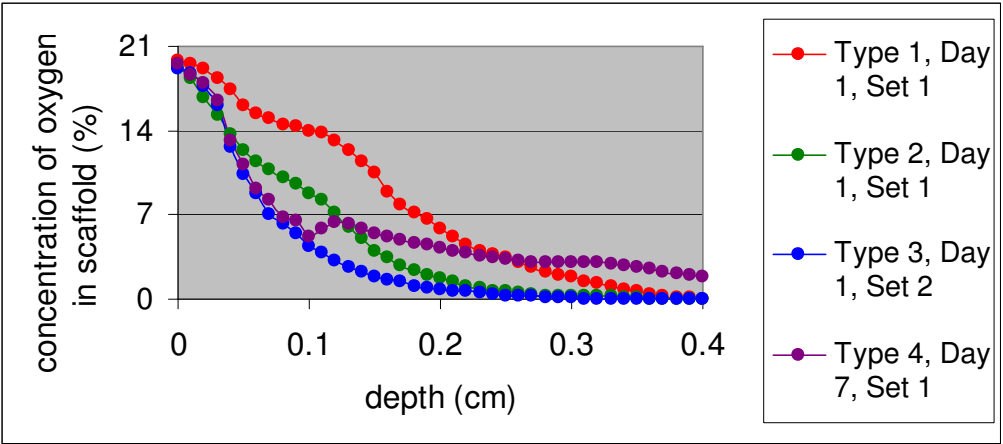
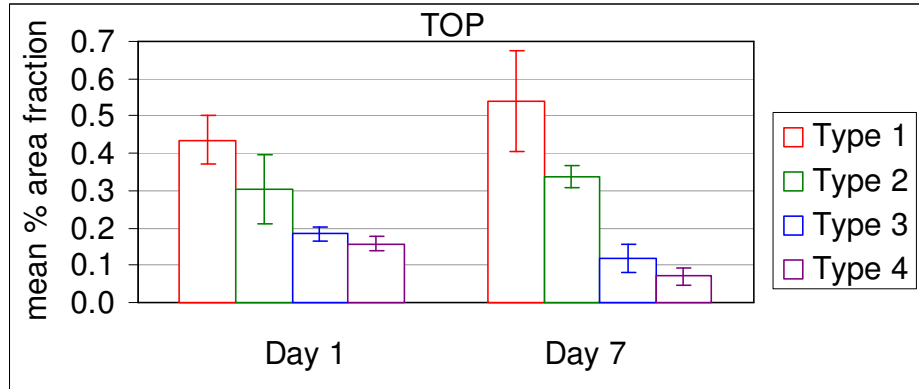


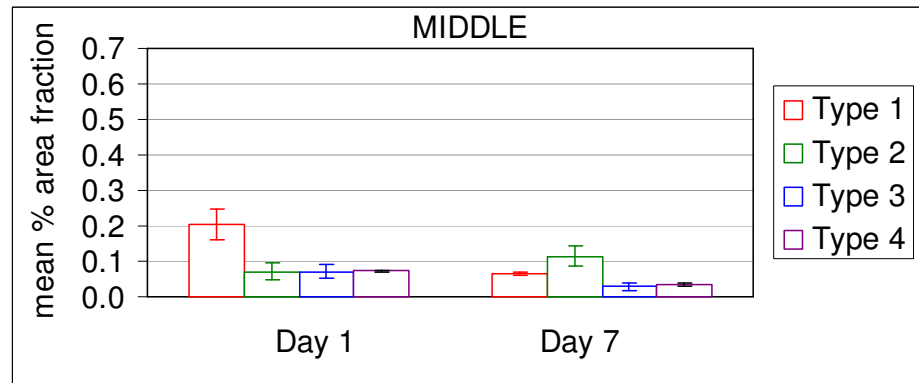
Figure 32. Oxygen concentration values in the top 0.4 cm for different scaffold types.

Chapter 13: Cell Viability Measurement Results

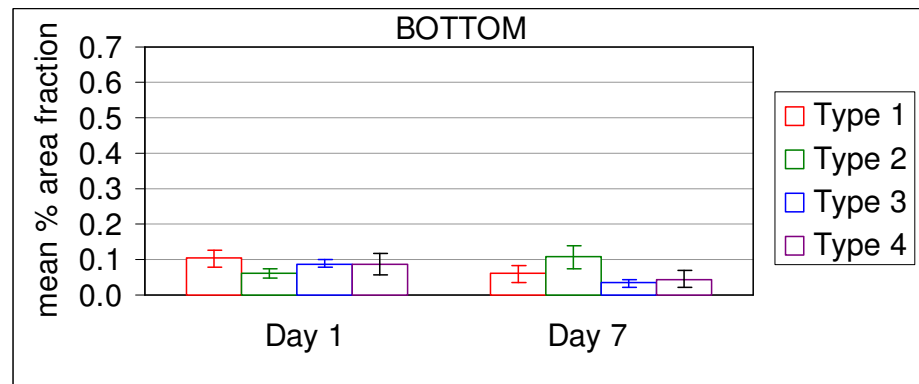
The results for cell viability are plotted for the different regions (Figure 33).



(a)



(b)



(c)

Figure 33. Cell viability as reflected by the mean % area of scaffold covered by viable cells for the different scaffold architectures for both days for the (a) top, (b) middle and (c) bottom regions. Graphs represent means ($n = 3$) \pm SD.

DEPTH COMPARISON

The top regions of all types were found to be significantly different from the middle and bottom regions at both time points, except for Type 4 on day 7. There was no difference observed between the middle and bottom regions for any architecture on any day. Thus, overall the top region was found to be significantly different from the middle and bottom regions. This could be due to greater availability of oxygen in the top region.

DAY COMPARISON

The middle regions of Types 1, 3 and 4 as well as the top region of Type 4 and bottom region of Type 3 showed a significant decline over a week and this could be attributed to diffusion constraints of nutrient delivery. Type 2 is the only scaffold architecture that showed an increase in viability over a week at all three depth regions, although none of these increases were statistically significant. This increase can be attributed to the combined effect of higher porosity (relative to Types 3 and 4) leading to better nutrient delivery, as well as higher tortuosity (relative to Type 1) resulting in greater anchorage for cells at the time of static cell seeding. However, overall, for all of the four architectures, there was no significant difference between days 1 and 7 with respect to cell viability.

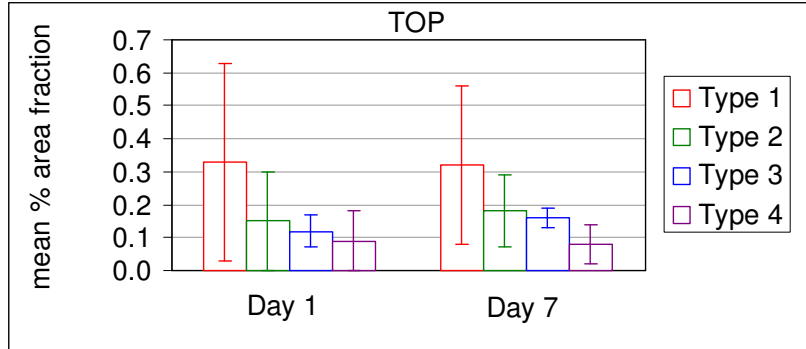
TYPE COMPARISON

For the top region on both days, Types 1 and 2 were not only significantly different from each other but also from Types 3 and 4, possibly due to the effects of tortuosity and porosity, respectively. The middle region of Type 1 was significantly different from the other types on day 1, probably owing to greater porosity and lower tortuosity. The middle and bottom regions of Type 2 were significantly different from the

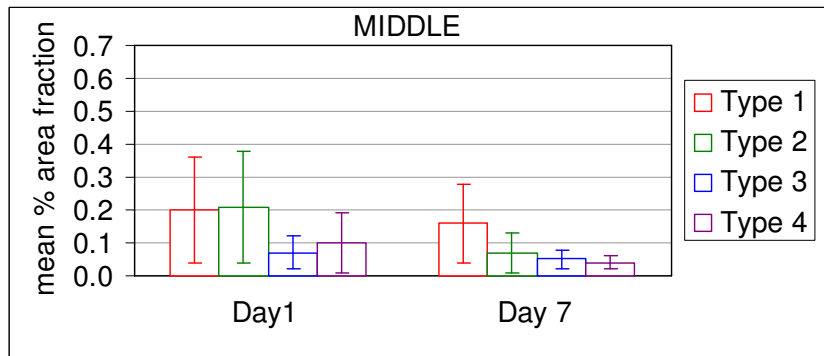
other types on day 7, and this can once again be attributed to the combined effects of porosity and tortuosity. Overall there was a significant difference between Types 1 and 3 as well as Types 1 and 4. There was no overall significant difference between Types 1 and 2, Types 2 and 3, Types 2 and 4 or Types 3 and 4.

Chapter 14: Cell Proliferation Measurement Results

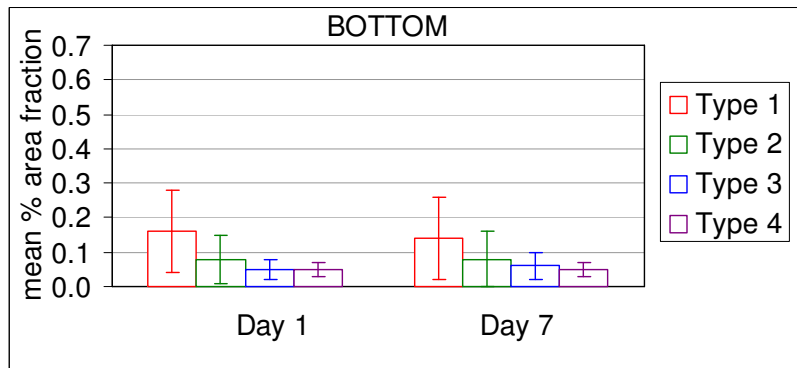
The results for cell proliferation are plotted for the different regions (Figure 34).



(a)



(b)



(c)

Figure 34. Cell proliferation as reflected by the mean % area fraction for the different scaffold architectures for both days for the (a) top, (b) middle and (c) bottom regions. Graphs represent means ($n = 3$) \pm SD.

DEPTH COMPARISON

Only the top region of Type 4 was found to have significantly more proliferation than the middle and bottom regions on day 7. There were no other significant differences found between any of the regions on either day across the four types. Overall, there were no significant differences between the different regions.

DAY COMPARISON

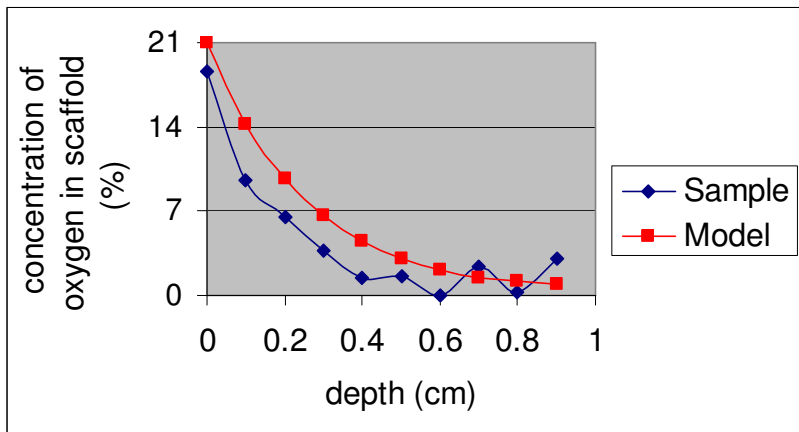
There were no significant differences found between any of the regions across the four types over the duration of a week.

TYPE COMPARISON

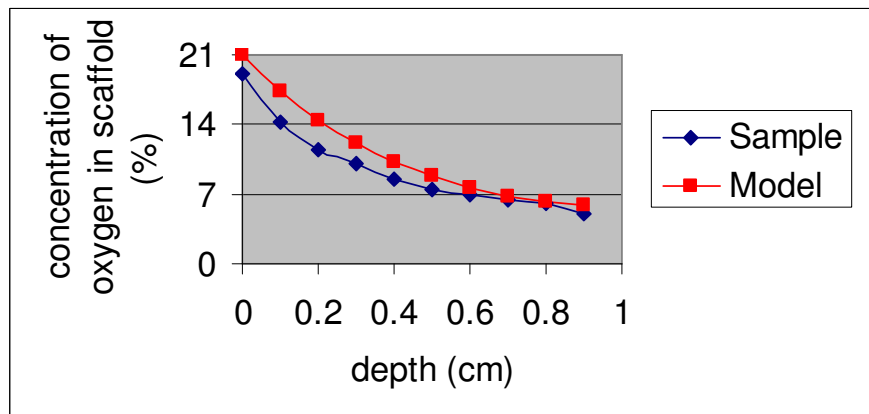
The proliferation in the middle region of Type 1 was found to be significantly greater than Type 4 for day 7. However, overall there were no significant differences between the four architectures.

Chapter 15: Validation of Diffusion Model

The diffusion model was validated by generating profiles for different values of the rate constant, K , to match the mean profiles of the samples as closely as possible (Figures 35-38). The Matlab® function 'lsqnonlin' was used to determine the value of K that minimized the non-linear least squares difference between the sample and model data.



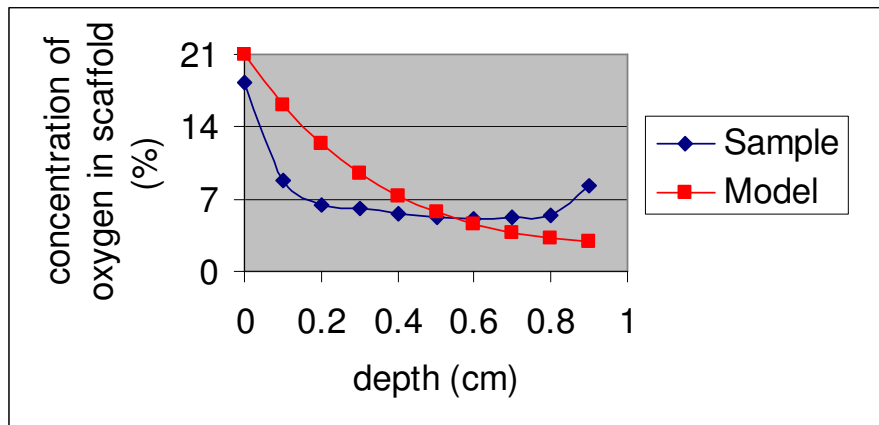
(a)



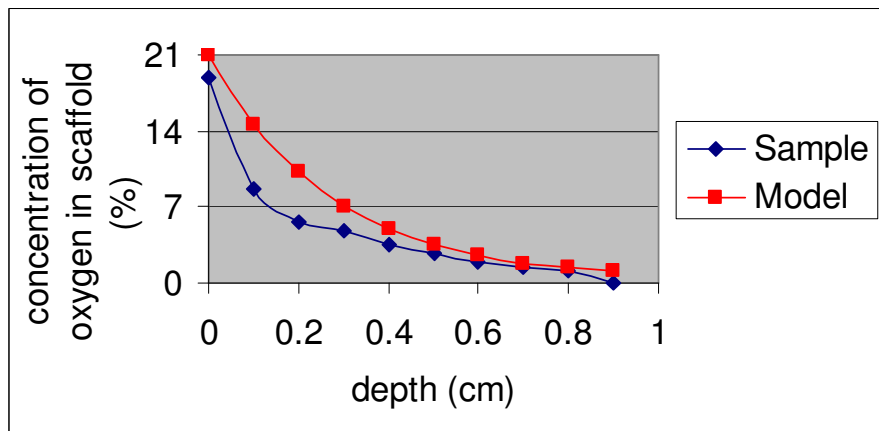
(b)

Figure 35. Profiles for the sample mean and the model for Type 1 ($P = 0.42$, $T = 1$) on (a) day 1 ($t = 86,400$ s) ($K = 0.00019$), (b) day 7 ($t = 604,800$ s) ($K = 0.00005$).

The degree of fit using the above function mainly depended on how good the initial guess (K_0) for K was. The function started at K_0 and found a value of K that minimized the sum of squares of the difference between the sample and model data, by checking for different values of K . The value of K_0 that was used for generating all the model plots was 0.0001.



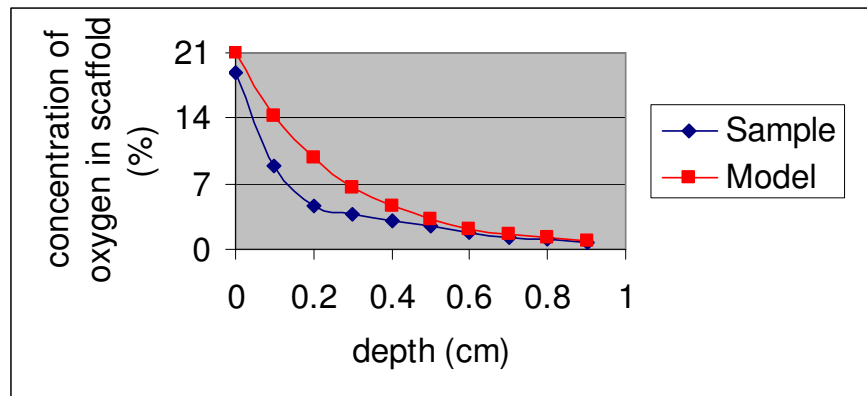
(a)



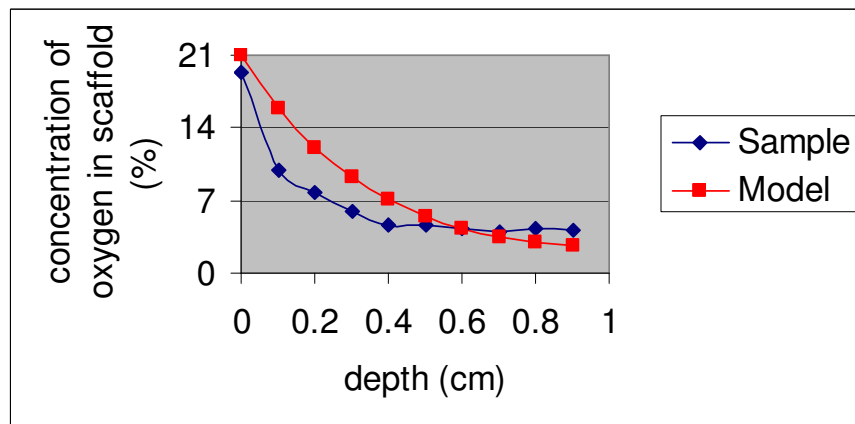
(b)

Figure 36. Profiles for the sample mean and the model for Type 2 ($P = 0.47$, $T = 1.25$) on (a) day 1 ($t = 86,400$ s) ($K = 0.00008$), (b) day 7 ($t = 604,800$ s) ($K = 0.00015$).

The Matlab® code used for determining the best K value for the four types on both days was similar, except for a few differences dictated by the variables being studied, namely, porosity (P), tortuosity (T) and time (t), as designated in the code. The values used for porosity were those obtained from the helium pycnometer, summarized in Table 1, while those used for tortuosity were obtained from Figures 1, 2 and 3. The values for time were represented in seconds for days 1 and 7. The diffusivity for oxygen in water at 37° C was assumed to be $3.0 \times 10^{-5} \text{ cm}^2/\text{sec}$.³²



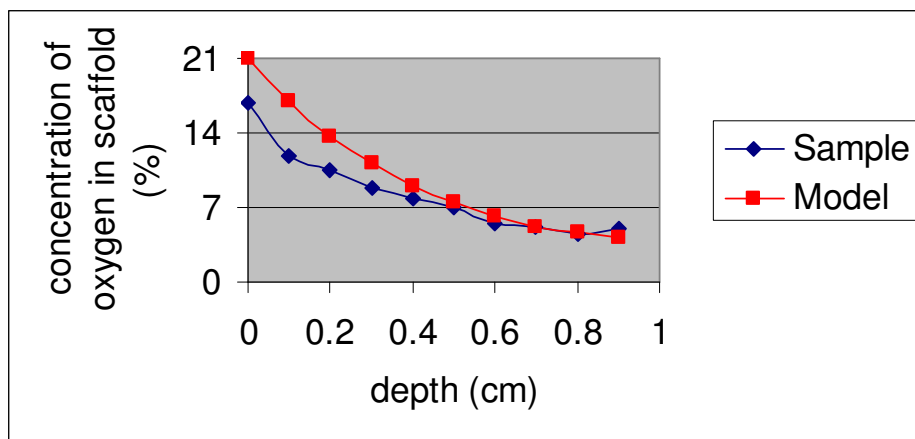
(a)



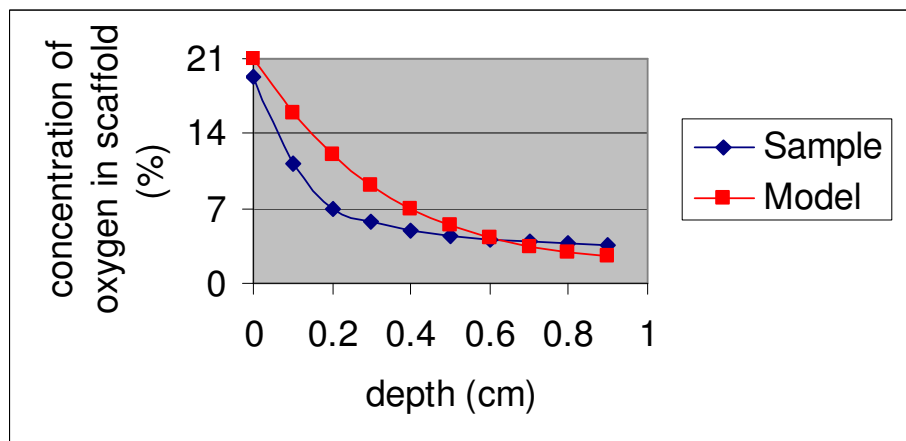
(b)

Figure 37. Profiles for the sample mean and the model for Type 3 (P = 0.25, T = 1) on (a) day 1 (t = 86,400 s) (K = 0.00011), (b) day 7 (t = 604,800 s) (K = 0.00006).

The data were obtained only up to a depth of 0.9 cm as the bottom of the scaffold was sealed with a layer of PCL and the hole for descending the microsensor could not be drilled any deeper to avoid breaking through this sealed layer. A qualitative analysis of each of the sample-model plots indicates that the model reasonably depicts the oxygen concentration depth profiles obtained from experimental observations, thereby validating the model.



(a)



(b)

Figure 38. Profiles for the sample mean and the model for Type 4 ($P = 0.27$, $T = 1.88$) on (a) day 1 ($t = 86,400$ s) ($K = 0.00002$), (b) day 7 ($t = 604,800$ s) ($K = 0.00003$).

DISCUSSION

POROSITY, PERMEABILITY AND WATER RETENTION TIME

Porosity had a significant effect on permeability and water retention time. There were no significant differences for permeability and water retention time between architectures of the same porosity but having different tortuosities. Thus, tortuosity did not appear to play as significant a role as porosity in determining the permeability of a structure. This finding supported the empirical relations described earlier. It is not clear why the measured permeability of Type 3 was lower and water retention time greater than Type 4, which are contrary to what one would expect given that Type 4 was designed to be less permeable than Type 3. However, these differences were not statistically significant.

The values of porosity estimated from the schematics (Figure 3) are up to 7.32% higher than what was obtained by using the pycnometer (Table 1). There could be two reasons for this discrepancy. The diameter of the fiber may not be exactly double that of the pore space, as was assumed in the schematic. Another contributing factor could be the assumption during the estimation of porosity that the fibers that were laid down were perfect circles when viewed from the side. However, in practice, when the molten fibers are laid down they could get slightly compressed because of the weight of the fibers placed over them, resulting in the fibers bulging slightly from the sides, thereby impacting the porosity estimation.

OXYGEN CONCENTRATION

All four architectures on both days revealed a decrease in oxygen concentration as a function of depth (Figures 22-25). The profiles seemed to be influenced by porosity and tortuosity as the oxygen concentration gradients differed from day 1 to day 7 for all four types and there were differences in the slopes of the profiles as well. The profiles for Types 1 and 2 seemed to have a similar slope on day 1 (Figure 22 (b)), however, the profile for Type 2 plateaued before the oxygen concentration could reach zero, indicating the absence of viable cells in the bottom region of Type 2 to consume oxygen. This could be attributed to the effect of tortuosity or nonhomogeneous cell distribution. The same reasoning applies to the trends observed for Types 3 and 4 on day 1 (Figure 23 (b)), although the slope of Type 3 is steeper than Type 4, indicating the presence of more viable cells consuming oxygen throughout the scaffold, and not only at the bottom. The trends observed for the four types on day 7 are more in keeping with what the model predicted with Type 1 having the least slope and porosity playing the dominant role in determining diffusion of oxygen.

Nonhomogeneous cell distribution due to static cell seeding could have contributed to the oxygen concentration profiles having steep slopes in some cases and not so steep in others, depending on how the cells got distributed within the scaffold. The most porous and least tortuous architecture (Type 1) displayed a steeper oxygen concentration profile (Figure 22 (b)) than the least porous and most tortuous architecture (Type 4) (Figure 23 (b)) on day 1, contrary to what the model predicted (Figure 21), assuming uniform cell distribution. Thus, the middle and bottom regions of the Type 4 architecture may not have been populated with cells as abundantly as Type 1, owing to the low permeability of the former, thereby generating the observed trends.

Figure 32 has plots of the oxygen concentration profiles for the different architectures in the top 0.4 cm of the construct. All exhibit the same exponentially decreasing trend with Type 1 having the minimum slope and Type 3 having the maximum, similar to the trend one observes in the permeability and water retention time data, thereby highlighting the effect that scaffold architecture has on diffusion of oxygen. Thus, an architecture that is more permeable and retains water for the shortest duration (Type 1) seems to favor better diffusion of oxygen compared to an architecture with low permeability and high water retention time (Types 3 and 4). It is not clear why the profile of Type 4 is less steep than that of Type 3 below 0.1 cm. The slope of an oxygen concentration profile in a scaffold homogeneously populated with cells could decrease for two possible reasons; either the absence of viable cells at the deeper levels to consume oxygen thereby keeping the oxygen profile relatively flat, as seems to be the case for Type 4, or due to lesser constraints on diffusion owing to an architecture more conducive for diffusion to occur, as seems to be the case for Type 1.

The oxygen concentration values for the controls as well as the samples at a depth of 0 cm (at the surface) all seem to start around 18-19% instead of 21%. The reason for this is not known. It could be that conducting the measurement just below the air-media interface could have contributed to this observation; however, what was more confounding was the apparent gradual increase in oxygen concentration as a function of depth recorded across the controls of all the scaffold architectures, up to 22.9% in one case. Initially this was attributed to drift due to transient effects, but it persisted even for long periods of equilibration (greater than 2 hours). The possibility of the degradation product of PCL (caproic acid) contributing to this disparity was also examined when increasing concentrations of caproic acid were added to full media and the oxygen concentration was recorded as a function of depth, but the response just showed a

variation from 21-22% up to a depth of 0.9 cm when measured at 0 and 3 hours. Although the chemical microsensor, that displays the oxygen concentration value, has an absolute accuracy of $\pm 2\%$ and these variations hover around the extremes of that range, no other specific cause could be attributed to this anomaly.

CELL VIABILITY

For all scaffold architectures on both days the top region supported significantly higher cell viability than the middle or bottom regions (Figure 33). However, the cell viability for Type 4 on day 7 did not follow this trend. This shows the ability of regions closer to a constant supply of oxygen to be able to better support cell viability. In case of Type 4 on day 7, the architecture had extremely low permeability, which might justify the finding. However, one must be cautious while interpreting these results. The cells were statically seeded on top of scaffolds that were pretreated with fibronectin. It was originally felt that the cells would gradually percolate through the interconnected channels of the scaffold due to gravity to distribute uniformly within the fibronectin-covered scaffold. However, the deposition of cells on the upper surface of the scaffold could have actually resulted in nonuniform cell distribution due to a majority of the cells mainly sticking to the fibronectin at the top of the scaffold. This could have produced a higher cell density in that region, thereby unfairly biasing cell distribution in the top region and the findings could be a reflection of this skewed cell distribution. Recent studies, however, support nonhomogeneous cell distribution in vascularized constructs^{19,50} and so this type of cell distribution could actually be advantageous. Moreover, the predictions of the model and the experimental observations are quite compatible.

The majority of scaffold types showed a significant decrease in cell viability over the duration of a week in the middle region, possibly owing to diffusion constraints. The bottom region had very little viability to begin with so although a decrease was observed, it was not significant in most cases. Type 4, owing to its low permeability, exhibited a significant decrease even in the top region. Type 2 was the only architecture to show a trend towards an increase in viability in all the regions over a seven day period, though none of these were significant increases. Type 1 also showed a slight increase in viability, which was also not a significant increase. However, these trends of increasing viability could be attributed to the higher porosity of Types 1 and 2. Overall, none of the scaffold architectures showed any significant increases in viability over the duration of a week, indicating that the architectural parameters selected were not suitable to sustain and promote cell growth in a scaffold with diffusion of oxygen restricted to the top surface over a 7 day period, as was done in this case.

Type 1 was found to support cell viability overall significantly greater than Types 3 and 4. However, surprisingly, Type 2 was not. In this case, the difference in tortuosity between Types 1 and 2 seems to have contributed to some extent to this finding because of which their cell viabilities were significantly different in the top regions on both days. Although the bottom and middle regions of Type 2 were significantly different from the others on day 7, it was not found to be significantly different from Types 3 and 4 overall. Thus, low tortuosity could play a role, although not as major as porosity, in being able to support cell viability over the duration of a week.

CELL PROLIFERATION

The more porous architectures (Types 1 and 2) seem to support cell proliferation across all three regions better than the less porous architectures (Type 3 and 4) on both

days. Also, between the two comprising the more porous pair, the less tortuous (Type 1) architecture supports cell proliferation better than the more tortuous architecture, for the most part. However, there was no significant difference observed in cell proliferation as a function of depth, day or architecture (Figure 34). There was an insignificant increase in proliferation observed in the top region for Types 2 and 3 over the duration of a week but other than that proliferation either remained unchanged or decreased. Proliferation remaining the same over a week would indicate that the cells are growing at the same rate on day 1 as well as on day 7, thereby indicating that a steady state had been established by day 1, as was predicted by the model. However, if the rate of proliferation remained constant one would expect the viability to increase on day 7, provided there was no cell death occurring during that period. Since there is no significant increase in cell viability over a week one would have to conclude that cell death was occurring at a rate so as to negate the effect of a constant rate of proliferation thereby maintaining viability relatively constant.

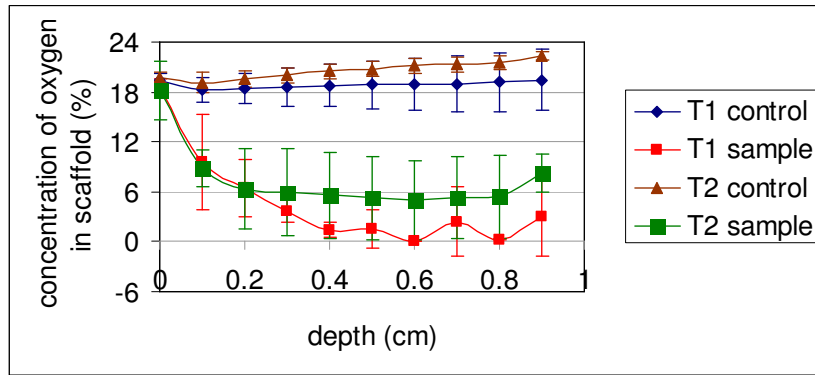
Another important contributor to this finding of no overall difference in any category was the huge standard deviation observed in the data. A reason for the large variability in the data could be the high autofluorescence of the PCL scaffolds treated with the BrdU kit (Figures 18 (c) and 19 (c)). Moreover, although MG63 cells are immortalized and can theoretically undergo unlimited passages without compromising their behavior, practically their activity does get negatively affected with greater number of passages, sometimes causing the cells to senesce, thereby making them lose their ability to divide. The laboratory, however, does not use cells after 14 passages to prevent this from happening. Although all the scaffolds in a single set were treated with cells that had undergone the same number of passages, this was not necessarily true from one set to the next. Another contributing factor could be the method employed for sectioning the

constructs. The method of sectioning could have caused many of the cells in the immediate vicinity of the blades to detach and since the different scaffold architectures would have offered differing resistance to the blades, the detachment of cells across different architectures may not have been the same, thereby further adding to the variability in data.

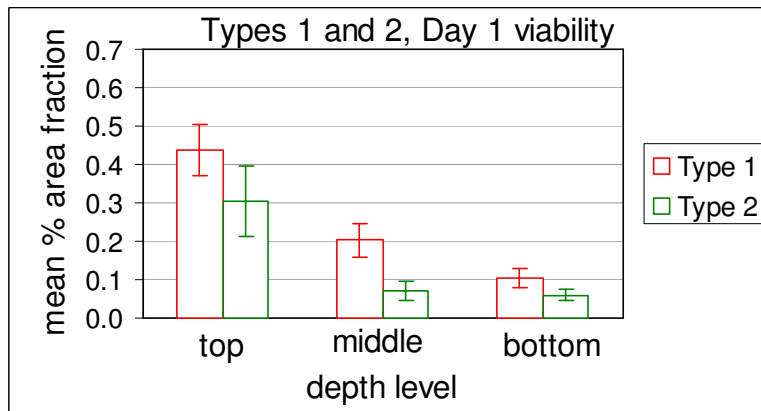
CORRELATION BETWEEN OXYGEN CONCENTRATION, CELL VIABILITY AND CELL PROLIFERATION

Statistically, it is not appropriate to draw standard correlations between these 3 studies as they were all conducted on different samples, although belonging to the same architecture. However, looking at the trends in data qualitatively one can state that some correlations between the various sets of data (Figures 39-42) can be drawn if certain assumptions are made. From Figures 39 and 40 we see that on day 1 the oxygen concentration profile for Type 1 is steeper than Type 2, and that of Type 3 is steeper than Type 4 (in the top region), indicating the presence of more viable and/or proliferating cells consuming oxygen at greater depths for the less tortuous architectures (Types 1 and 3), which is supported by the viability and proliferation data. Since scaffold tortuosity is a component of the effective diffusivity of oxygen in the scaffold, we can see the role that internal scaffold architecture plays in governing the effect of this crucial parameter. Porosity, on day 1, did not appear to play as significant a role as tortuosity, as the average oxygen concentration profile for Type 1 seemed to be just slightly steeper than Type 3 and that of Type 2 seemed to be just slightly steeper than that of Type 4.

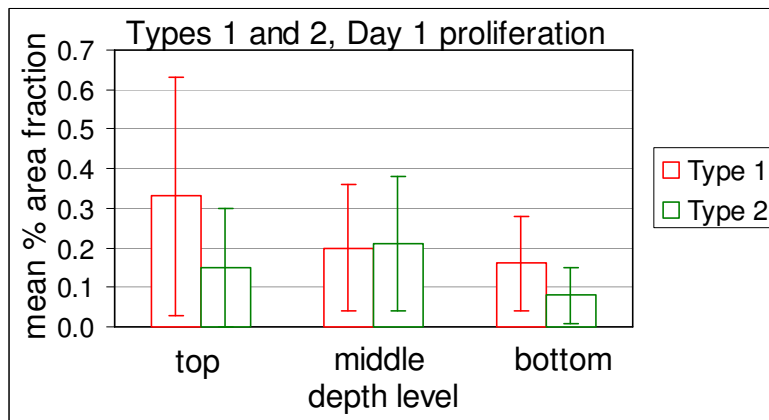
From Figure 41, however, we see that by day 7 the mean oxygen concentration profile for Type 2 has a steeper slope than Type 1, indicating the presence of more viable



(a)

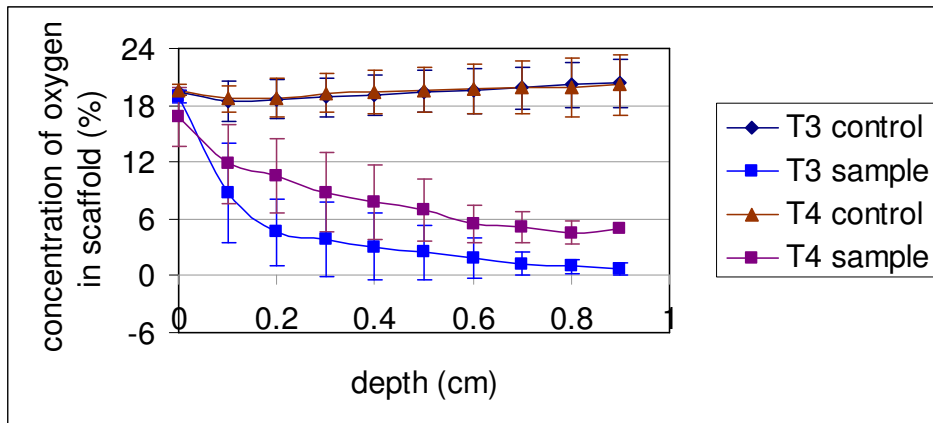


(b)

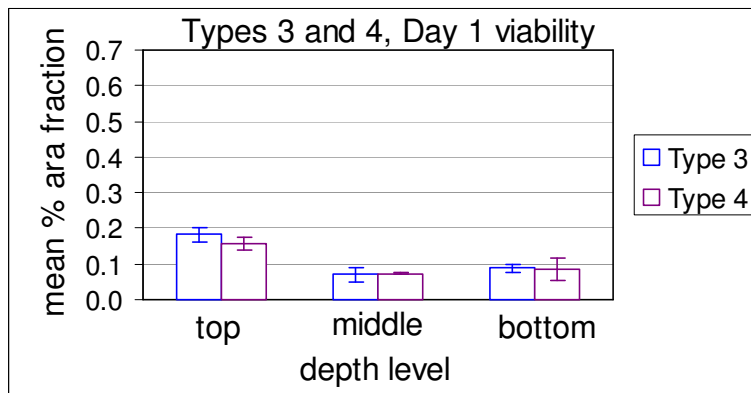


(c)

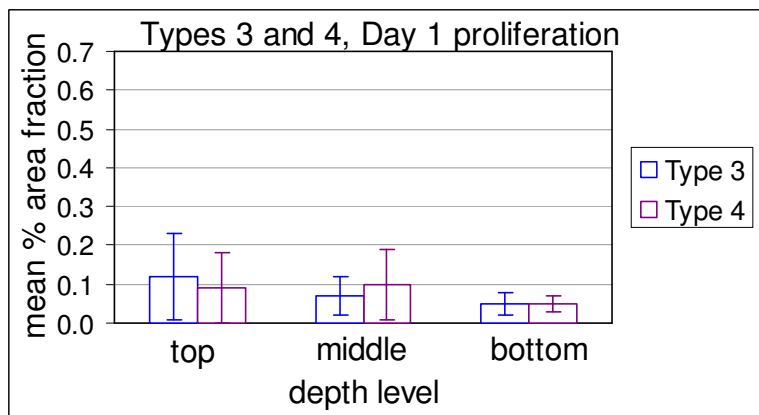
Figure 39. (a) Mean oxygen concentration, (b) mean cell viability, (c) mean cell proliferation for Types 1 and 2 on day 1.



(a)



(b)

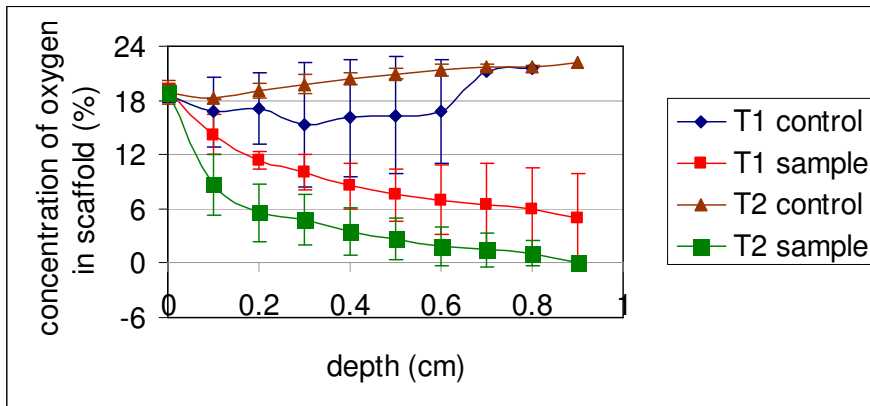


(c)

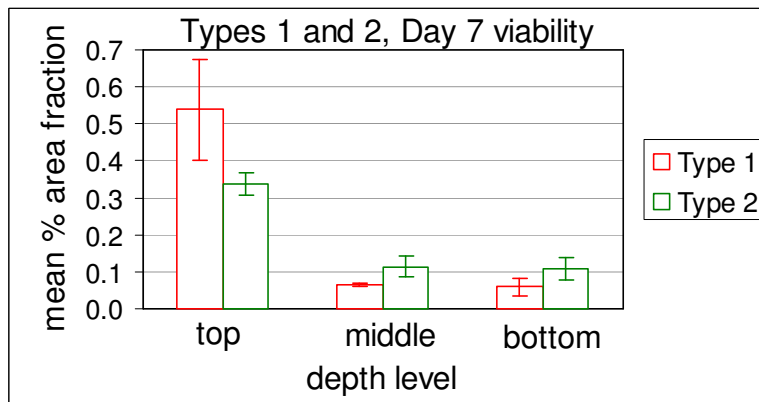
Figure 40. (a) Mean oxygen concentration, (b) mean cell viability, (c) mean cell proliferation for Types 3 and 4 on day 1.

cells at greater depths for the more tortuous architecture (Type 2), which is supported by the viability data for the middle and bottom regions (Figure 42 (b)). The viability data for the top region of Type 1 is significantly greater than that for Type 2, implying that the cells in the top region for Type 1 consumed most of the oxygen leaving little for the cells below, resulting in lower levels of viability in the middle and bottom regions. This finding is counterintuitive given that one would assume the less tortuous architecture to support more viability at greater depths, and is thus difficult to explain. This can be attributed to the possible lack of oxygen at the lower levels due to diffusion constraints causing the cells to concentrate close to the region of greater oxygen availability i.e. the top region, to remain viable, where their proliferation is also greater. Increased proliferation in the top region would result in greater consumption of oxygen locally, thereby further depriving the cells at greater depths from receiving oxygen. The more tortuous architecture (Type 2) might make it more difficult for cells to migrate towards greater availability of oxygen and they might have to make do with what they get at greater depths, which seems to adversely affect their proliferation.

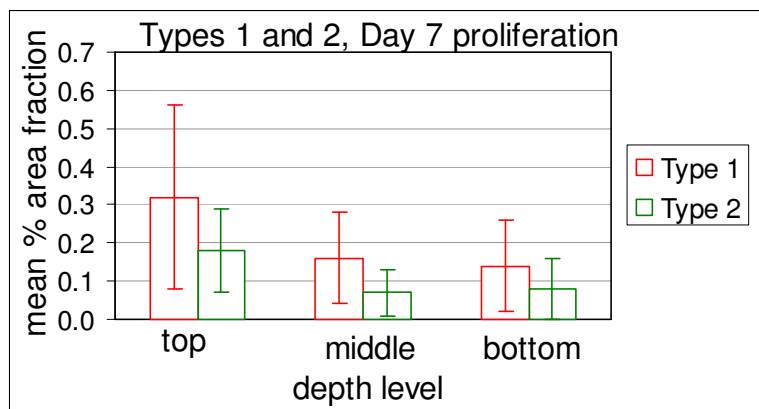
From Figure 42 we see that by day 7 the oxygen concentration profiles for Types 3 and 4 overlap, which is reflected in the similar trends observed for viability and proliferation. Tortuosity, therefore, does not seem to play a significant role on day 7. Also, the above argument of cell migration seems to be restricted to architectures of greater porosity. The low porosity possessed by architectures of Types 3 and 4 would understandably pose a much greater obstacle to cell migration than the architectures of higher porosity (Types 1 and 2). The oxygen concentration profiles for Types 3 and 4 seem to plateau in the bottom region, while they continue to slope downwards for Types 1 and 2 (Figure 42 (a)), once again highlighting the effect of differences in diffusion, this time attributable to porosity.



(a)

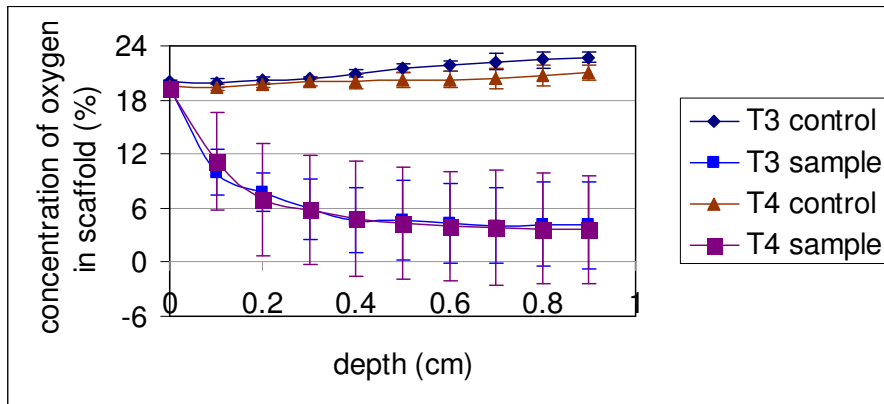


(b)

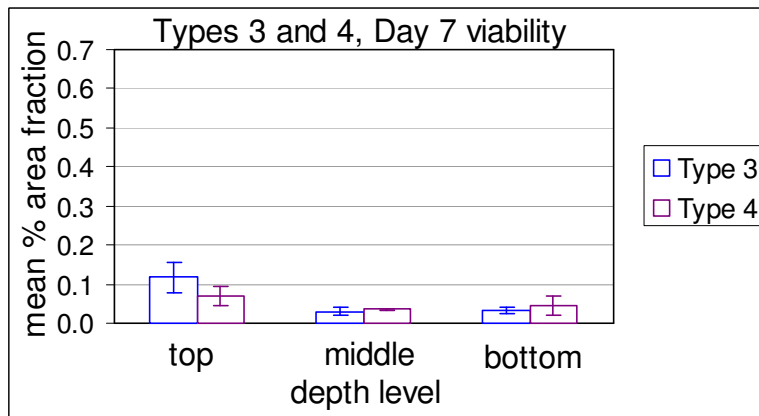


(c)

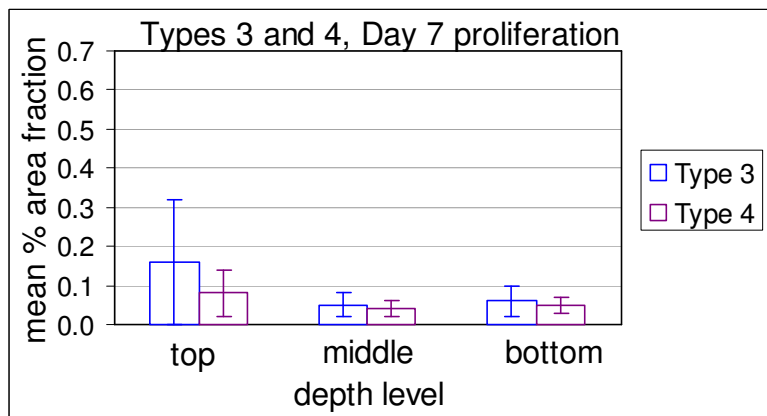
Figure 41 (a) Mean oxygen concentration, (b) mean cell viability, (c) mean cell proliferation for Types 1 and 2 on day 7.



(a)



(b)



(c)

Figure 42. (a) Mean oxygen concentration, (b) mean cell viability, (c) mean cell proliferation for Types 3 and 4 on day 7.

Thus, tortuosity seems to play a predominant role in determining the oxygen concentration profiles on day 1 while porosity seems to be the major deciding factor on day 7. Both of these architectural parameters contribute to diffusion through the scaffold, thereby highlighting its importance.

DIFFUSION MODEL

The diffusion model reasonably predicted experimentally obtained oxygen concentration profiles. Qualitatively, the model fit the sample measurements quite well for different values of the rate constant, K . The measured values of porosity and the estimated values of tortuosity that were used in the model seemed to appropriately reflect the architectural parameters of the different types of scaffolds. Making the effective diffusivity of oxygen within the scaffold a function of porosity and tortuosity helped to accurately portray the dependence of diffusion of oxygen within the scaffold on architectural parameters.

The major reasons for the inability of the profiles generated by the model to exactly overlap with the experimental data are the assumptions of uniform cell distribution and oxygen consumption as well as the difference in their starting values. As was mentioned earlier, the experimental data have an oxygen concentration of about 18-19% at the surface, whereas the model assumes this value to be 21%, as this is the atmospheric composition of oxygen. The model can be made more accurate by expanding the rate constant to incorporate terms of cell density and oxygen consumption at different depths. Including concentration-dependent diffusion coefficients as well as the changing porosities and tortuosities during the growth of the cells in the scaffold would help make the model more powerful. In spite of its inadequacies the prediction of the model is quite good.

CONCLUSIONS

We have successfully investigated the oxygen concentration profiles within the interior of architecturally distinct constructs. Qualitative analysis allowed us to observe trends based on the architectural differences between the scaffolds. All the architectures displayed an exponentially decreasing trend in oxygen concentration as a function of depth on days 1 and 7. The slopes of the profiles varied as a function of porosity, tortuosity, cell distribution and time.

We have successfully evaluated cell viability and proliferation in the interior of these constructs and attempted to qualitatively correlate the findings with the results obtained for oxygen concentration measurement as a function of depth. The three sets of data seem to correlate well and emphasize the importance of tortuosity on day 1 and porosity on day 7, in influencing the observed trends, thereby strengthening the case to further explore the effects of different architectural parameters on cell function.

A simple diffusion model was mathematically developed to predict the oxygen concentration profiles and the model was successfully validated.

Based on the findings from the study on cell viability, where in most of the significant differences were observed, we can conclude that the architecture with the most porosity and least tortuosity is able to best sustain cell viability in the region closest to oxygen supply.

Porosity seems to play a greater role than tortuosity in not only influencing architecture-dependent parameters like permeability and water retention time, but also in supporting basic cell functions like viability, proliferation and oxygen diffusion.

References

- ¹Agrawal, C. M., J. S. McKinney, D. Huang and K. A. Athanasiou. "The use of the vibrating particle technique to fabricate highly porous and permeable biodegradable scaffolds." In: *Synthetic Bioabsorbable Polymers for Implants, ASTM STP 1396*, edited by C. M. Agrawal, J. E. Parr and S. T. Lin. West Conshohocken, PA: American Society for Testing and Materials, 2000, pp. 99-114.
- ²Agrawal, C. M., J. S. McKinney, D. Lanctot and K. A. Athanasiou. Effects of fluid flow on the in vitro degradation kinetics of biodegradable scaffolds for tissue engineering. *Biomaterials* 21(23): 2443-2452, 2000.
- ³Agrawal, C. M. and J. L. Ong. Basics of tissue engineering scaffolds. *personal communication*, 2003.
- ⁴Agrawal, C. M. and R. B. Ray. Biodegradable polymeric scaffolds for musculoskeletal tissue engineering. *J. Biomed. Mater. Res.* 55(2): 141-150, 2001.
- ⁵Arcaute, K., B. K. Mann and R. B. Wicker. Stereolithography of three-dimensional bioactive poly(ethylene glycol) constructs with encapsulated cells. *Annals of Biomedical Engineering* 34(9): 1429-1441, 2006.
- ⁶Athanasiou, K. A., J. P. Schmitz and C. M. Agrawal. The effects of porosity on degradation of PLA-PGA implants. *Tissue Eng.* 4: 53-63, 1998.
- ⁷Boby, J. D., R. M. Pilliar, H. U. Cameron and G. C. Weatherly. The optimum pore size for the fixation of porous-surfaced metal implants by the ingrowth of bone. *Clin. Orthop.* 150: 263-270, 1980.
- ⁸Boby, J. D., R. M. Pilliar, H. U. Cameron, G. C. Weatherly and G. M. Kent. The effect of porous surface configuration on the tensile strength of fixation of implants by bone ingrowth. *Clin. Orthop.* 149: 291-298, 1980.
- ⁹Borden, M., S. F. El-Amin, M. Attawia and C. T. Laurencin. Structural and human cellular assessment of a novel microsphere-based tissue engineered scaffold for bone repair. *Biomaterials* 24(4): 597-609, 2003.
- ¹⁰Botchwey, E. A., M. A. Dupree, S. R. Pollack, E. M. Levine and C. T. Laurencin. Tissue engineered bone: Measurement of nutrient transport in three-dimensional matrices. *J. Biomed. Mater. Res.* 67A: 357-367, 2003.
- ¹¹Botchwey, E. A., S. R. Pollack, S. El-Amin, E. M. Levine, R. S. Tuan and C. T. Laurencin. Human osteoblast-like cells in three-dimensional culture with fluid flow. *Biorheology* 40(1-3): 299-306, 2003.
- ¹²Cao, T., K.-H. Ho and S.-H. Teoh. Scaffold design and in vitro study of osteochondral coculture in a three-dimensional porous polycaprolactone scaffold fabricated by fused deposition modeling. *Tissue Eng.* 9 Supplement 1(4): S103-S112, 2003.
- ¹³Chu, T.-M. G., D. G. Orton, S. J. Hollister, S. E. Feinberg and J. W. Halloran. Mechanical and in vivo performance of hydroxyapatite implants with controlled architectures. *Biomaterials* 23: 1283-1293, 2002.
- ¹⁴Chua, C. K., K. F. Leong, K. H. Tan, F. E. Wiria and C. M. Cheah. Development of tissue scaffolds using selective laser sintering of polyvinyl alcohol/hydroxyapatite biocomposite for craniofacial and joint defects. *Journal of Materials Science: Materials in Medicine* 15(10): 1113-1121, 2004.

- ¹⁵Chung, C. A., C. W. Yang and C. W. Chen. Analysis of cell growth and diffusion in a scaffold for cartilage tissue engineering. *Biotechnol. Bioeng.* 94(6): 1138-1146, 2006.
- ¹⁶Chung, C. A., C. W. Chen, C. P. Chen and C. S. Tseng. Enhancement of cell growth in tissue-engineering constructs under direct perfusion: modeling and simulation. *Biotechnol. Bioeng.* 97(6): 1603-1616, 2007.
- ¹⁷Collins, R. E. *Flow of Fluids Through Porous Materials*. Tulsa, Oklahoma: PennWell Publishing Company, 1976, 270 pp.
- ¹⁸Cooke, M. N., J. P. Fisher, D. Dean, C. Rimnac and A. G. Mikos. Use of stereolithography to manufacture critical-sized 3D biodegradable scaffolds for bone ingrowth. *J. Biomed. Mater. Res.* 64B(2): 65-69, 2003.
- ¹⁹Croll, T. I., S. Gentz, K. Mueller, M. Davidson, A. J. O'Connor, G. W. Stevens and J. J. Cooper-White. Modelling oxygen diffusion and cell growth in a porous, vascularising scaffold for soft tissue engineering applications. *Chemical Engineering Science* 60(17): 4924-4934, 2005.
- ²⁰Darling, A. L. and W. Sun. 3D microtomographic characterization of precision extruded poly- ϵ -caprolactone scaffolds. *Journal of Biomedical Materials Research Part B: Applied Biomaterials* 70B(2): 311-317, 2004.
- ²¹Dellinger, J. G., J. R. Cesarano and R. D. Jamison. Robotic deposition of model hydroxyapatite scaffolds with multiple architectures and multiscale porosity for bone tissue engineering. *Journal of Biomedical Materials Research. Part A* 82A(2): 383-394, 2007.
- ²²Draghi, L., S. Resta, M. G. Pirozzolo and M. C. Tanzi. Microspheres leaching for scaffold porosity control. *Journal of Materials Science: Materials in Medicine* 16(12): 1093-1097, 2005.
- ²³Freed, L. E., G. Vunjak-Novakovic, R. J. Biron, D. B. Eagles, D. C. Lesnoy, S. K. Barlow and R. Langer. Biodegradable polymer scaffolds for tissue engineering. *Biotechnology (NY)* 12(7): 689-693, 1994.
- ²⁴Galban, C. J. and B. R. Locke. Analysis of cell growth kinetics and substrate diffusion in a polymer scaffold. *Biotechnol. Bioeng.* 65(2): 121-132, 1999.
- ²⁵Giordano, R. A., B. M. Wu, S. W. Borland, L. G. Cima, E. M. Sachs and M. J. Cima. Mechanical properties of dense polylactic acid structures fabricated by three dimensional printing. *J. Biomater. Sci. Polym. Ed.* 8(1): 63-75, 1996.
- ²⁶Goldstein, A. S., G. Zhu, G. E. Morris, R. K. Meszlenyi and A. G. Mikos. Effect of osteoblastic culture conditions on the structure of poly(DL-Lactic-co-Glycolic Acid) foam scaffolds. *Tissue Eng.* 5(5): 421-433, 1999.
- ²⁷Griffon, D. J., M. R. Sedighi, D. V. Schaeffer, J. A. Eurell and A. L. Johnson. Chitosan scaffolds: interconnective pore size and cartilage engineering. *Acta biomaterialia* 2(3): 313-320, 2006.
- ²⁸Gross, K. A. and L. M. Rodriguez-Lorenzo. Bioedgradable composite scaffolds with an interconnected spherical network for bone tissue engineering. *Biomaterials* 25(20): 4955-4962, 2004.
- ²⁹Hao, L., M. M. Savalani, Y. Zhang, K. E. Tanner and R. A. Harris. Selective laser sintering of hydroxyapatite reinforced polyethylene composites for bioactive implants and tissue scaffold development. *Proceedings of the Institution of Mechanical Engineers. Part H, Journal of Engineering in Medicine* 220(4): 521-531, 2006.

- ³⁰Harley, B. A., A. Z. Hastings, I. V. Yannas and A. Sannino. Fabricating tubular scaffolds with a radial pore size gradient by a spinning technique. *Biomaterials* 27(6): 866-874, 2006.
- ³¹Haselgrove, J. C., I. M. Shapiro and S. F. Silverton. Computer modeling of the oxygen supply and demand of cells of the avian growth cartilage. *The American Journal of Physiology* 265(2): C497-C506, 1993.
- ³²Himmelblau, D. M. Diffusion of dissolved gases in liquids. *Chemical Reviews* 64: 527-550, 1964.
- ³³Hollister, S. J., C. Y. Lin, E. Saito, C. Y. Lin, R. D. Schek, J. M. Taboas, J. M. Williams, B. Partee, C. L. Flanagan, A. Diggs, E. N. Wilke, G. H. Van Lenthe, R. Muller, T. Wirtz, S. Das, S. E. Feinberg and P. H. Krebsbach. Engineering craniofacial scaffolds. *Orthodontics and Craniofacial Research* 8(3): 162-173, 2005.
- ³⁴Hou, Q., D. W. Grijpma and J. Feijen. Porous polymeric structures for tissue engineering prepared by a coagulation, compression moulding and salt leaching technique. *Biomaterials* 24: 1937-1947, 2003.
- ³⁵Hou, Q., D. W. Grijpma and J. Feijen. Preparation of interconnected highly porous polymeric structures by a replication and freeze-drying process. *J. Biomed. Mater. Res.* 67(2): 732-740, 2003.
- ³⁶Howk, D. and T. M. Chu. Design variables for mechanical properties of bone tissue scaffolds. *Biomedical Sciences Instrumentation* 42: 278-283, 2006.
- ³⁷Hu, Y., D. W. Grainger, S. R. Winn and J. O. Hollinger. Fabrication of poly(α -hydroxy acid) foam scaffolds using multiple solvent systems. *J. Biomed. Mater. Res.* 59: 563-572, 2002.
- ³⁸Huang, Y. C., Y. Y. Huang, C. C. Huang and H. C. Liu. Manufacture of porous polymer nerve conduits through a lyophilizing and wire-heating process. *Journal of Biomedical Materials Research Part B: Applied Biomaterials* 74(1): 659-664, 2005.
- ³⁹Hutmacher, D. W., T. Schantz, I. Zein, K. W. Ng, S. H. Teoh and K. C. Tan. Mechanical properties and cell cultural response of polycaprolactone scaffolds designed and fabricated via fused deposition modeling. *J. Biomed. Mater. Res.* 55(2): 203-216, 2001.
- ⁴⁰Hutmacher, D. W., S. H. Teoh, I. Zein, K. W. Ng, J.-T. Schantz and J. C. Leahy. "Design and fabrication of a 3D scaffold for tissue engineering bone." In: *Synthetic Bioabsorbable Polymers for Implants*, edited by C. M. Agrawal, J. E. Parr and S. T. Lin. West Conshohocken, PA: ASTM, 2000, pp. 152-167.
- ⁴¹Hutmacher, D. W., M. Sittinger and M. V. Risbund. Scaffold-based tissue engineering: rationale for computer-aided design and solid free-form fabrication systems. *Trends Biotechnol.* 22(7): 354-362, 2004.
- ⁴²Ishaug-Riley, S., G. M. Crane, M. J. Miller, A. W. Yasko, M. J. Yaszemski and A. G. Mikos. Bone formation by three-dimensional stromal osteoblast culture in biodegradable polymer scaffolds. *J. Biomed. Mater. Res.* 36(1): 17-28, 1997.
- ⁴³Ishaug-Riley, S., G. M. Crane-Kruger, M. J. Yaszemski and A. G. Mikos. Three-dimensional culture of rat calvarial osteoblasts in porous biodegradable polymers. *Biomaterials* 19(15): 1405-1412, 1998.

- ⁴⁴Itälä, A., H. O. Ylänen, C. Ekholm, K. H. Karisson and H. T. Aro. Pore diameter of more than 100 µm is not requisite for bone ingrowth in rabbits. *J. Biomed. Mater. Res.* 58: 679-683, 2001.
- ⁴⁵Karande, T. S., J. L. Ong and C. M. Agrawal. Diffusion in musculoskeletal tissue engineering scaffolds: design issues related to porosity, permeability, architecture and nutrient mixing. *Annals of Biomedical Engineering* 32(12): 1728-1743, 2004.
- ⁴⁶Kellner, K., G. Liebsch, I. Klimant, O. S. Wolfbeis, T. Blunk, M. B. Schulz and A. Göpferich. Determination of oxygen gradients in engineered tissue using a fluorescent sensor. *Biotechnol. Bioeng.* 80(1): 73-83, 2002.
- ⁴⁷Khalyfa, A., S. Vogt, J. Weisser, G. Grimm, A. Rechtenbach, W. Meyer and M. Schnabelrauch. Development of a new calcium phosphate powder-binder system for the 3D printing of patient specific implants. *Journal of Materials Science: Materials in Medicine* article(in): press, 2007.
- ⁴⁸Knackstedt, M. A., C. H. Arns, T. J. Senden and K. Gross. Structure and properties of clinical coralline implants measured via 3D imaging and analysis. *Biomaterials* 27(13): 2776-2786, 2006.
- ⁴⁹Kuboki, Y., Q. Jin and H. Takita. Geometry of carriers controlling phenotypic expression in BMP-induced osteogenesis and chondrogenesis. *J. Bone Joint Surg.* 83-A(Supplement 1, Part 2): S1-105 - S101-115, 2001.
- ⁵⁰Landman, K. A. and A. Q. Cai. Cell Proliferation and Oxygen Diffusion in a Vascularising Scaffold. *Bulletin of Mathematical Biology* Epub ahead of print, 2007.
- ⁵¹LeBaron, R. G. and K. A. Athanasiou. *Ex vivo* synthesis of articular cartilage. *Biomaterials* 21: 2575-2587, 2000.
- ⁵²Lee, K. W., S. Wang, L. Lu, E. Jabbari, B. L. Currier and M. J. Yaszemski. Fabrication and characterization of poly(propylene fumarate) scaffolds with controlled pore structures using 3-dimensional printing and injection molding. *Tissue Eng.* 12(10): 2801-2811, 2006.
- ⁵³Lee, Y.-M., Y.-J. Seol, Y.-T. Lim, S. Kim, S.-B. Han, I.-C. Rhyu, S.-H. Baek, S.-J. Heo, J.-Y. Choi, P. R. Klokkevold and C.-P. Chung. Tissue-engineered growth of bone by marrow cell transplantation using porous calcium metaphosphate matrices. *J. Biomed. Mater. Res.* 54: 216-223, 2001.
- ⁵⁴Lemon, G. and J. R. King. Multiphase modelling of cell behaviour on artificial scaffolds: effects of nutrient depletion and spatially nonuniform porosity. *Mathematical Medicine and Biology* 24(1): 57-83, 2007.
- ⁵⁵Lewis, M. C., B. D. MacArthur, J. Malda, G. Pettet and C. P. Please. Heterogeneous proliferation within engineered cartilaginous tissue: the role of oxygen tension. *Biotechnol. Bioeng.* 91(5): 607-615, 2005.
- ⁵⁶Li, J., A. Beaussart, Y. Chen and A. F. Mak. Transfer of apatite coating from porogens to scaffolds: Uniform apatite coating within porous poly(DL-lactic-co-glycolic acid) scaffold in vitro. *Journal of Biomedical Materials Research Part A* 80(1): 226-233, 2007.
- ⁵⁷Li, J. P., J. R. de Wijn, C. A. van Blitterswijk and K. de Groot. Porous Ti6Al4V scaffold directly fabricating by rapid prototyping: preparation and in vitro experiment. *Biomaterials* 27(8): 1223-1235, 2006.

- ⁵⁸Li, S., J. R. D. Wijn, J. Li, P. Layrolle and K. D. Groot. Macroporous biphasic calcium phosphate scaffold with high permeability/porosity ratio. *Tissue Eng.* 9(3): 535-548, 2003.
- ⁵⁹Li, S. H., J. R. D. Wijn, P. Layrolle and K. d. Groot. Synthesis of macroporous hydroxyapatite scaffolds for bone tissue engineering. *J. Biomed. Mater. Res.* 61: 109-120, 2002.
- ⁶⁰Lievers, W. B., L. V., S. M. Arsenault, S. D. Waldman and A. K. Pilkey. Specimen size effect in the volumetric shrinkage of cancellous bone measured at two levels of dehydration. *Journal of Biomechanics* 40(9): 1903-1909, 2007.
- ⁶¹Lin, C. Y., N. Kikuchi and S. J. Hollister. A novel method for biomaterial scaffold internal architecture design to match bone elastic properties with desired porosity. *Journal of Biomechanics* 37(5): 623-636, 2004.
- ⁶²Liu, X., Y. Won and P. Ma. Porogen-induced surface modification of nano-fibrous poly(L-lactic acid) scaffolds for tissue engineering. *Biomaterials* 27(21): 3980-3987, 2006.
- ⁶³Liu, X. and P. X. Ma. Polymeric scaffolds for bone tissue engineering. *Annals of Biomedical Engineering* 32(3): 477-486, 2004.
- ⁶⁴Ma, P. X. and J.-W. Choi. Biodegradable polymer scaffolds with well-defined interconnected spherical pore network. *Tissue Eng.* 7(1): 23-33, 2001.
- ⁶⁵Malda, J., J. Rouwkema, D. E. Martens, E. P. I. Comte, F. K. Kooy, J. Tramper, C. A. v. Blitterswijk and J. Riesle. Oxygen gradients in tissue-engineered PEGT/PBT cartilaginous constructs: measurement and modeling. *Biotechnol. Bioeng.* 86(1): 9-18, 2004.
- ⁶⁶Mamchaoui, K. and G. Saumon. A method for measuring the oxygen consumption of intact cell monolayers. *American Journal of Physiology. Lung Cellular and Molecular Physiology* 278: 858-863, 2000.
- ⁶⁷Maquet, V., S. Blacher, R. Pirard, J.-P. Pirard, M. N. Vyakarnam and R. Jerome. Preparation of macroporous biodegradable poly(L-lactide-co-ε-caprolactone) foams and characterization by mercury intrusion porosimetry, image analysis, and impedance spectroscopy. *J. Biomed. Mater. Res.* 66A: 199-213, 2003.
- ⁶⁸Maspero, F. A., K. Ruffieux, B. Muller and E. Wintermantel. Resorbable defect analog PLGA scaffolds using CO₂ as solvent: Structural characterization. *J. Biomed. Mater. Res.* 62: 89-98, 2002.
- ⁶⁹Mooney, D. J., K. McNamara, D. Hern, J. P. Vacanti and R. Langer. Stabilized polyglycolic acid fibre-based tubes for tissue engineering. *Biomaterials* 17(2): 115-124, 1996.
- ⁷⁰Moore, M. J., E. Jabbari, E. L. Ritman, L. Lu, B. L. Currier, A. J. Windebank and M. J. Yaszemski. Quantitative analysis of interconnectivity of porous biodegradable scaffolds with micro-computed tomography. *Journal of Biomedical Materials Research Part A* 71(2): 258-267, 2004.
- ⁷¹Moroni, L., J. A. A. Hendriks, R. Schotel, J. R. D. Wijn and C. A. V. Blitterswijk. Design of biphasic polymeric 3-dimensional fiber deposited scaffolds for cartilage tissue engineering applications. *Tissue Eng.* 13(2), 2007.

- ⁷²Moroni, L., J. R. D. Wijn and C. A. V. Blitterswijk. 3D fiber-deposited scaffolds for tissue engineering: influence of pores geometry and architecture on dynamic mechanical properties. *Biomaterials* 27(7): 974-985, 2006.
- ⁷³Murphy, W. L., R. G. Dennis, J. L. Kileny and D. J. Mooney. Salt fusion: An approach to improve pore interconnectivity within tissue engineering scaffolds. *Tissue Eng.* 8(1): 43-52, 2002.
- ⁷⁴Nam, Y. S. and T. G. Park. Porous biodegradable polymeric scaffolds prepared by thermally induced phase separation. *J. Biomed. Mater. Res.* 47: 8-17, 1999.
- ⁷⁵Neves, A. A., N. Medcalf, M. Smith and K. M. Brindle. Evaluation of engineered meniscal cartilage constructs based on different scaffold geometries using magnetic resonance imaging and spectroscopy. *Tissue Eng.* 12(1): 53-62, 2006.
- ⁷⁶Oh, S. H., S. G. Kang, E. S. Kim, S. H. Cho and J. H. Lee. Fabrication and characterization of hydrophilic poly(lactic-co-glycolic acid)/poly(vinyl alcohol) blend cell scaffolds by melt-molding particulate-leaching method. *Biomaterials* 24: 4011-4021, 2003.
- ⁷⁷Oh, S. H., I. K. Park, J. M. Kim and J. H. Lee. *In vitro* and *in vivo* characteristics of PCL scaffolds with pore size gradient fabricated by a centrifugation method. *Biomaterials* 28(9): 1664-1671, 2007.
- ⁷⁸Oliveira, J. F. D., P. F. D. Aguiar, A. M. Rossi and G. A. Soares. Effect of process parameters on the characteristics of porous calcium phosphate ceramics for bone tissue scaffolds. *Artif. Organs* 27(5): 406-411, 2003.
- ⁷⁹Park, A., B. Wu and L. G. Griffith. Integration of surface modification and 3D fabrication techniques to prepare patterned poly(L-lactide) substrates allowing regionally selective cell adhesion. *J. Biomater. Sci. Polym. Ed.* 9(2): 89-110, 1998.
- ⁸⁰Peter, S. J., M. J. Miller, A. W. Yasko, M. J. Yaszemski and A. G. Mikos. Polymer concepts in tissue engineering. *J. Biomed. Mater. Res.* 43(4): 422-427, 1998.
- ⁸¹Petrov, N. and S. R. Pollack. Comparative analysis of diffusive and stress induced nutrient transport efficiency in the lacunar-canalicular system of osteons. *Biorheology* 40(1-3): 347-353, 2003.
- ⁸²Revsbech, N. P. An oxygen microsensor with a guard cathode. *Limnology and Oceanography* 34(2): 474-478, 1989.
- ⁸³Rodriguez-Lorenzo, L. M., M. Vallet-Regi and J. M. F. Ferreira. Fabrication of porous hydroxyapatite bodies by a new direct consolidation method: starch consolidation. *J. Biomed. Mater. Res.* 60: 232-240, 2002.
- ⁸⁴Rohner, D., D. W. Hutmacher, T. K. Cheng, M. Oberholzer and B. Hammer. *In vivo* efficacy of bone-marrow-coated polycaprolactone scaffolds for the reconstruction of orbital defects in the pig. *J. Biomed. Mater. Res.* 66B(2): 574-580, 2003.
- ⁸⁵Roy, T. D., J. L. Simon, J. L. Ricci, E. D. Rekow, V. P. Thompson and J. R. Parsons. Performance of degradable composite bone repair products made via three-dimensional fabrication techniques. *J. Biomed. Mater. Res.* 66A: 283-291, 2003.
- ⁸⁶Sachlos, E. and J. T. Czernuska. Making tissue engineering scaffolds work. Review: The application of solid freeform fabrication technology to the production of tissue engineering scaffolds. *Eur. Cell. Mater.* 5: 29-40, 2003.

- ⁸⁷Sanz-Herrera, J. A., J. M. Garcia-Aznar and M. Doblare. A mathematical model for bone tissue regeneration inside a specific type of scaffold. *Biomechanics and Modeling in Mechanobiology* Epub ahead of print, 2007.
- ⁸⁸Schantz, J.-T., A. Brandwood, D. W. Hutmacher, H. L. Khor and K. Bittner. Osteogenic differentiation of mesenchymal progenitor cells in computer designed fibrin-polymer-ceramic scaffolds manufactured by fused deposition modeling. *Journal of Materials Science: Materials in Medicine* 16(9): 807-819, 2005.
- ⁸⁹Scheidegger, A. E. *The Physics of Flow Through Porous Media*. New York: Macmillan, 1957, 236 pp.
- ⁹⁰Seitz, H., W. Rieder, S. Irsen, B. Leukers and C. Tille. Three-dimensional printing of porous ceramic scaffolds for bone tissue engineering. *Journal of Biomedical Materials Research. Part B, Applied Biomaterials* 74(2): 782-788, 2005.
- ⁹¹Shanbhag, S., J. W. Lee and N. Kotov. Diffusion in three-dimensionally ordered scaffolds with inverted colloidal crystal geometry. *Biomaterials* 26(27): 5581-5585, 2005.
- ⁹²Shanbhag, S., S. Wang and N. A. Kotov. Cell distribution profiles in three-dimensional scaffolds with inverted-colloidal-crystal geometry: modeling and experimental investigations. *Small* 1(12): 1208-1214, 2005.
- ⁹³Sheridan, M. H., L. D. Shea, M. C. Peters and D. J. Mooney. Bioabsorbable polymer scaffolds for tissue engineering capable of sustained growth factor delivery. *J. Control. Release* 64: 91-102, 2000.
- ⁹⁴Sherwood, J. K., S. L. Riley, R. Palazzolo, S. C. Brown, D. C. Monkhouse, M. Coates, L. G. Griffith, L. K. Landeen and A. Ratcliffe. A three-dimensional osteochondral composite scaffold for articular cartilage repair. *Biomaterials* 23: 4739-4751, 2002.
- ⁹⁵Singhal, A. R., C. M. Agrawal and K. A. Athanasiou. Salient degradation features of a 50:50 PLA/PGA scaffold for tissue engineering. *Tissue Eng.* 2(3): 197-207, 1996.
- ⁹⁶Sodian, R., M. Loebe, A. Hein, D. P. Martin, S. P. Hoerstrup, E. V. Potapov, H. Hausmann, T. Lueth and R. Hetzer. Application of stereolithography for scaffold fabrication for tissue engineered heart valves. *ASAIO J.* 48(1): 12-16, 2002.
- ⁹⁷Sodian, R., P. Fu, C. Lueders, D. Szymanski, C. Fritsche, M. Gutberlet, S. P. Hoerstrup, H. Hausmann, T. Lueth and R. Hetzer. Tissue engineering of vascular conduits: fabrication of custom-made scaffolds using rapid prototyping techniques. *The Thoracic and Cardiovascular Surgeon* 53(3): 144-149, 2005.
- ⁹⁸Sosnowski, S., P. Wozniak and M. Lewandowska-Szumiel. Polyester scaffolds with bimodal pore size distribution for tissue engineering. *Macromolecular Bioscience* 6(6): 425-434, 2006.
- ⁹⁹Spain, T. L., C. M. Agrawal and K. A. Athanasiou. New technique to extend the useful life of a biodegradable cartilage implant. *Tissue Eng.* 4(4): 343-352, 1998.
- ¹⁰⁰Suh, S. W., J. Y. Shin, J. Kim, J. Kim, C. H. Beak, D.-I. Kim, H. Kim, S. S. Jeon and I.-W. Choo. Effect of different particles on cell proliferation in polymer scaffolds using a solvent-casting and particulate leaching technique. *ASAIO J.* 48: 460-464, 2002.
- ¹⁰¹Taboas, J. M., R. D. Maddox, P. H. Krebsbach and S. J. Hollister. Indirect solid free form fabrication of local and global porous, biomimetic and composite 3D polymer-ceramic scaffolds. *Biomaterials* 24(1): 181-194, 2003.

- ¹⁰²Tan, K. H., C. K. Chua, K. F. Leong, C. M. Cheah, W. S. Gui, W. S. Tan and F. E. Wiria. Selective laser sintering of biocompatible polymers for applications in tissue engineering. *Bio-Medical Materials and Engineering* 15(1-2): 113-124, 2005.
- ¹⁰³Thomson, R. C., M. J. Yaszemski, J. M. Powers and A. G. Mikos. Hydroxyapatite fiber reinforced poly(α - hydroxy ester) foams for bone regeneration. *Biomaterials* 19: 1935-1943, 1998.
- ¹⁰⁴Tsang, V. L. and S. N. Bhatia. Fabrication of three-dimensional tissues. *Advances in Biochemical Engineering/Biotechnology* 103: 189-205, 2007.
- ¹⁰⁵Vacanti, J. P., M. A. Morse, W. M. Saltzman, A. J. Domb, A. Perez-Atayde, R. Langer, C. L. Mazzoni and C. Breuer. Selective cell transplantation using bioabsorbable artificial polymers as matrices. *J. Pediatr. Surg.* 23: 3-9, 1988.
- ¹⁰⁶Vozi, G., C. Fliam, A. Ahluwalia and S. Bhatia. Fabrication of PLGA scaffolds using soft lithography and microsyringe deposition. *Biomaterials* 24(14): 2533-2540, 2003.
- ¹⁰⁷Wang, F., L. Shor, A. Darling, S. Khalil, W. Sun, S. Gucer and A. Lau. Precision extruding deposition and characterization of cellular poly- ϵ -caprolactone tissue scaffolds. *Rapid Prototyping Journal* 10(1): 42-49, 2004.
- ¹⁰⁸Wang, H., J. Pieper, F. Peters, C. A. van Blitterswijk and E. N. Lammé. Synthetic scaffold morphology controls human dermal connective tissue formation. *Journal of Biomedical Materials Research Part A* 74(4): 523-532, 2005.
- ¹⁰⁹Whang, K., T. K. Goldstick and K. E. Healy. A biodegradable polymer scaffold for delivery of osteotropic factors. *Biomaterials* 21: 2545-2551, 2000.
- ¹¹⁰Widmer, M. S., P. K. Gupta, L. Lu, R. K. Meszlenyi, G. R. D. Evans, K. Brandt, T. Savel, A. Gurlek, C. W. P. Jr and A. G. Mikos. Manufacture of porous biodegradable polymer conduits by an extrusion process for guided tissue regeneration. *Biomaterials* 19: 1945-1955, 1998.
- ¹¹¹Williams, J. M., A. Adewunmi, R. M. Schek, C. L. Flanagan, P. H. Krebsbach, S. E. Feinberg, S. J. Hollister and S. Das. Bone tissue engineering using polycaprolactone scaffolds fabricated via selective laser sintering. *Biomaterials* 26(23): 4817-4827, 2005.
- ¹¹²Wiria, F. E., K. F. Leong, C. K. Chua and Y. Liu. Poly-epsilon-caprolactone/hydroxyapatite for tissue engineering scaffold fabrication via selective laser sintering. *Acta Biomaterialia* 3(1): 1-12, 2007.
- ¹¹³Woodfield, T. B., C. A. V. Blitterswijk, J. D. Wijn, T. J. Sims, A. P. Hollander and J. Riesle. Polymer scaffolds fabricated with pore-size gradients as a model for studying the zonal organization within tissue-engineered cartilage constructs. *Tissue Eng.* 11(9-10): 1297-1311, 2005.
- ¹¹⁴Wu, L. and J. Ding. Effects of porosity and pore size on in vitro degradation of three-dimensional porous poly(D,L-lactide-co-glycolide) scaffolds for tissue engineering. *Journal of Biomedical Materials Research Part A* 75(4): 767-777, 2005.
- ¹¹⁵Xie, J., M. Ihara, Y. Jung, I. K. Kwon, S. H. Kim, Y. H. Kim and T. Matsuda. Mechano-active scaffold design based on microporous poly(L-lactide-co-epsilon-caprolactone) for articular cartilage tissue engineering: dependence of porosity on compression force-applied mechanical behaviors. *Tissue Eng.* 12(3): 449-458, 2006.
- ¹¹⁶Yang, J., G. Shi, J. Bei, S. Wang, Y. Cao, Q. Shang, G. Yang and W. Wang. Fabrication and surface modification of macroporous poly(L-lactic acid) and poly(L-

- lactic-co-glycolic acid) (70/30) cell scaffolds for human skin fibroblast cell culture. *J. Biomed. Mater. Res.* 62: 438-446, 2002.
- ¹¹⁷Yang, S., K.-F. Leong, Z. Du and C.-K. Chua. The design of scaffolds for use in tissue engineering. Part II. Rapid prototyping techniques. *Tissue Eng.* 8(1): 1-11, 2002.
- ¹¹⁸Yang, S., K.-F. Leong, Z. Du and C.-K. Chua. The design of scaffolds for use in tissue engineering. Part I. Traditional factors. *Tissue Eng.* 7(6): 679-689, 2001.
- ¹¹⁹Yeong, W. Y., C. K. Chua, K. F. Leong and M. Chandrasekaran. Rapid prototyping in tissue engineering: challenges and potential. *Trends Biotechnol.* 22(12): 643-652, 2004.
- ¹²⁰Yurt, N., H. Beyenal, J. Sears and Z. Lewandowski. Quantifying selected growth parameters of *Leptothrix discophora* SP-6 in biofilms from oxygen concentration profiles. *Chemical Engineering Science* 58(20): 4557-4566, 2003.
- ¹²¹Zein, I., D. W. Hutmacher, K. C. Tan and S. H. Teoh. Fused deposition modeling of novel scaffold architectures for tissue engineering applications. *Biomaterials* 23: 1169-1185, 2002.
- ¹²²Zhao, F., Y. Yin, W. W. Lu, J. C. Leong, W. Zhang, J. Zhang, M. Zhang and K. Yao. Preparation and histological evaluation of biomimetic three-dimensional hydroxyapatite/chitosan-gelatin network composite scaffolds. *Biomaterials* 23: 3227-3234, 2002.

Vita

Tejas Shyam Karande was born on June 23, 1977 in Bombay (Mumbai), India, the son of Dr. Shyam Janardan Karande and Dr. (Mrs.) Alka Shyam Karande. He passed the Indian Certificate of Secondary Education (ICSE) examination from Greenlawns High School, Mumbai, India in 1993 following which he joined Jai Hind College, Mumbai, India in the science stream to pass the Higher Secondary Certificate (HSC) exam in 1995. He obtained the Bachelor of Engineering degree in Biomedical Engineering from the Dwarkadas J. Sanghvi College of Engineering, University of Mumbai, Mumbai, India in 1999 and the Master of Science degree in Biomedical Engineering from the University of Texas at Austin, Austin, Texas in 2002. The citation for the paper he has published is: Karande, T. S., Ong, J. L., Agrawal, C. M.: Diffusion in musculoskeletal tissue engineering scaffolds: Design issues related to porosity, permeability, architecture, and nutrient mixing. *Annals of Biomedical Engineering*, 32(12), 1728-1743, 2004.

Permanent address: C-9/10, Ganesh Prasad, Sreater Road, Mumbai-400 007, India.

This dissertation was typed by Tejas Shyam Karande.